

ABSTRACT

Title of dissertation: Excited Nucleon and Delta Spectra
From Lattice QCD

Eric Engelson, Doctor of Philosophy, 2009

Dissertation directed by: Professor Stephen J. Wallace
Department of Physics

We calculate the nucleon and delta excited state spectra from lattice QCD. Operators which transform as irreducible representations of the lattice symmetry group are used as bases for variational calculations. We compute matrices of correlation functions between all the operators in the variational bases. From the time dependence of the eigenvalues of these matrices, we extract energy eigenvalues. By subducing the continuum $SU(3)$ rotation group to the octahedral group, we can identify the spins of the continuum states which correspond to the lattice states.

In the nucleon spectrum calculation, we use $24^3 \times 64$ anisotropic lattices with pion masses of 416 MeV and 576 MeV. The lattices have a spacing of about 0.1 fm and an anisotropy of 3. We use the Wilson gauge and the Wilson fermion actions with two flavors of dynamical light quarks. The low-lying spectrum has many of the qualitative features of the physical spectrum and we are able to identify the continuum states which correspond to several of the lattice states. This includes one of the first observations of a spin- $\frac{5}{2}$ state on the lattice.

For the delta spectrum calculation, we use $16^3 \times 128$ anisotropic lattices. The

gauge action is the tree-level tadpole improved Wilson gauge action, while in the fermion sector we use the clover action. The pion mass is about 390 MeV and the anisotropy is 3.5. We have two flavors of dynamical light quarks as well as dynamical strange quarks. To compute the correlation functions, we use the distillation method in which operators are projected on the the low lying eigenmodes of the Laplacian operator, allowing for an exact computation of all-to-all propagators between the distilled source and sink operators. We are able to identify four low-lying states with continuum delta states.

Excited Nucleon and Delta Spectra From Lattice QCD

by

Eric Engelson

Dissertation submitted to the Faculty of the Graduate School of the
University of Maryland, College Park in partial fulfillment
of the requirements for the degree of
Doctor of Philosophy
2009

Advisory Committee:

Professor Stephen J. Wallace/Advisor

Professor Paulo Bedaque

Professor Elizabeth J. Beise

Professor Thomas Cohen

Professor Michael Coplan

© Copyright by
Eric Engelson
2009

Acknowledgements

I would never have been able to complete this project without the help and support of many people. First and foremost, I would like to thank my advisor. The guidance and instruction I have received from over the past several years have been immeasurable. He has always been willing to take the time to answer my questions and provide me with any necessary instruction. My development as a scientist would not have been possible without his encouragement and support.

This work could not have been completed without the combined efforts of my collaborators: John Bulava, Dr. Saul Cohen, Dr. Jozef Dudek, Dr. Robert Edwards, Dr. Justin Foley, Dr. Bálint Joó, Dr. K. Jimmy Juge, Dr. Adam Lichtl, Dr. Huey-Wen Lin, Dr. Nilmani Mathur, Dr. Colin Morningstar, Dr. Michael J. Peardon, Dr. David G. Richards, and Dr. Sinéad Ryan. In particular, David Richards and Robert Edwards have provided invaluable assistance including timely responses to countless emails as well as their hospitality during several trips to Jefferson Laboratory. I would also like to thank Jo Dudek for his assistance with the correlator reconstruction method used in this work. The code which performed this calculation was developed by him.

A special thanks goes to Loretta Robinette. Our research group would likely cease to function without her work.

Last but certainly not least, I would like to thank my family. Without their love and support I never would have made it this far.

Table of Contents

List of Tables	v
List of Figures	vii
1 Introduction	1
1.1 The Standard Model	2
1.2 The Strong Nuclear Force	5
1.2.1 Quark Models	7
1.3 Quantum Chromodynamics	11
1.3.1 Asymptotic Freedom	13
1.4 Baryon Spectroscopy	13
2 Lattice Quantum Chromodynamics	22
2.1 Path Integral Formalism	22
2.2 Discretizing Space-time	24
2.3 Euclidean Field Theory	25
2.4 Lattice Gauge Actions	27
2.5 Lattice Fermion Actions	29
2.6 Extracting Excited State Energies	31
2.6.1 The Variational Method	33
2.7 The Monte Carlo Method	39
2.8 Calculation Overview	43
2.8.1 Error Analysis	45
3 Optimized Baryon Operators	48
3.1 The Building Blocks	49
3.1.1 Quark Smearing	50
3.1.2 Gauge Link Smearing	51
3.1.3 Displacements	52
3.2 Momentum Projections	55
3.3 Flavor Projections	55
3.4 Spin and Parity Projections	59
3.4.1 The Octahedral Group	59
3.4.2 Projecting onto Group Irreps	61
3.4.3 Continuum Spin Identification	71
4 The Excited Nucleon Spectrum	73
4.1 Nucleon Correlation Functions	73
4.1.1 Minimizing Matrix Inversions	76
4.1.2 Charge Conjugation	78
4.2 Anisotropic Lattices	81
4.2.1 Tuning the Action	83
4.3 Setting the Scale	84

4.4	Gauge Configurations	85
4.4.1	Smearing Parameters	88
4.5	Operator Pruning	92
4.6	Backward State Contamination	95
4.7	Operator Rephasing	96
4.8	The Variational Method	99
4.8.1	Filtering	105
4.8.2	Choosing t_0 and t^*	106
4.9	Fitting Method	113
4.10	Results	115
4.10.1	Multi-particle Thresholds	115
4.10.2	Discussion	130
5	Distillation	134
5.1	All-to-all Propagators	135
5.1.1	Stochastic All-to-All Propagators	137
5.2	Distillation: Exact All-to-All Propagators	138
5.3	Distillation Tests	142
6	The Excited Delta Spectrum	147
6.1	Improved Actions	147
6.2	Lattice Parameters	150
6.3	Operator Pruning	152
6.4	Results	153
6.4.1	Discussion	154
7	Conclusions and Outlook	164
A	Nucleon Operators	167
B	Delta Operators	171
	Bibliography	178

List of Tables

1.1	The fundamental particles in nature.	3
1.2	The fundamental forces in nature.	4
1.3	Quantum numbers of the three flavors of quarks in Gell-Mann and Zweig's constituent quark model.	8
3.1	Patterns of displacements for baryon operators.	56
3.2	Quark model flavor wave functions for zero strangeness light baryons.	57
3.3	Quark model flavor wave functions for strange light baryons.	58
3.4	Projections of elemental annihilation operators onto operators of definite isospin and strangeness.	59
3.5	Restrictions on spin and displacement indices for nucleon operators for each displacement pattern.	63
3.6	Restrictions on spin and displacement indices for delta operators for each displacement pattern.	64
3.7	The number of embeddings of irreps of O^D for nucleon operators of each displacement type.	69
3.8	The number of embeddings of irreps of O^D for delta operators of each displacement type.	70
3.9	The number of occurrences of each irrep of O^D in the subduction of $SO(3)$	72
4.1	Canonical orientations for each displacement pattern in baryon operators.	78
4.2	Parameters used in the generation of gauge configurations for $N_f = 2$ Wilson gauge and Wilson fermion lattices used in the nucleon spectrum calculation.	89
4.3	The nucleon spectrum at $m_\pi = 416$ MeV.	116
4.4	The nucleon spectrum at $m_\pi = 578$ MeV.	117
6.1	The delta spectrum at $m_\pi = 390$ MeV.	155

A.1	Final set of operators used in nucleon spectrum calculation in the G_1 channels.	168
A.2	Final set of operators used in nucleon spectrum calculation in the H channels.	169
A.3	Final set of operators used in nucleon spectrum calculation in the G_2 channels.	170
B.1	Final set of operators used in the delta spectrum calculation in the G_{1g} channel.	172
B.2	Final set of operators used in the delta spectrum calculation in the G_{1u} channel.	173
B.3	Final set of operators used in the delta spectrum calculation in the H_g channel.	174
B.4	Final set of operators used in the delta spectrum calculation in the H_u channel.	175
B.5	Final set of operators used in the delta spectrum calculation in the G_{2g} channel.	176
B.6	Final set of operators used in the delta spectrum calculation in the G_{2u} channel.	177

List of Figures

1.1	The pseudoscalar meson octet.	9
1.2	The baryon decuplet and octet.	9
1.3	Nucleon and delta energy levels from experiment and a quark model calculation.	15
1.4	Nucleon spectrum from quenched QCD with $m_\pi = 490$ MeV.	16
1.5	Nucleon spectrum from quenched QCD with $m_\pi = 700$ MeV.	17
1.6	Delta spectrum from quenched QCD with $m_\pi = 700$ MeV.	18
1.7	Experimental nucleon spectrum organized by lattice irreps.	19
1.8	Experimental delta spectrum organized by lattice irreps.	20
3.1	A comparison of the effective energies of three different nucleon operators with and without smearing.	53
4.1	Effective energies of correlation functions used to calculate the pion mass for the lattices with $m_\ell = -0.4125$	87
4.2	Energies of pion and ρ states with different momenta and corresponding fits to the energy-momentum dispersion relation.	88
4.3	Effective energy at $t =$ for various nucleon operators as a function σ_s and n_σ	90
4.4	Jackknife error in the effective energy at $t = 4$ for various nucleon operators as a function of ρ and n_ρ	91
4.5	Effective energy of the nucleon G_{1g} ground and three excited states for different choices of the Gaussian quark smearing radius.	93
4.6	Nucleon G_{1g} ground state correlator at $m_\pi = 416$ MeV obtained using the variational method.	97
4.7	Nucleon G_{1u} ground state correlator at $m_\pi = 416$ MeV obtained using the variational method.	98
4.8	Phases of the matrix elements of the G_{1g} nucleon correlator matrix at $t = 1$ for the 136 upper triangle elements.	100

4.9	Time dependence of the phase of an imaginary correlator matrix element.	101
4.10	χ^2 of the reconstructed correlator matrix for charmonium, diagonalized using the principle correlator method, as a function of t_0	109
4.11	χ^2 for the reconstructed nucleon correlator matrices, diagonalized using the fixed eigenvector method, at the optimal t_0 and varying t^*	110
4.12	A diagonal G_{1g} nucleon correlator matrix element and its reconstruction, using the optimal choice for t_0 and t^*	111
4.13	A diagonal nucleon G_{1g} correlator matrix element and its reconstruction, choosing t_0 smaller than the optimal value.	112
4.14	Plots of $C_{II}^\Lambda(t)e^{E_I^\Lambda(t-t_0)}$ for the four extracted nucleon G_{1g} states at $m_\pi = 578$ MeV.	118
4.15	Plots of $C_{II}^\Lambda(t)e^{E_I^\Lambda(t-t_0)}$ for the four extracted nucleon G_{1u} states at $m_\pi = 578$ MeV.	119
4.16	Plots of $C_{II}^\Lambda(t)e^{E_I^\Lambda(t-t_0)}$ for the four extracted nucleon H_g states at $m_\pi = 578$ MeV.	120
4.17	Plots of $C_{II}^\Lambda(t)e^{E_I^\Lambda(t-t_0)}$ for the four extracted nucleon H_u states at $m_\pi = 578$ MeV.	121
4.18	Plots of $C_{II}^\Lambda(t)e^{E_I^\Lambda(t-t_0)}$ for the four extracted nucleon G_{2g} states at $m_\pi = 578$ MeV.	122
4.19	Plots of $C_{II}^\Lambda(t)e^{E_I^\Lambda(t-t_0)}$ for the four extracted nucleon G_{2u} states at $m_\pi = 578$ MeV.	123
4.20	Plots of $C_{II}^\Lambda(t)e^{E_I^\Lambda(t-t_0)}$ for the four extracted nucleon G_{1g} states at $m_\pi = 416$ MeV.	124
4.21	Plots of $C_{II}^\Lambda(t)e^{E_I^\Lambda(t-t_0)}$ for the four extracted nucleon G_{1u} states at $m_\pi = 416$ MeV.	125
4.22	Plots of $C_{II}^\Lambda(t)e^{E_I^\Lambda(t-t_0)}$ for the four extracted nucleon H_g states at $m_\pi = 416$ MeV.	126
4.23	Plots of $C_{II}^\Lambda(t)e^{E_I^\Lambda(t-t_0)}$ for the four extracted nucleon H_u states at $m_\pi = 416$ MeV.	127
4.24	Plots of $C_{II}^\Lambda(t)e^{E_I^\Lambda(t-t_0)}$ for the four extracted nucleon G_{2g} states at $m_\pi = 416$ MeV.	128

4.25	Plots of $C_{II}^\Lambda(t)e^{E_I^\Lambda(t-t_0)}$ for the four extracted nucleon G_{2u} states at $m_\pi = 416$ MeV.	129
4.26	The nucleon spectrum at $m_\pi = 578$ MeV.	131
4.27	The nucleon spectrum at $m_\pi = 416$ MeV.	132
5.1	Feynman diagrams for connected and disconnected contributions to flavorless meson propagators.	137
5.2	The number of eigenvalues of the Laplacian operator less than λ_{max} for $16^3 \times 128$ and $20^3 \times 128$ lattices.	143
5.3	Effective mass plots for two single-site and two singly displaced G_{1g} nucleon operators on $16^3 \times 128$ lattices calculated with different number of eigenvectors.	144
5.4	Fitted energies of the ground and first excited states from a G_{1g} nucleon variational calculation.	145
5.5	Effective mass plots for two single-site and two singly displaced G_{1g} nucleon operators on $16^3 \times 128$ and $20^3 \times 128$ lattices calculated with different numbers of eigenvectors.	146
6.1	Location of various $N_f = 2 + 1$ ensembles in the $l_\Omega - s_\Omega$ plane.	151
6.2	The effective energy for three single-site and three doubly-displaced-I delta operators, which all appear to couple to the same state.	153
6.3	Plots of $C_{II}^\Lambda(t)e^{E_I^\Lambda(t-t_0)}$ for the four extracted delta G_{1g} states at $m_\pi = 390$ MeV.	156
6.4	Plots of $C_{II}^\Lambda(t)e^{E_I^\Lambda(t-t_0)}$ for the four extracted delta G_{1u} states at $m_\pi = 390$ MeV.	157
6.5	Plots of $C_{II}^\Lambda(t)e^{E_I^\Lambda(t-t_0)}$ for the four extracted delta H_g states at $m_\pi = 390$ MeV.	158
6.6	Plots of $C_{II}^\Lambda(t)e^{E_I^\Lambda(t-t_0)}$ for the four extracted delta H_u states at $m_\pi = 390$ MeV.	159
6.7	Plots of $C_{II}^\Lambda(t)e^{E_I^\Lambda(t-t_0)}$ for the four extracted delta G_{2g} states at $m_\pi = 390$ MeV.	160
6.8	Plots of $C_{II}^\Lambda(t)e^{E_I^\Lambda(t-t_0)}$ for the four extracted delta G_{2u} states at $m_\pi = 390$ MeV.	161

6.9	The delta spectrum at $m_\pi = 390$ MeV.	162
-----	--	-----

Chapter 1

Introduction

The goal of particle physics is to discover the basic constituents of nature and determine the ways in which they interact. Moreover, physicists would like to understand how macroscopic phenomena arise from the interactions between fundamental particles. As experimental physics has progressed, scientists have been able to probe smaller and smaller length scales and repeatedly have discovered substructure in what were thought to be indivisible particles.

Atomic theories have their roots in ancient Greek philosophy, but the first scientific treatment developed in the 17th and 18th centuries as chemists observed certain substances which could not be broken down by chemical means. It was hypothesized that these substances were made up of indivisible atoms. Around the turn of the twentieth century, Einstein's theory of Brownian motion would provide the first conclusive evidence that matter did, indeed, consist of microscopic particles.

In the mid 1800's Mendeleev published his periodic table of the elements, which organized the elements based on patterns in their properties. These patterns suggested that the atomic properties of the elements arose due to different arrangements of constituent particles. The first subatomic particle to be discovered was the electron, which Thomson isolated in 1897. Rutherford's gold foil experiment a decade later revealed that the atom consisted of a heavy, positively-charged nu-

cleus surrounded by a cloud of light, negatively-charged electrons. The proton was discovered by Rutherford in 1918, and the neutron by Chadwick in the 1930's.

Since then, particle physicists have found that the proton and neutron consist of smaller particles known as quarks, and a myriad of other particles have been discovered. The culmination of the last century of particle physics is the standard model.

1.1 The Standard Model

A complete treatment of particle physics and the standard model can be found a number of textbooks [1, 2, 3] and a catalog of all results from theoretical and experimental particle physics can be found in [4]. According to the standard model, matter consists of twelve fundamental particles (as well as their antiparticles): six flavors of quarks (up, down, strange, charm, bottom and top) and six leptons (the electron, muon, tau, and the three neutrinos). The up, charm, and top quark all have a charge of $+\frac{2}{3}$, while the down, strange, and bottom quarks all have a charge of $-\frac{1}{3}$.¹ The quarks also possess a color charge, which binds them together to form particles such as the proton and neutron. The electron, muon, and tau have an electric charge of -1, while the three neutrinos are uncharged. The particles can be arranged in three generations, each consisting of a positively charged quark, a negatively charged quark, a charged lepton, and its corresponding neutrino. The charged particles in the second generation are about two orders of magnitude more

¹In units where the magnitude of the charge of the electron is 1.

Table 1.1: The fundamental particles in nature. Energies of the charged particles are given in MeV in parentheses [4].

	Quarks		Leptons	
1 st Generation	u(1.5-3.0)	d(3-7)	e(0.511)	ν_e
2 nd Generation	c(1250)	s(95)	$\mu(105.7)$	ν_μ
3 rd Generation	t(174200)	b(4200)	$\tau(1777)$	ν_τ
Electric Charge	$+\frac{2}{3}$	$-\frac{1}{3}$	-1	0

massive than the corresponding particles in the first generation. A similar relation is observed between the second and third generations. The fundamental particles are summarized in Table 1.1.

There exist four fundamental interactions between the particles: strong, electromagnetic, weak, and gravity. The strong force acts on the color charge of the quarks to produce colorless bound states known as hadrons. At short distances hadrons may interact strongly in a manner similar to van der Waals forces between electrically neutral molecules. This is the mechanism that binds protons and neutrons together to form nuclei. At large separations (compared to the size of nucleus, $\sim 10^{-15}$ m) hadrons do not interact and the strong force is, therefore, considered a short range force. Within that range its strength is typically much greater than that of the other forces.

The electromagnetic force binds electrons and nuclei together into atoms, and in turn, the atoms into molecules and all the large extended objects seen in the

Table 1.2: The fundamental forces in nature, adapted from [1].

	strong	electromagnetic	weak	gravity
gauge boson	gluon	photon	W^\pm, Z	-
range	$\sim 10^{-15}$ m	∞	$\sim 10^{-17}$ m	∞
relative strength	1	10^{-2}	10^{-6}	10^{-39}

universe. The quantum field theory of electrodynamics, QED, is today considered the most well-tested theory in science. The weak force is responsible for nuclear phenomena including beta decay. All of the particles in Table 1.1 participate in the weak force. It allows the transformation of one flavor of quark to another. The electromagnetic and weak forces were unified by the work of Glashow, Weinberg, and Salam [5, 6, 7]. The electroweak force is mediated through gauge bosons: the photon for the electromagnetic force, and the W and Z bosons for the weak force. The photon is massless, allowing the electromagnetic force to have an infinite range, while the massive weak gauge bosons allow the weak force to act only across finite distances $\sim \frac{1}{M_W}$. The mass of the weak bosons is due to the Higgs mechanism. Although the Higgs boson is yet to be observed, most particle physicists believe its existence will be experimentally confirmed at the LHC in the near future. The remaining force, gravity, is very weak in comparison to the other three forces. Its effects are negligible at the subatomic level. The fundamental forces in nature are summarized in Table 1.2, adapted from [1].

The standard model unites the electroweak and strong forces into a single

framework. It is known to be incomplete, as it does not include a description of gravity. Nevertheless, it has been very successful at explaining a wide range of phenomena in subatomic physics up to an energy scale of about 1 TeV.

1.2 The Strong Nuclear Force

In this work, we calculate the energies of strongly bound multi-quark states from quantum chromodynamics (QCD), the quantum field theory which describes the strong force within the standard model. We first review the development of strong physics and QCD. A complete treatment can be found in [8].

With the discovery that the nucleus consists of protons and neutrons, it was clear that there had to exist a new force to bind the constituents together. This new interaction had to overcome the electromagnetic repulsion of the protons and attract the neutrons. As this interaction was not observed outside of the nucleus, it was inferred that it was only felt by particles separated by about 10^{-15} m, the length scale of the nucleus. Yukawa introduced the first quantum field theory for the strong force in 1934. In his theory, the force was mediated by a massive particle which he called the pion. The strong force potential between two nucleons was given by

$$V(r) = \frac{g^2}{4\pi r} e^{-m_\pi r}, \quad (1.1)$$

where g is the coupling constant and m_π the mass of the pion. Yukawa predicted this mass to be ~ 200 MeV in order to obtain the desired range of ~ 1 fm. The pion would be discovered in 1947 [9].

However, it soon became clear that the pion was not the fundamental transmitter of the strong force and was, in fact, a composite particle. Throughout the following decade, a large number of additional new particles and resonances were also discovered. Several states, such as the Δ 's, Σ 's, Ξ 's, Ω^- , and Λ^0 were all heavier than the nucleon and decayed into nucleon states. These particles are collectively known as “baryons”. Likewise, a family of states including the kaons and η , which decayed into pion states, were classified as “mesons”. The electron and the muon (and later the tau and the neutrinos) were classified as “leptons”. To explain why certain interactions were never observed, physicists assigned the particles new quantum numbers such as baryon and lepton number. Requiring these quantities to be conserved explained why certain reactions did not occur.

Some of the newly discovered particles, such as the kaons, were observed to be produced on very short time scales relative to their decay time. A new quantum number called strangeness was introduced to explain this phenomenon [10, 11, 12]. The pions and nucleons have zero strangeness, while the kaons have strangeness one. The strange particles are produced in pairs with opposite strangeness (and thus zero net strangeness) but then decay through a much slower process to zero strangeness states. In the language of the standard model, they are produced via the strangeness conserving strong force, but decay through the strangeness violating weak force.

One peculiar aspect of the mass spectrum is the existence of several sets of particles with identical quantum numbers (ignoring electric charge) and nearly degenerate masses. As an example, the masses of the proton and neutron are, $m_p = 938.27$

and $m_n = 939.57$. This led Heisenberg to postulate that the proton and neutron were different states of the same particle known as the nucleon [13]. This symmetry would be broken by electromagnetic interactions, resulting in the small difference in mass between the two particles, similar to Zeeman splitting of electron spin states in the hydrogen atom. In the absence of electromagnetic forces, the two particles would be indistinguishable, and their behavior under the nuclear force would be identical. The neutron and proton form the basis of a two-dimensional Hilbert space. The nucleon is two-component vector within this space and the nuclear force is invariant under $SU(2)$ transformations.² Mathematically, these transformations are identical to the transformations of spin- $\frac{1}{2}$ states in a rotationally invariant system, and thus we call this symmetry “isospin.” Other hadrons, such as the pions and deltas form higher dimensional isospin multiplets which are analogous to states of higher angular momentum.

1.2.1 Quark Models

The quark model [14] arose from an attempt to organize the new particles in a manner similar to Mendeleev’s construction of the periodic table of elements. Gell-Mann and Ne’eman [15, 16] placed the particles in hexagonal and trigonal tables based on their charge and strangeness. The pseudoscalar meson octet is shown in Fig. 1.1 while the baryon decuplet and octet are shown in Fig. 1.2. Just as the patterns of elements in the periodic table correspond to different arrange-

²The electromagnetic splitting would actually make the proton heavier than the neutron. The mass splitting is really due to $SU(2)$ being only an approximate symmetry.

Table 1.3: Quantum numbers of the three flavors of quarks in Gell-Mann and Zweig's constituent quark model.

Flavor	Spin	Baryon Number	Charge	Strangeness
up	$\frac{1}{2}$	$\frac{1}{3}$	$+\frac{2}{3}$	0
down	$\frac{1}{2}$	$\frac{1}{3}$	$-\frac{1}{3}$	0
strange	$\frac{1}{2}$	$\frac{1}{3}$	$-\frac{1}{3}$	1

ments of protons, neutrons, and electrons within the atoms, Gell-Mann and Zweig hypothesized the existence of constituent particles which Gell-Mann called quarks [17, 18, 19]. At the time, only three flavors of quarks were needed to explain all known particles. The quantum numbers of the quarks are summarized in Table 1.3. The mesons consist of a quark-antiquark state while the baryons are a three quark state. Hadrons with zero strangeness are combinations of the up and down quarks. These two quarks form an $SU(2)$ isospin doublet. The flavor wave functions of mesons then transform as a $\mathbf{2} \otimes \bar{\mathbf{2}} = \mathbf{3} \oplus \mathbf{1}$ multiplet. The three $\mathbf{3}$ corresponds to the pions, while the $\mathbf{1}$ is a singlet state. The baryon flavor wave functions transform as a $\mathbf{2} \otimes \mathbf{2} \otimes \mathbf{2} = \mathbf{4} \oplus \mathbf{2} \oplus \mathbf{2}$ multiplet. The $\mathbf{4}$ are the Δ 's and the mixed-antisymmetric $\mathbf{2}$ are the nucleons. These states all have definite isospin I and I_3 quantum numbers. We can expand the quark multiplet to $SU(3)$ by including the strange quark. For mesons, we have $\mathbf{3} \otimes \bar{\mathbf{3}} = \mathbf{8} \oplus \mathbf{1}$, forming an octet corresponding to the meson octet and a singlet, the η' . In the baryon sector, we have $\mathbf{3} \otimes \mathbf{3} \otimes \mathbf{3} = \mathbf{10} \oplus \mathbf{8} \oplus \mathbf{8} \oplus \mathbf{1}$. Here we have a completely symmetric decuplet and a mixed-antisymmetric octet,

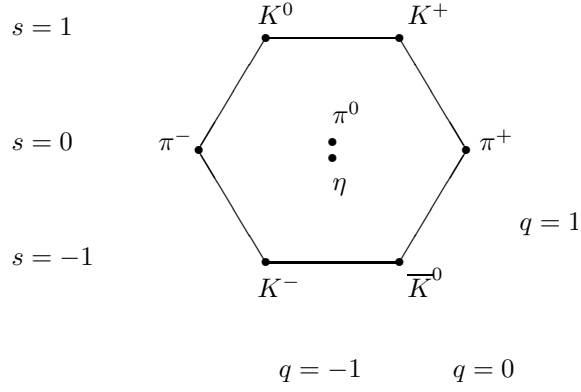


Figure 1.1: The pseudoscalar meson octet.

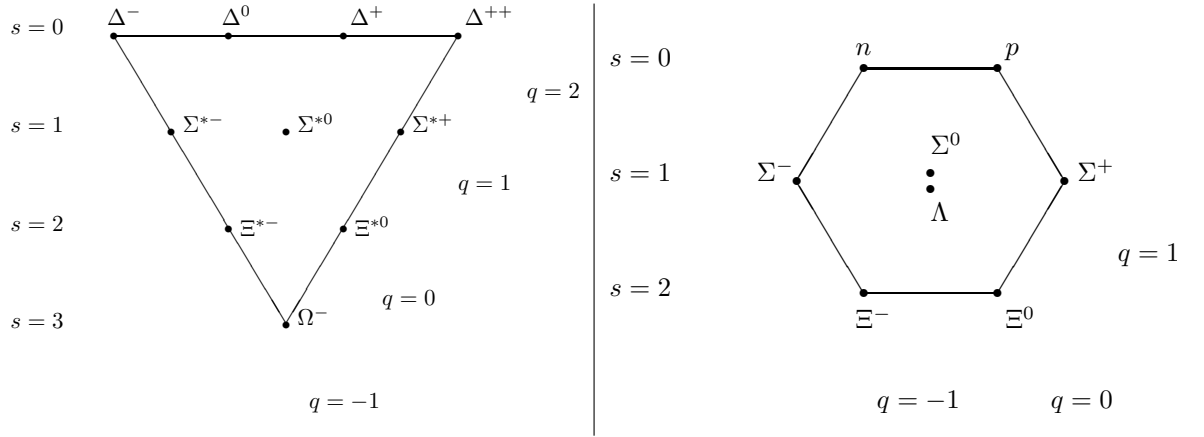


Figure 1.2: The baryon decuplet (left) and octet (right).

corresponding to the particles in Fig. 1.2.

Some of the quark model states had a wave function completely symmetric under particle exchange, a violation of the Pauli-exclusion principle. Greenberg [20] proposed a new quantum number now known as color [21] which could take on three values: red, green, and blue. It was postulated that hadrons are “colorless” combinations of quarks: baryons consisted of a red, a green, and a blue quark, while mesons were a color-anticolor combination. Since the three quarks within a baryon all have a different color, the color wave function can then be antisymmetrized. The

requirement that all states be colorless implied that the quarks were confined and that isolated quarks could never be observed.

Although the quark model was successful in explaining the properties of many particles, most physicists regarded quarks as nothing more than a theoretical construct. The first evidence for their existence came in the late 1960's from the deep inelastic scattering experiments at SLAC [22]. These results were explained by Feynman's parton model which described the proton as a collection of point-like particles [23]. At high energies, these particles were found to be non-interacting, a phenomenon known as asymptotic freedom.

In 1974, a new heavy meson called the J/Ψ was discovered with a lifetime about 1000 times higher than would be expected for a particle that heavy. The quark model, expanded to include a fourth quark known as "charm," offered the best explanation for the new meson. The expanded model predicted the existence of many new charmed particles which would eventually be discovered. Other experiments compared the cross section of e^+e^- scattering into both hadrons and to $\mu^+\mu^-$. The cross sections for both reactions could be computed using quantum electrodynamics. The results of the experiments suggested that the quarks came in three varieties, providing evidence for the existence of color.

Gell-Mann and Fritzsche would identify the color of the quarks as the charge associated with the strong force [24, 25]. The work of Gross, Wilcek, and Politzer showed that an $SU(3)$ gauge field, which would couple to the colored quarks, was asymptotically free at high energies and confining at low energies [26, 27]. From these ideas, a quantum field theory describing the strong force, QCD, emerged.

1.3 Quantum Chromodynamics

The QCD picture of the hadron is very different from that in the quark model. A baryon does, in fact, contain three quarks and a meson a quark-antiquark pair, which we call “valence quarks,” but their interaction is mediated by the exchange of massless gluons. These gluons, in turn, can couple to quark-antiquark loops as well as gluon loops. The interaction is non-perturbative at the hadronic energy scale. In fact, the up and down quarks have a mass on the order of a few MeV, while the proton and neutron have mass of nearly 1000 MeV. The majority of the energy in the hadrons is due to the gluons and the virtual “sea” quarks and their non-perturbative interactions.

QCD is a quantum field theory [28] that describes the strong interaction between the quarks. Each quark field has three color components, each of which is a spinor field. The gluons are represented by a gauge field which acts on the SU(3) color symmetry. As SU(3) has eight generators, we require eight gluon fields to maintain local gauge invariance. We denote a quark field of flavor F as $\psi^F(x)$ and a gluon field as A_μ^a with $a = 1 \dots 8$.

The QCD Lagrangian is

$$\mathcal{L}_{QCD}(x) = \mathcal{L}_G(x) + \mathcal{L}_Q(x), \tag{1.2}$$

where $\mathcal{L}_G(x)$ is purely gluonic and $\mathcal{L}_Q(x)$ describes the dynamics of the quarks. The

gluonic part is³

$$\mathcal{L}_G(x) = -\frac{1}{4}\text{Tr} [F^{\mu\nu}(x)F_{\mu\nu}(x)], \quad (1.3)$$

$$F_{\mu\nu}(x) = \partial_\mu A_\nu(x) - \partial_\nu A_\mu(x) + ig [A_\mu(x), A_\nu(x)], \quad (1.4)$$

$$A_\mu(x) = \sum_{a=1}^8 A_\mu^a(x) \frac{\lambda^a}{2}, \quad (1.5)$$

where g is the strength of coupling of the gauge field, and the λ^a are the Gell-Mann matrices which generate the SU(3) group. Expanding the commutators yields three- and four-gluon interactions.

In the fermion sector, the Lagrangian is

$$\mathcal{L}_Q(x) = \sum_F \bar{\psi}^F(x)(i\gamma^\mu D_\mu - M_F)\psi^F(x), \quad (1.6)$$

with $\bar{\psi}^F(x) = \psi^{\dagger F}\gamma_0$, M_F is the mass of a quark of flavor F , and D_μ is the covariant derivative,

$$D_\mu = \partial_\mu + igA_\mu. \quad (1.7)$$

Under a local gauge transformation, denoted by $V(x) = e^{i\alpha^a(x)\lambda^a/2}$, with the $\alpha^a(x)$ arbitrary differentiable functions, we have the following transformation properties:

$$\psi^F(x) \rightarrow V(x)\psi^F(x), \quad (1.8)$$

$$A_\mu(x) \rightarrow V(x) \left(A_\mu(x) + \frac{i}{g}\partial_\mu \right) V^\dagger(x), \quad (1.9)$$

$$F_{\mu\nu} \rightarrow V(x)F_{\mu\nu}(x)V^\dagger(x). \quad (1.10)$$

We also define the parallel transporters along a path \mathcal{C}

$$U(\mathcal{C}) = \mathcal{P}e^{ig\int_{\mathcal{C}} A_\mu(x)dx}, \quad (1.11)$$

³Unless otherwise noted, summation over repeated indices is implied.

where \mathcal{P} indicates a path ordered integral. We can write our covariant derivative in terms of the parallel transporter:

$$D_\mu = \lim_{\epsilon \rightarrow 0} \frac{1}{\epsilon} [\psi(x + \epsilon \hat{\mu}) - U(x + \epsilon \hat{\mu}, x) \psi(x)], \quad (1.12)$$

where $U(x + \epsilon \hat{\mu}, x)$ is the parallel transporter along an infinitesimal path from x to $x + \epsilon \hat{\mu}$.

1.3.1 Asymptotic Freedom

One of the unique features of QCD is asymptotic freedom. The renormalized coupling constant in QCD, $\alpha_s = g^2/4\pi$, “runs” and changes with the energy scale of the interaction. To leading order, the coupling constant is

$$\alpha_s(k^2) \approx \frac{\alpha_s(\Lambda_{QCD})}{1 + \alpha_s(\Lambda_{QCD}) \frac{32-2n_f}{12\pi} \ln \left(\frac{k^2}{\Lambda_{QCD}^2} \right)}, \quad (1.13)$$

where Λ_{QCD} is on the order of 300 MeV. As the energy scale of the interaction k^2 increases to infinity, α_s goes to zero and we can use perturbation theory to calculate in QCD. At the hadronic scale, however, $\alpha_s \sim 1$, and perturbation theory breaks down.

1.4 Baryon Spectroscopy

Because perturbation theory is impossible at the hadronic scale, quark models have remained an important tool for studying strongly bound states. Modern quark models introduce a typically spin-independent confining potential as well as a variety of spin-dependent interactions. Using this potential, the spectrum of bound states

and decay rates can be calculated. However, quark models remain unsatisfactory for a number of reasons. As shown in Fig. 1.3 from [4], in the nucleon and delta spectrum the quark model predicts many more states than are observed experimentally. This may be the result of the quark model having too many degrees of freedom. A possible reduction in the number of degrees of freedom can be effected by modeling a baryon as a diquark-quark state. On the other hand, it may be that these “missing states” can only be observed experimentally in unstudied channels. A direct QCD calculation could resolve this issue.

In any case, the quark model is not derived from QCD and thus does not provide any insight into how the bound states arise from the fundamental interactions of the quarks. It also does not contain a mechanism for calculating excitations of the gluon fields and determining the energies of glueballs, hybrids, and other exotic states.

The only way to perform first principles calculations in QCD at the hadronic scale is to numerically integrate the path integral representations of physical observables. This requires QCD to be reformulated on a finite and discrete space-time lattice. This procedure will be described in detail in the next chapter. Lattice QCD allows for the calculation of a wide range of QCD observables and is a key component in the nuclear physics research program. In this work, we calculate the energy spectrum of baryons on the lattice. In particular, we study the spectrum for light baryons with $I = \frac{1}{2}$ (the nucleons) and $I = \frac{3}{2}$ (the deltas).

The Hadron Spectrum (HadSpec) Collaboration has developed the technology to extract the masses of excited states in lattice QCD, including the development

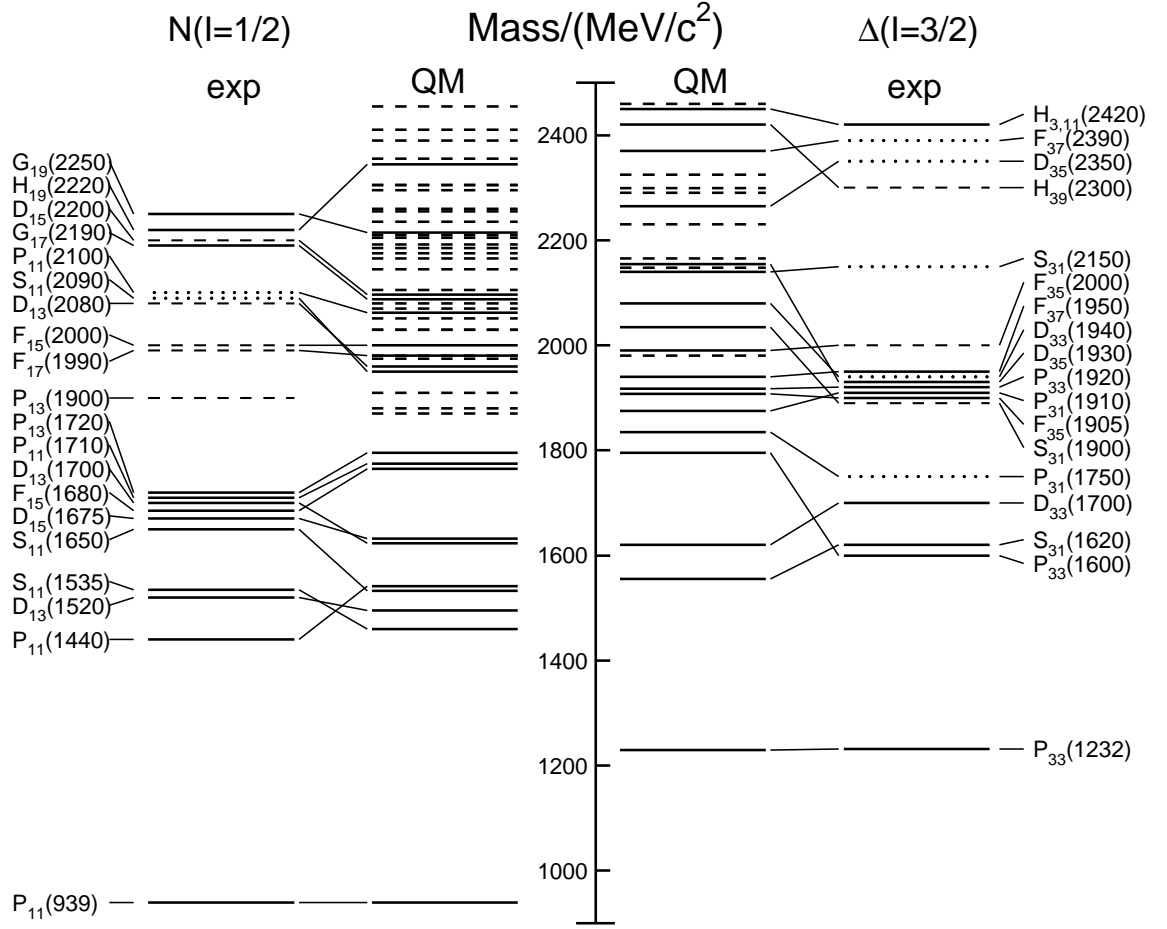


Figure 1.3: From [4], nucleon and delta energy levels from experiment (exp) and a quark model (QM) calculation. Three and four star states are indicated with a solid line, two star states with a dashed line, and one star states with a dotted lines. For the quark model, those states with a tentative correspondence with an experimentally observed state are indicated with a solid line, while those states without an observed counterpart are indicated by a dashed line.

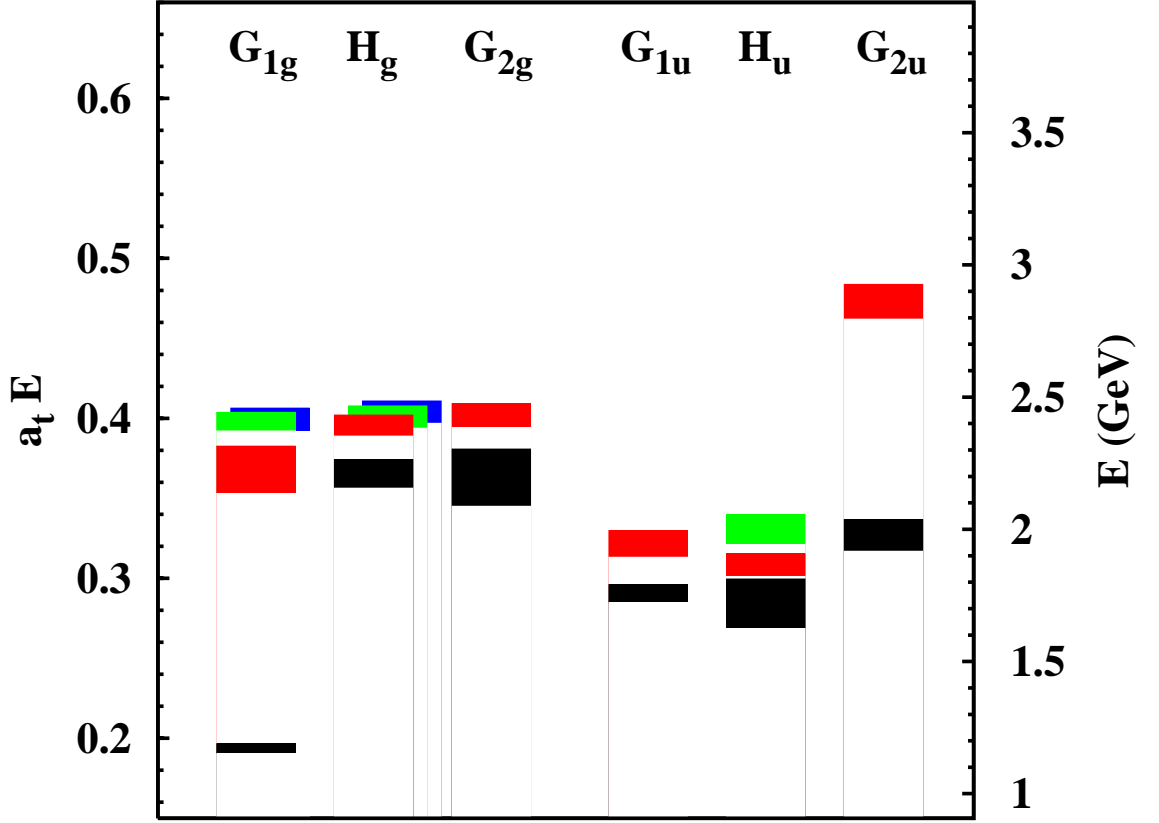


Figure 1.4: From [29], the nucleon spectrum from $167 \, 24^3 \times 64$ quenched lattices with $m_\pi = 490$ MeV. States are separated into irreducible representations of the lattice rotation group, as discussed in Chapter 3. The heights of the boxes represent the statistical uncertainty.

of sets of operators which transform as rows of the irreducible representations of the lattice rotation group. These operators have been used to perform spectroscopy calculations in quenched QCD as shown in Figs. 1.4, 1.5, and 1.6 [29, 30, 31]. In Figs. 1.7 and 1.8 we show the experimental nucleon and delta energy spectra organized by lattice irreducible representations.

In this work we take an important step forward and present some of the first

Nucleon Mass Spectrum

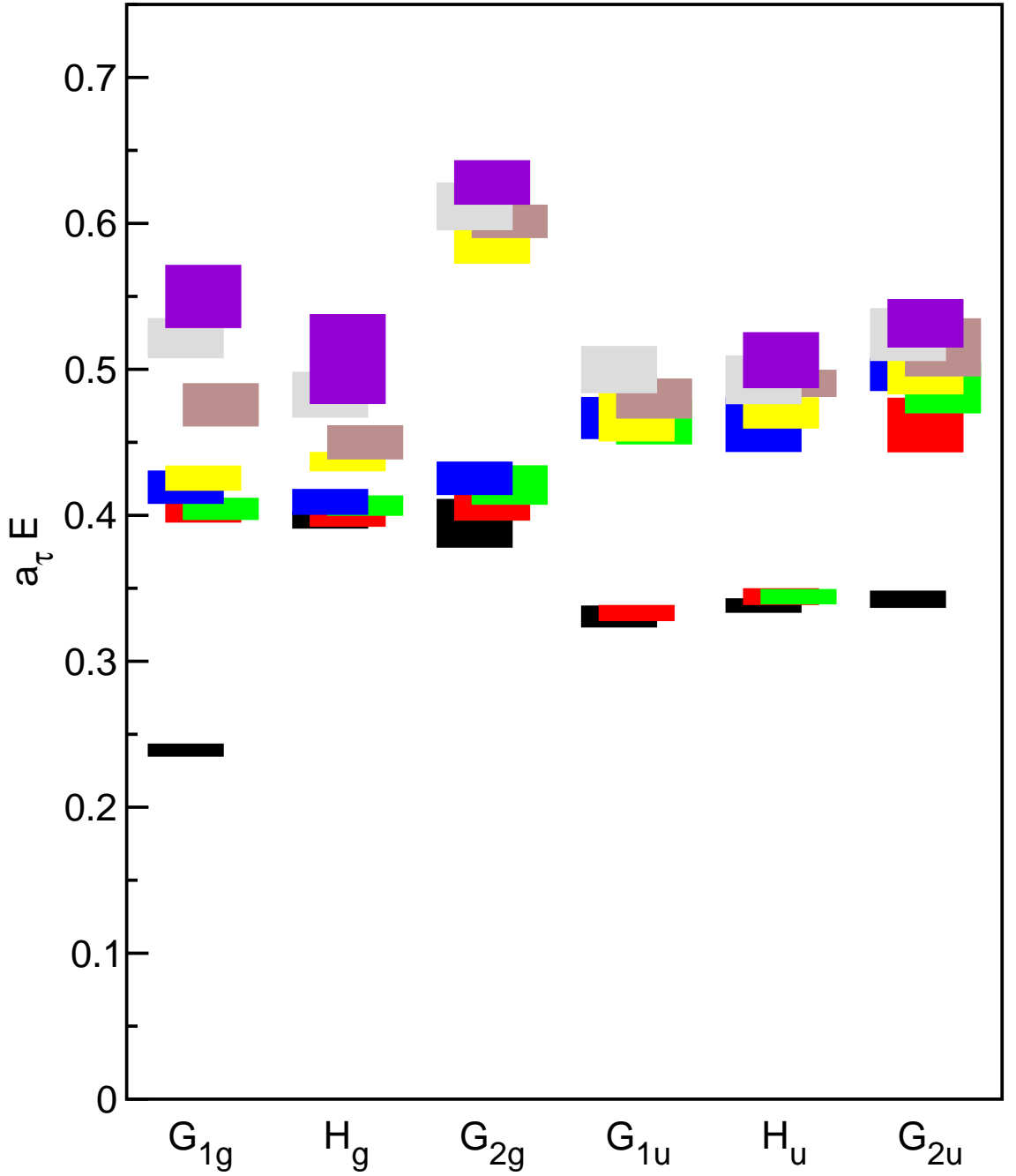


Figure 1.5: From [30], the nucleon spectrum from 200 $12^3 \times 48$ quenched lattices with $m_\pi = 700$ MeV. States are separated into irreducible representations of the lattice rotation group, as discussed in Chapter 3. The heights of the boxes represent the statistical uncertainty.

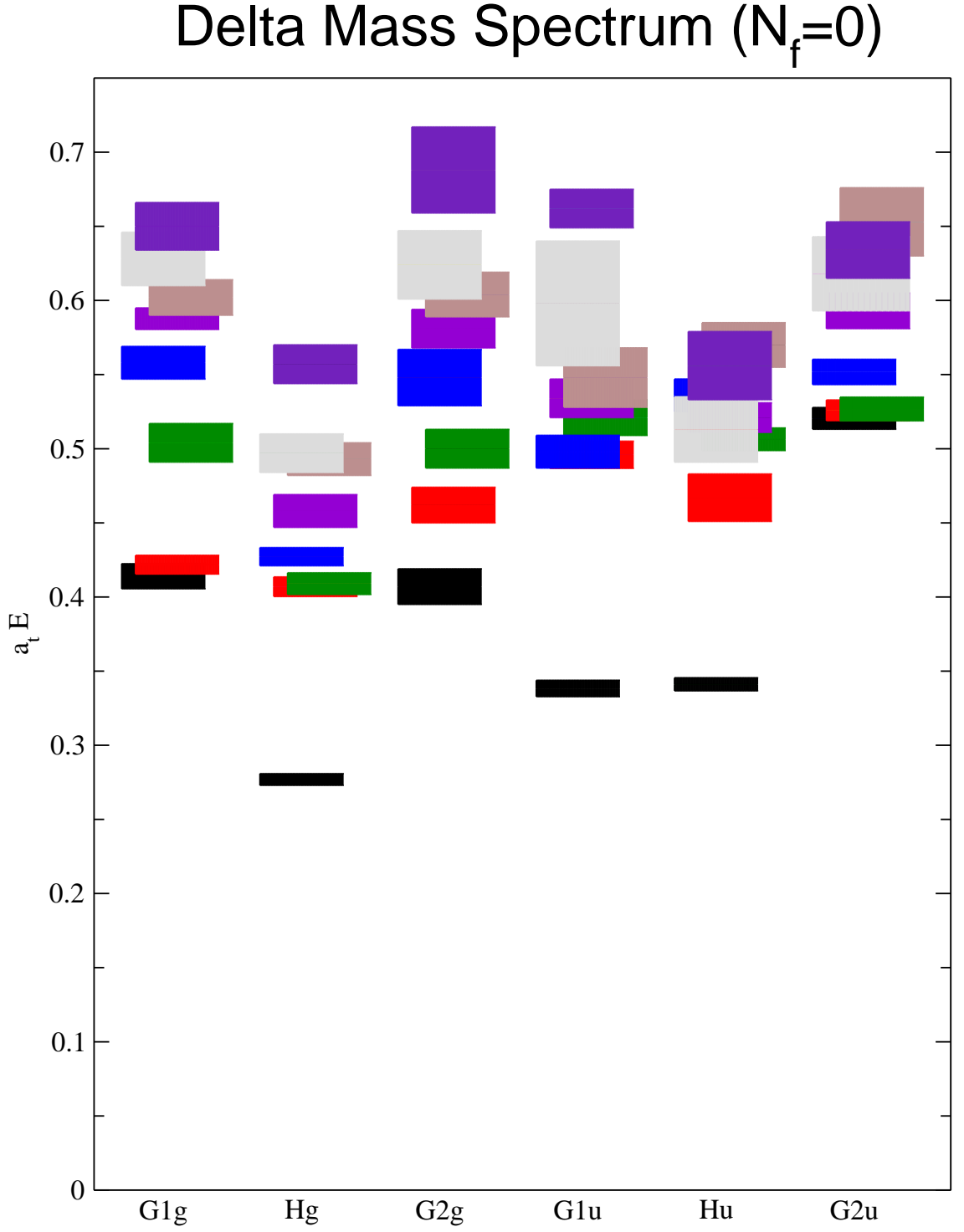


Figure 1.6: From [31], the delta spectrum from 200 $12^3 \times 48$ quenched lattices with $m_\pi = 700$ MeV. States are separated into irreducible representations of the lattice rotation group, as discussed in Chapter 3. The heights of the boxes represent the statistical uncertainty.

Nucleon Mass Spectrum (Exp)

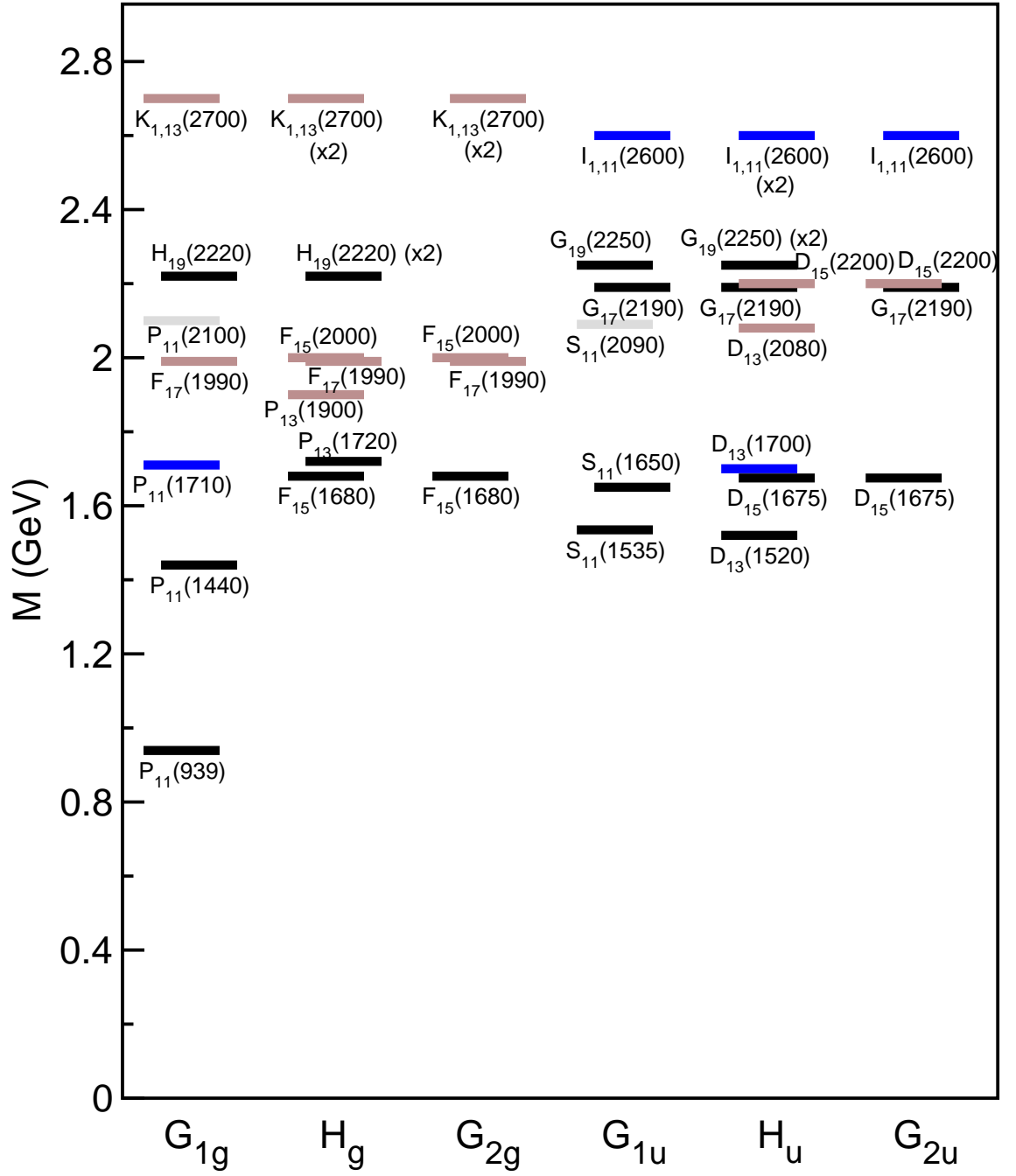


Figure 1.7: Experimental nucleon spectrum organized by lattice irreps. Four-star states are indicated by black lines, three-star states by blue lines, two-star states by tan lines, and one-star states by gray lines. Notation is $L_{I,2J}$, where L is the orbital angular momentum, I is the isospin, and J is the total angular momentum.

Delta Mass Spectrum (Exp)

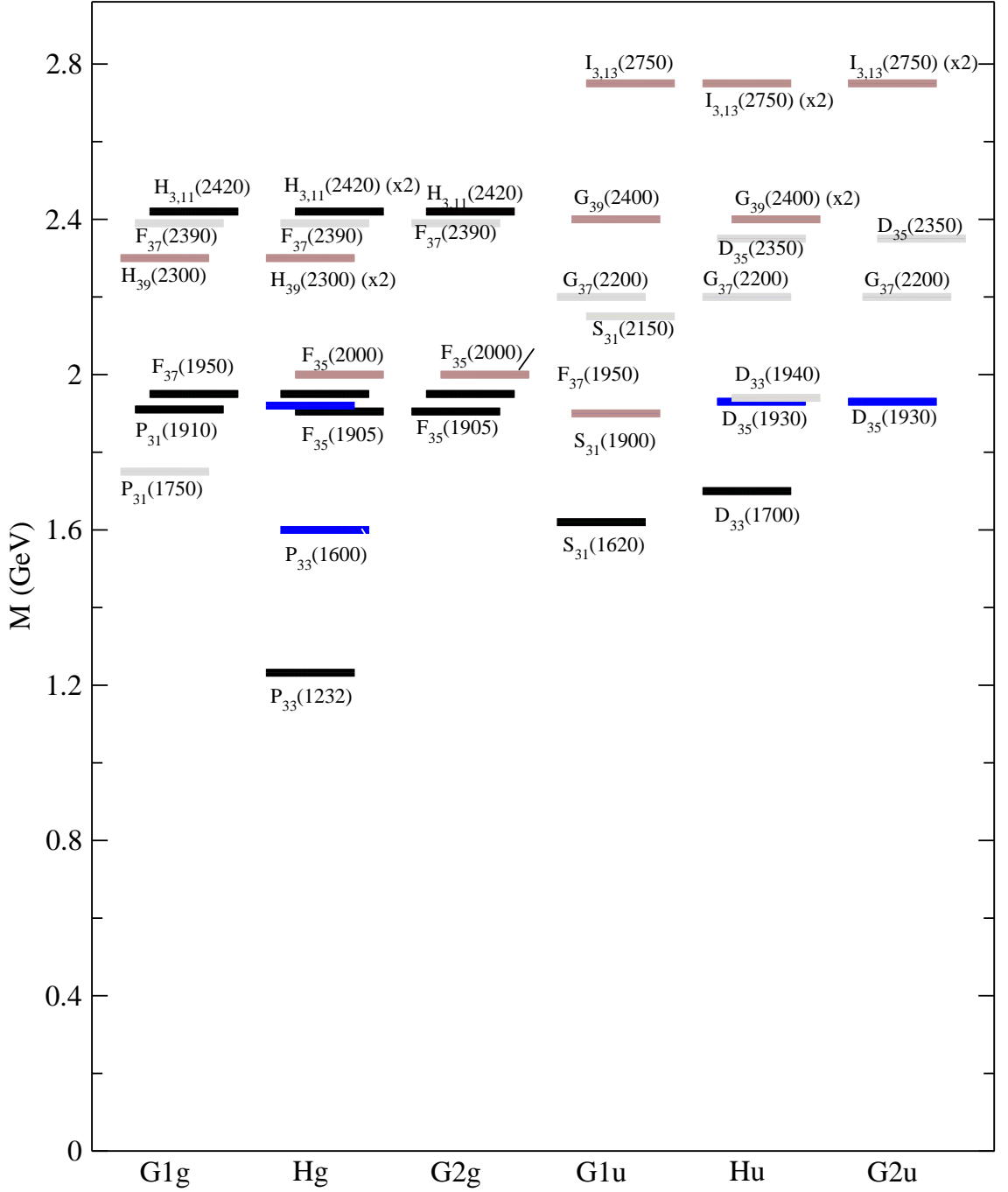


Figure 1.8: Experimental delta spectrum organized by lattice irreps. Four-star states are indicated by black lines, three-star states by blue lines, two-star states by tan lines, and one-star states by gray lines. Notation is $L_{2I,2J}$, where L is the orbital angular momentum, I is the isospin, and J is the total angular momentum.

excited nucleon and delta spectroscopy results with fully dynamical light quarks. In Chapter 2 we present an overview of lattice QCD including the discretization of the QCD action and the Monte Carlo method for performing lattice calculations on a computer. In particular, we focus on the methods for extracting the excited energy spectrum. An important step in this calculation is the development of operators which have good coupling to the states of interest. These operators should have definite quantum numbers and transform as irreducible representations of the lattice symmetry group. These symmetries as well as the construction of the operators is discussed in Chapter 3. In Chapter 4, we present results of a nucleon excited energy spectrum calculation with two flavors of dynamical light fermions. We introduce a new calculational method in Chapter 5 known as distillation which, in the future, will facilitate the calculation of matrix elements of multi-hadron operators. As we approach the physical pion mass, the inclusion of such operators will be important for the identification of multi-hadron states in the calculated spectrum. In Chapter 6, we use this technique to calculate the delta spectrum using dynamical light and strange quarks. Finally, in Chapter 7 we offer some concluding remarks and the outlook for the future.

Chapter 2

Lattice Quantum Chromodynamics

The goal of lattice QCD [32, 33, 34, 35] is to reformulate QCD on a finite, discrete space-time lattice so that QCD path integrals can be calculated on a computer. In this chapter, we first review Feynman's path integral formalism in Section 2.1. We describe the discretization of space-time in Section 2.2, followed by the transformation of QCD to the Euclidean manifold in Section 2.3, and the formulation of the lattice action in Sections 2.4 and 2.5. In Section 2.6, we describe specifically how we perform mass spectrum calculations. In Section 2.7, we describe the Monte Carlo integration method for evaluating QCD integrals on a computer. Finally, in Section 2.8, we give an overview of a lattice spectrum calculation.

2.1 Path Integral Formalism

The path integral formulation of quantum mechanics, developed by Feynman [36, 37], rewrites a matrix element between an initial and final state of a quantum system as an integral over intermediate states. The integral is essentially a sum over every possible path through coordinate space from initial to final state, modulated by a phase e^{iS} , where S is the action for that path. For a field theory, we integrate over field configurations, where a configuration is the specification of the value of the field at all points in space-time. All the physical information of the field theory

is contained in the vacuum expectation values of time-ordered products of field operators. For a scalar bosonic theory, with field operators denoted by $\phi(x)$, the path integral representation is

$$\langle \phi_f | \mathcal{T} [\phi(x_1)\phi(x_2)\dots\phi(x_n)] | \phi_i \rangle = \frac{1}{Z} \int D[\phi] \phi(x_1)\phi(x_2)\dots\phi(x_n) e^{iS[\phi]}, \quad (2.1)$$

$$Z = \int D[\phi] e^{iS[\phi]}, \quad (2.2)$$

where ϕ_i and ϕ_f are the initial and final field configurations at times t_i and t_f respectively. The integral is over all possible field configurations subject to the boundary conditions $\phi(t_i) = \phi_i$ and $\phi(t_f) = \phi_f$.

For fermions, the path integral must capture the anticommutation property of the field operators. This is accomplished by integrating over anticommuting Grassmann numbers. The elements of a Grassmann algebra $\{\eta_1, \dots, \eta_N\}$ have the following properties:

$$\{\eta_i, \eta_j\} = 0, \quad (2.3)$$

$$\eta_i^2 = 0. \quad (2.4)$$

The integration of Grassmann numbers is defined to be

$$\int d\eta_i = 0, \quad (2.5)$$

$$\int d\eta_i \eta_i = 1. \quad (2.6)$$

The quark propagator in QCD is given by

$$\langle \Omega | \mathcal{T} [\psi(x)\bar{\psi}(y)] | \Omega \rangle = \frac{1}{Z} \int D[\bar{\psi}]D[\psi]D[U] \psi(x)\bar{\psi}(y) e^{iS[\bar{\psi},\psi,U]}, \quad (2.7)$$

$$Z = \int D[\bar{\psi}]D[\psi]D[U] e^{iS[\bar{\psi},\psi,U]}, \quad (2.8)$$

where the integral over the fermion fields is performed using the rules of Grassmann integration.

As written, this is an ill-formed integral because there are an uncountably infinite number of integration variables (the value of the fields at every space-time point). We approximate the integral by reformulating the theory on a finite space-time lattice with appropriate boundary conditions. This technique, developed by Wilson [38], is called lattice QCD.

2.2 Discretizing Space-time

We reformulate QCD on a finite four-dimensional manifold, with periodic or anti-periodic boundary conditions. We denote the lattice spacing by a and the length of the lattice by L .¹ The fields are defined only at points $x_\mu = n_\mu a$, where each component of n_μ is an integer. In the discretized theory, integrals over space-time are replaced by sums over all lattice points:

$$\int d^4x f(x) \rightarrow \sum_{n_\mu} a^4 f(n_\mu a), \quad (2.9)$$

with $0 \leq n_\mu < L$. It is conventional to work with dimensionless fields, absorbing the factors of a on the right hand side of Eq. (2.9) into the field and quark mass as

¹For now we will assume an isotropic lattice with lattice spacings and total lengths the same in all directions. Later we will allow the time direction to have a finer spacing and more lattice sites than the spatial directions.

follows:

$$\psi(x) \rightarrow a^{3/2}\psi(x), \quad (2.10)$$

$$M \rightarrow aM. \quad (2.11)$$

With these definitions, the lattice spacing a does not explicitly appear in the action.

Derivatives of a function with respect to space are replaced by differences in the value of the function at nearby lattice points. There are a number of definitions which converge to a derivative in the continuum. The most common are the forward ∇_μ^f , backward ∇_μ^b , and symmetric ∇_μ^s derivatives defined as follows:

$$\nabla_\mu^f \psi(x) = \frac{1}{a} [\psi(x + a\hat{\mu}) - \psi(x)], \quad (2.12)$$

$$\nabla_\mu^b \psi(x) = \frac{1}{a} [\psi(x) - \psi(x - a\hat{\mu})], \quad (2.13)$$

$$\nabla_\mu^s \psi(x) = \frac{1}{2} [\Delta_\mu^f \psi(x) + \Delta_\mu^b \psi(x)] = \frac{1}{2a} [\psi(x + a\hat{\mu}) - \psi(x - a\hat{\mu})]. \quad (2.14)$$

In the continuum limit, the forward and backward derivatives converge to a derivative with $\mathcal{O}(a^2)$ corrections, while the symmetric derivative converges with $\mathcal{O}(a^3)$ corrections. We define the discretized second derivative as follows

$$\Delta_\mu \psi(x) = \frac{1}{a} [\nabla_\mu^f \psi(x) - \nabla_\mu^b \psi(x)] = \frac{1}{a^2} [\psi(x + \hat{\mu}a) + \psi(x - \hat{\mu}a) - 2\psi(x)]. \quad (2.15)$$

In the continuum, this converges to ∂_μ^2 with $\mathcal{O}(a^4)$ corrections.

2.3 Euclidean Field Theory

Lattice field theory is typically formulated in Euclidean space, rather than Minkowski space, by analytically continuing the theory to imaginary times. Integration in the time direction is performed along the imaginary axis, which effectively

converts the metric from Minkowski to Euclidean. As a result, the discrete space-time lattice becomes a four-dimensional hypercube and the phase factor in Eq. (2.7) changes from e^{iS} to e^{-S} . This change is essential for performing a Monte Carlo integration of the path integral. From this point on, all quantities are assumed to be on the Euclidean manifold, unless labeled with a subscript or superscript M .

By convention, the Euclidean time axis is labeled 4 and there is no distinction between upper and lower indices. The coordinates and derivatives in Euclidean space are connected to those in Minkowski space by

$$x^4 = x_4 = ix_M^0 = ix_0^M, x^j = x_j = x_M^j = -x_j^M, \quad (2.16)$$

$$\partial^4 = \partial_4 = -i\partial_M^0 = -i\partial_0^M, \partial^j = \partial_j = -\partial_M^j = \partial_j^M. \quad (2.17)$$

We define the vector potential $A_\mu(x)$ as follows:

$$A^4 = A_4 = -iA_M^0 = -iA_0^M, A^j = A_j = -A_M^j = A_j^M. \quad (2.18)$$

Finally, we must redefine the Dirac γ matrices to satisfy $\{\gamma_\mu, \gamma_\nu\} = 2\delta_{\mu\nu}$. This is accomplished with

$$\gamma^4 = \gamma_4 = \gamma_M^0 = \gamma_0^M, \gamma^j = \gamma_j = -i\gamma_M^j = i\gamma_j^M, \gamma_5 = \gamma_4\gamma_1\gamma_2\gamma_3 = \gamma_5^M. \quad (2.19)$$

We now compute the Minkowski QCD action in terms of the Euclidean action.

From Eq. (2.18) the Euclidean field strength tensor is

$$F^{4i} = F_{4i} = iF_M^{0i} = -iF_{0i}^M, F^{ij} = F_{ij} = F_M^{ij} = F_{ij}^M. \quad (2.20)$$

This gives for the action in the gauge sector

$$iS_G^M = i \int dx_M^0 \int d^3 \mathbf{x}_M \left(-\frac{1}{4} F_{\mu\nu}^M F_{\mu\nu}^M \right), \quad (2.21)$$

$$= i \int (-idx_4) \int d^3 \mathbf{x} \left(-\frac{1}{4} \right) [(iF_{4i})(-iF_{4i}) + (-iF_{4i})(iF_{4i}) + F_{ij}F_{ij}], \quad (2.22)$$

$$= - \int d^4 x \frac{1}{4} F_{\mu\nu} F_{\mu\nu} \equiv -S_G. \quad (2.23)$$

To derive the Euclidean fermion action we first note that from Eqs. (2.17) and (2.18), the covariant derivative in Euclidean space is

$$D^4 = D_4 = -iD_0^M = -iD_M^0, D^j = D_j = -D_M^j = D_j^M. \quad (2.24)$$

Thus, the Euclidean fermion action is

$$iS_F^M = i \int dx_M^0 \int d^3 \mathbf{x}_M \bar{\psi}_M (i\gamma_M^0 D_0^M + i\gamma_M^j D_j^M - M) \psi_M, \quad (2.25)$$

$$= i \int (-idx_4) \int d^3 \mathbf{x} \bar{\psi} (i\gamma_4(iD_4) + i(i\gamma_j)D_j - M) \psi, \quad (2.26)$$

$$= - \int d^4 x \bar{\psi} (\gamma_\mu D_\mu + M) \psi \equiv -S_F, \quad (2.27)$$

and the QCD Lagrangian in Euclidean space is

$$S = \frac{1}{4} F_{\mu\nu} F_{\mu\nu} + \bar{\psi} (\gamma_\mu D_\mu + m) \psi. \quad (2.28)$$

2.4 Lattice Gauge Actions

We now turn our attention to discretizing the Euclidean QCD action. The discretized gauge action is parameterized in terms of the parallel transporters, Eq. (1.11), along the lines connecting adjacent lattice points. We denote the “gauge link” from point x to $x + a\hat{\mu}$ as $U_\mu(x)$. In terms of the gluon fields we have

$$U_\mu(x) = e^{iagA_\mu(x)}. \quad (2.29)$$

From Eq. (1.5), the gauge links are SU(3) matrices. They transform under a gauge transformation as

$$U_\mu(x) \rightarrow V(x)U_\mu(x)V^\dagger(x + a\hat{\mu}). \quad (2.30)$$

This enables us to maintain an exact local gauge symmetry. In contrast, the transformation of $A_\mu(x)$ involves a derivative, which would have to be approximated on the lattice. As a result, if we parameterize the gauge field in terms of $A_\mu(x)$, rather than $U_\mu(x)$, we can only maintain an approximate local gauge symmetry. The gauge links have the property

$$U_\mu(x) = U_{-\mu}^\dagger(x + a\hat{\mu}). \quad (2.31)$$

We write the discretized action in terms of gauge invariant quantities. The simplest such quantity is the plaquette, the parallel transporter from a point x , around an elementary loop in the $\mu\nu$ plane back to x , which we denote $U_{\mu\nu}(x)$:

$$U_{\mu\nu}(x) = U_\mu(x)U_\nu(x + a\hat{\mu})U_\mu^\dagger(x + a\hat{\nu})U_\nu^\dagger(x), \quad (2.32)$$

$$= e^{igaA_\mu(x)}e^{igaA_\nu(x+a\hat{\mu})}e^{-igaA_\mu(x+a\hat{\nu})}e^{-igaA_\nu(x)}, \quad (2.33)$$

$$= \exp \left(ia^2g \left(\frac{A_\nu(x + a\hat{\mu}) - A_\nu(x)}{a} + \frac{A_\mu(x + a\hat{\nu}) - A_\mu(x)}{a} + \frac{1}{2}g[A_\mu(x), A_\nu(x)] \right. \right. \\ \left. \left. + \frac{1}{2}g[A_\mu(x + a\hat{\nu}), A_\nu(x + a\hat{\mu})] \right) + \mathcal{O}(a^3) \right), \quad (2.34)$$

where in the last line we have used the Baker-Campbell-Hausdorff formula. In the continuum limit, the first two terms of the exponential converge to partial derivatives of the field, and we combine the commutators by evaluating the fields at x . This

gives

$$U_{\mu\nu} \underset{a \rightarrow 0}{=} \exp \left(i g a^2 (\partial_\mu A_\nu(x) - \partial_\nu A_\mu(x) + g[A_\mu(x), A_\nu(x)]) + \mathcal{O}(a^3) \right) \quad (2.35)$$

$$= e^{i g a^2 F_{\mu\nu} + \mathcal{O}(a^3)} \quad (2.36)$$

Taking the real part of the trace of the plaquette then gives

$$\text{ReTr} [U_{\mu\nu}(x)] = \text{Tr} \left[\frac{1}{2} (U_{\mu\nu}(x) + U_{\mu\nu}^\dagger(x)) \right] = N_c - a^4 g^2 \text{Tr} [(F_{\mu\nu}(x) F^{\mu\nu}(x))] + \mathcal{O}(a^6), \quad (2.37)$$

where N_c is the number of colors. Thus, the Wilson gauge action [38] is

$$S_G^W = \sum_x \sum_{\mu < \nu} \beta \left(1 - \frac{1}{2N_c} \text{Tr} [U_{\mu\nu}(x) + U_{\mu\nu}^\dagger(x)] \right), \quad (2.38)$$

with $\beta = 2N_c/g^2$. This is a sum over each plaquette (we require $\mu < \nu$ in the sum so only one orientation is included) with appropriate constants so as to reproduce the QCD gauge action in the continuum limit with $\mathcal{O}(a^2)$ corrections.

2.5 Lattice Fermion Actions

Fermions are trickier to discretize than the gauge field because the most naïve lattice fermion action does not produce the correct continuum result. To illustrate, we first consider free fermions. Using the symmetric discrete derivative, Eq. (2.14), yields a free fermion action for a single flavor

$$S_{free} = \sum_{x,y} \bar{\psi}_{\bar{\alpha}}(x) K_{\bar{\alpha}\alpha}(x,y) \psi_{\alpha}(y), \quad (2.39)$$

where the quark matrix $K_{\alpha\alpha'}(x,y)$ is given by

$$K_{\bar{\alpha}\alpha}(x,y) = \sum_{\mu} \frac{1}{2} (\gamma_{\mu})_{\bar{\alpha}\alpha} (\delta_{y,x+a\hat{\mu}} - \delta_{y,x-a\hat{\mu}}) + M \delta_{x,y} \delta_{\bar{\alpha},\alpha}. \quad (2.40)$$

The fermion propagator is given by the inverse of the quark matrix:

$$\langle \Omega | \mathcal{T} [\psi_\alpha(y) \bar{\psi}_{\bar{\alpha}}(x)] | \Omega \rangle = K_{\alpha\bar{\alpha}}^{-1}(y, x). \quad (2.41)$$

We can invert the quark matrix in Fourier space to obtain

$$K_{\alpha\bar{\alpha}}^{-1}(y, x) = \int_{-\pi/a}^{\pi/a} \frac{d^4 k}{(2\pi)^4} \frac{\left(-i \sum_\mu \gamma_\mu \frac{1}{a} \sin(k_\mu a) + M\right)_{\alpha\bar{\alpha}}}{\left(\frac{1}{a} \sum_\mu \sin(k_\mu a)\right)^2 + M^2} e^{ik(y-x)}. \quad (2.42)$$

The momenta are constrained to the Brillouin zone in momentum space, $-\pi/a < k_\mu \leq \pi/a$. Taking the $a \rightarrow 0$ limit, the lattice propagator is finite and converges to the continuum propagator as $k_\mu \rightarrow 0$. However, the propagator also has a continuum limit as k_μ approaches the corners of the Brillouin zone, $k_\mu \rightarrow (0, 0, 0, \pi/a), (0, 0, \pi/a, 0), \dots, (\pi/a, \pi/a, \pi/a, \pi/a)$. The continuum limit of the lattice propagator has a total of 16 single particle states with the same energy as the zero-momentum states. One represents the physical particle, while the other 15 are lattice artifacts known as “doubblers”.

While it may seem that this doubling problem is a result of our particular choice of discretization, Nielsen and Ninomiya [39] showed that the phenomenon is a property of lattice fermion actions which have a few very general properties: hermiticity, locality, translational invariance, and chiral symmetry in the zero quark mass limit. To solve the doubling problem it is necessary to abandon one of these properties.

Wilson’s solution [40] to the doubling problem adds a new term to the action which disappears in the continuum limit and breaks chiral symmetry. The propagator for this new action only has a continuum limit for $k_\mu \rightarrow 0$, eliminating the

doublers. The free Wilson action is (for a single quark flavor)

$$S_{Wilson,free} = S_{free} - \frac{ra}{2} \sum_{x,\mu} \bar{\psi}(x) \Delta_\mu \psi(x), \quad (2.43)$$

$$= \sum_{x,y} \bar{\psi}_{\bar{\alpha}}(x) K_{\bar{\alpha}\alpha}(x,y) \psi_\alpha(y), \quad (2.44)$$

$$K_{\bar{\alpha}\alpha}(x,y) = (M + 4r) \delta_{x,y} \delta_{\bar{\alpha},\alpha} - \frac{1}{2} \sum_{\mu} [(r - \gamma_\mu)_{\bar{\alpha}\alpha} \delta_{y,x+a\hat{\mu}} + (r + \gamma_\mu)_{\bar{\alpha}\alpha} \delta_{y,x-a\hat{\mu}}], \quad (2.45)$$

where r is the Wilson parameter, typically set to 1.

To include the interactions between quarks and gluons, we include a gauge link in the discretized derivatives as in Eq. (1.12). This gives

$$S_{Wilson} = \sum_A \sum_{x,y} \bar{\psi}_{\bar{c}\bar{\alpha}}^A(x) K_{\bar{c}\bar{\alpha};c\alpha}^A(x,y) \psi_{c\alpha}^A(y), \quad (2.46)$$

$$K_{\bar{c}\bar{\alpha};c\alpha}^A(x,y) = (M^A + 4r) \delta_{x,y} \delta_{\bar{\alpha},\alpha} \delta_{\bar{c},c} - \frac{1}{2} \sum_{\mu} [(r - \gamma_\mu)_{\bar{\alpha}\alpha} U_\mu(x)_{\bar{c}c} \delta_{y,x+a\hat{\mu}} + (r + \gamma_\mu)_{\bar{\alpha}\alpha} U_\mu^\dagger(x)_{\bar{c}c} \delta_{y,x-a\hat{\mu}}]. \quad (2.47)$$

$\psi_{c\alpha}^A(x)$ is a quark field of flavor A , color c , and spin α .

2.6 Extracting Excited State Energies

In order to extract the energies of baryon states, we must connect the Euclidean path integrals to eigenstates of the quantum mechanical Hamiltonian. This is accomplished with the transfer operator \hat{T} , which translates a state one lattice unit in time along the imaginary time axis,

$$\hat{T} = e^{-\hat{H}a}. \quad (2.48)$$

To calculate the vacuum expectation value of an operator \mathcal{O} , we multiply on the left by \hat{T}^N and take a trace:

$$\text{Tr} \left(\hat{T}^N \mathcal{O} \right) = \text{Tr} \left(e^{-H(Na)} \mathcal{O} \right) = \sum_{n=1}^{\infty} e^{-E_n t} \langle n | \mathcal{O} | n \rangle, \quad (2.49)$$

with $t = Na$. Taking the limit $N \rightarrow \infty$, we project out only the $n = 0$ state (the vacuum) to get

$$\langle \Omega | \mathcal{O} | \Omega \rangle = \frac{1}{Z} \int D[\psi] D[\bar{\psi}] D[U] \mathcal{O}(\psi, \bar{\psi}, U) e^{-S[\psi, \bar{\psi}, U]} = \lim_{N \rightarrow \infty} \frac{\text{Tr} \left(\hat{T}^N \mathcal{O} \right)}{\text{Tr} \left(\hat{T}^N \right)}, \quad (2.50)$$

$$= \lim_{t \rightarrow \infty} \frac{\text{Tr} \left(e^{-Ht} \mathcal{O} \right)}{\text{Tr} \left(e^{-Ht} \right)}. \quad (2.51)$$

The existence of the transfer operator is necessary to extract QCD observables from the Euclidean formulation.

To extract the energies of QCD energies, we consider an operator $\bar{\mathcal{O}}$ which creates some superposition of energy eigenstates and its corresponding annihilation operator \mathcal{O} . We calculate the correlation function $\langle \Omega | \mathcal{T} [\mathcal{O}(t_f) \bar{\mathcal{O}}(t_i)] | \Omega \rangle$:²

$$\begin{aligned} C(t) &= \langle \Omega | \mathcal{O}(t_f) \bar{\mathcal{O}}(t_i) | \Omega \rangle \\ &= \langle \Omega | e^{H(t_f - t_i)} \mathcal{O}(t_i) e^{-H(t_f - t_i)} \bar{\mathcal{O}}(t_i) | \Omega \rangle, \end{aligned} \quad (2.52)$$

$$= \sum_{n=1}^{\infty} \langle \Omega | \mathcal{O}(t_i) | n \rangle \langle n | \bar{\mathcal{O}}(t_i) | \Omega \rangle e^{-E_n t}. \quad (2.53)$$

²In general, correlation functions will be the time ordered vacuum expectation value of a creation operator acting at time t_i and an annihilation operator acting at time t_f . We will write the correlators as a function of $t = t_f - t_i$. We will assume $t_f > t_i$ and for brevity omit the time ordering operator. Statements made in this work about correlators will generally be true regardless of the time ordering.

In the limit $t \rightarrow \infty$, the sum in Eq. (2.53) is dominated by the lowest energy eigenstate which couples to \mathcal{O} . Note that we are essentially calculating a matrix element of the operator $e^{-H(t_f-t_i)}$:

$$\langle \Omega | \mathcal{O}(t_f) \bar{\mathcal{O}}(t_i) | \Omega \rangle = \langle \Psi | e^{-H(t_f-t_i)} | \Psi \rangle, \quad (2.54)$$

$$| \Psi \rangle = \bar{\mathcal{O}}(t_i) | \Omega \rangle, \quad (2.55)$$

$$\langle \Psi | = \langle \Omega | \mathcal{O}(t_i) \quad (2.56)$$

2.6.1 The Variational Method

The energies of excited states are best extracted by extending the method above. We start with a set of N creation operators $\{\bar{\mathcal{O}}_I\}$, $I = 1 \dots N$ and corresponding annihilation operators. We compute the correlation matrix

$$C_{IJ}(t) = \langle \Omega | \mathcal{O}_I(t_f) \bar{\mathcal{O}}_J(t_i) | \Omega \rangle, \quad (2.57)$$

$$\equiv \langle \Psi_I | e^{-H(t_f-t_i)} | \Psi_J \rangle, \quad (2.58)$$

and solve the eigenvalue problem

$$C_{IJ}(t) v_{nJ} = \lambda_n(t) v_{nI}, \quad (2.59)$$

where the $\lambda_n(t)$ are the time-dependent eigenvalues of the correlation matrix and the v_{nI} are the corresponding time-independent eigenvectors. It is shown in [41] that the eigenvalues are

$$\lambda_n(t) = e^{-E_n t} [1 + \mathcal{O}(e^{-\Delta_n t})], \quad (2.60)$$

$$\Delta_n = \min_i |E_i - E_n|. \quad (2.61)$$

For sufficiently large times, each eigenvalue can be modeled as an exponential decay with a decay constant equal to the n^{th} energy level in the spectrum and we can obtain the energy by fitting the eigenvalue as a function of time. We can also calculate the effective energy,

$$E_{eff} = \ln \left(\frac{\lambda_n(t)}{\lambda_n(t+1)} \right), \quad (2.62)$$

$$= aE_n \left(1 + \mathcal{O}(e^{-\Delta_n t}) \right). \quad (2.63)$$

As t increases, the effective energy plateaus to constant value. This provides a useful visualization of the quality of the data as well as an estimate of an energy level. The dominant correction is from the state closest in energy. A superior method, which reduces the corrections in Eq. (2.60), is to solve the generalized eigenvalue problem

$$C_{IJ}(t)v_{nJ} = \lambda_n(t)C_{IJ}(t_0)v_{nJ}, \quad (2.64)$$

for some value of t_0 . The eigenvectors of the generalized problem diagonalize the projection of the transfer operator into the subspace spanned by the $\{|\Psi_I\rangle\}$. In [42] it is shown that for an appropriate choice of t_0 , the eigenvalues of this generalized problem are

$$\lambda_n(t) = e^{-E_n(t-t_0)} \left[1 + \mathcal{O}(e^{-(E_{N+1}-E_n)t}) \right]. \quad (2.65)$$

The dominant correction is not from the closest energy state, but rather from the $(N+1)^{\text{th}}$ state.

To show this, we first solve the problem where the correlation matrix has

contributions from only the N lowest energy eigenstates,

$$C_{IJ}^{(0)}(t) = \sum_{n=1}^N Z_{nI}^* Z_{nJ} e^{-E_n t}, \quad (2.66)$$

$$Z_{nI} = \langle n | \Psi_I \rangle, \quad (2.67)$$

and consider contributions from the higher energy eigenstates to be a perturbation on $C_{IJ}^{(0)}(t)$:

$$C_{IJ}(t) = \sum_{n=1}^N Z_{nI}^* Z_{nJ} e^{-E_n t} + \sum_{n=N+1}^{\infty} Z_{nI}^* Z_{nJ} e^{-E_n t}, \quad (2.68)$$

$$\equiv C_{IJ}^{(0)}(t) + C_{IJ}^{(1)}(t). \quad (2.69)$$

We also define the projection of the Hamiltonian onto the lowest N energy eigenstates:

$$H^{(0)} = \sum_{i=1}^N |i\rangle \langle i|. \quad (2.70)$$

The eigenvalues of the operator $e^{-H^{(0)}t}$ are given by $e^{-E_n t}$, $n \leq N$. We denote the matrix representation of this operator in the basis of energy eigenstates as $\tilde{T}_{ij}^{(0)}(t)$:

$$\tilde{T}_{ij}^{(0)}(t) = \langle i | e^{-H^{(0)}t} | j \rangle = e^{-E_i t} \delta_{ij}. \quad (2.71)$$

$\tilde{T}_{ij}^{(0)}(t)$ and $C_{IJ}^{(0)}(t)$ both have the same rank, and ideally we would like to transform $C_{IJ}^{(0)}(t)$ into $\tilde{T}_{ij}^{(0)}(t)$. These two matrices are related by the transformation

$$C_{IJ}^{(0)}(t) = (Z^\dagger)_{Ii} \tilde{T}_{ij}^{(0)}(t) Z_{jJ}. \quad (2.72)$$

The diagonalization of $C_{IJ}^{(0)}(t)$ is effectively a change of basis, or an orthogonal transformation. Only in the special case where the transformation in Eq. (2.72) is orthogonal ($Z^\dagger = Z^{-1}$) will the diagonalization of $C_{IJ}^{(0)}(t)$ produce $\tilde{T}_{ij}^{(0)}(t)$. This

occurs when the $\{\Psi_I\}$ are orthonormal and Z_{nI} is a unitary matrix, which generally is not true. In fact, it is shown in [41] that the eigenvalues of $C_{IJ}^{(0)}(t)$ are given by Eq. (2.60).

Now we consider the matrix

$$\begin{aligned} T_{IJ}^{(0)}(t) &= [Z^{-1}(Z^\dagger)^{-1}C^{(0)}(t)]_{IJ}. \\ &= (Z^{-1})_{Ii}\tilde{T}_{ij}^{(0)}(t)Z_{jJ}. \end{aligned} \quad (2.73)$$

This matrix is related to $\tilde{T}_{ij}^{(0)}(t)$ by an orthogonal transformation and its diagonalization would produce $\tilde{T}_{ij}^{(0)}(t)$. Diagonalizing $T_{IJ}^{(0)}(t)$ is equivalent to solving the generalized eigenvalue problem

$$C_{IJ}^{(0)}(t)v_{nJ}^{(0)} = \lambda_n^{(0)}(t)(Z^\dagger Z)_{IJ}v_{nJ}^{(0)}. \quad (2.74)$$

Of course, $Z^\dagger Z$ is unknown so we cannot directly solve this problem. We can instead replace $Z^\dagger Z$ with $Z^\dagger \tilde{T}^{(0)}(t_0)Z = C^{(0)}(t_0)$, to obtain the generalized eigenvalue equation

$$C_{IJ}^{(0)}(t)v_{nJ}^{(0)} = \lambda_n^{(0)}(t)C_{IJ}^{(0)}(t_0)v_{nJ}^{(0)}. \quad (2.75)$$

We transform this equation as follows:

$$C_{IJ}^{(0)}(t)v_{nJ}^{(0)} = \lambda_n^{(0)}(t)C_{IJ}^{(0)}(t_0)v_{nJ}^{(0)}, \quad (2.76)$$

$$(Z^\dagger \tilde{T}^{(0)}(t)Z)_{IJ}v_{nJ}^{(0)} = \lambda_n^{(0)}(Z^\dagger \tilde{T}^{(0)}(t_0)Z)_{IJ}v_{nJ}^{(0)}, \quad (2.77)$$

$$\left[(\tilde{T}^{(0)}(t_0)Z)^{-1}(ZZ^{-1})(\tilde{T}^{(0)}(t)Z) \right]_{IJ} v_{nJ}^{(0)} = \lambda_n^{(0)}(t)v_{nJ}^{(0)}, \quad (2.78)$$

$$\left[(Z^{-1}\tilde{T}^{(0)}(t_0)Z)^{-1}(Z^{-1}\tilde{T}^{(0)}(t)Z) \right]_{IJ} v_{nJ}^{(0)} = \lambda_n^{(0)}(t)v_{nJ}^{(0)}, \quad (2.79)$$

$$[(T^{(0)})^{-1}(t_0)T^{(0)}(t)]_{IJ} v_{nJ}^{(0)} = \lambda_n^{(0)}(t)v_{nJ}^{(0)}. \quad (2.80)$$

The last line is satisfied if the vector $v_{nJ}^{(0)}$ is an eigenvector of the transfer operator in the $\{|\Psi\rangle\}$ basis. The corresponding eigenvalue is $\lambda_n^{(0)} = e^{-E_n(t-t_0)}$. This demonstrates the superiority of the generalized eigenvalue problem, Eq. (2.64) over the standard eigenvalue problem, Eq. (2.59). In the generalized problem, when the rank of the correlation matrix is equal to the rank of the Hamiltonian, the eigenvectors of the correlator matrix are the eigenvectors of the transfer matrix. The corresponding eigenvalues each have contributions from a single state. Mixing between energy eigenstates only occurs when we consider the corrections from $C_{IJ}^{(1)}(t)$. In the standard problem, however, mixing between energy eigenstates generally occurs even in the $C_{IJ}^{(0)}(t)$ problem.

We return now to the full correlation matrix in Eq. (2.69) and calculate the perturbative corrections due to $C_{IJ}^{(1)}(t)$. The first order corrections to the eigenvalues are

$$\lambda_n^{(1)}(t) = v_{nI}^{(0)*} \left(C_{IJ}^{(1)}(t) - \lambda_n^{(0)} C_{IJ}^{(1)}(t_0) \right) v_{nJ}^{(0)}. \quad (2.81)$$

From the definition of $C_{IJ}^{(1)}(t)$, it is clear that this expression only involves energies larger than E_N . The eigenvalues, including the dominant first order correction are

$$\lambda_n = e^{-E_n(t-t_0)} \left[1 + \mathcal{O}(e^{-(E_{N+1}-E_n)(t-t_0)}) \right]. \quad (2.82)$$

The first order correction to the eigenvector is

$$v_{nI}^{(1)} = \sum_{m \neq n} \frac{1}{v_{mI}^{(0)*} C_{IJ}^{(0)}(t_0) v_{mJ}^{(0)}} \frac{v_{mI}^{(0)*} \left[C_{IJ}^{(1)}(t) - \lambda_n^{(0)} C_{IJ}^{(1)}(t_0) \right] v_{nJ}^{(0)}}{\lambda_n^{(0)} - \lambda_m^{(0)}} v_{mJ}^{(0)}. \quad (2.83)$$

Following [42], we rewrite

$$(\lambda_n^{(0)} - \lambda_m^{(0)})^{-1} = (\lambda_n^{(0)})^{-1} \sum_{k=0}^{\infty} e^{-k(E_m - E_n)(t-t_0)}, \quad (2.84)$$

to obtain

$$v_{nI}^{(1)} = \sum_{m \neq n} \frac{1}{v_{mI}^{(0)*} C_{IJ}^{(0)}(t_0) v_{mJ}^{(0)}} v_{mI}^{(0)*} [C_{IJ}^1(t) - \lambda_n^{(0)} C_{IJ}^1(t_0)] v_{nJ}^{(0)} (\lambda_n^{(0)})^{-1} \sum_{k=0}^{\infty} e^{-k(E_m - E_n)(t - t_0)} v_{mJ}^{(0)}. \quad (2.85)$$

This correction includes contributions from all energy levels, not just those above the N^{th} level. The corrections from energy levels with $E_n < E_{N+1}$ will show up in the higher order corrections to the eigenvalues.

The second order correction to the eigenvalue is

$$\lambda_n^{(2)} = \frac{1}{v_{nI}^{(0)*} C_{IJ}^{(0)}(t_0) v_{nJ}^{(0)}} \left[v_{nI}^{(0)*} \left(\overbrace{C_{IJ}^{(1)}(t)}^1 - \overbrace{\lambda_n^{(1)} C_{IJ}^0(t_0)}^2 - \overbrace{\lambda_n^{(0)} C_{IJ}^{(1)}(t_0)}^3 \right) v_{nJ}^{(1)} - \lambda_n^{(1)} v_{nI}^{(0)*} C_{IJ}^{(1)}(t_0) v_{nJ}^{(0)} \right]. \quad (2.86)$$

We consider the three terms involving $v_{nJ}^{(1)}$, labeling the individual terms using overbraces to aid in the discussion. Term 1 involves $C_{IJ}^{(1)}(t)$, introducing corrections which are suppressed by at least $e^{-E_{N+1}t}$. Similarly, term 2 has a factor of $\lambda_n^{(1)} \sim e^{-(E_{N+1} - E_n)(t - t_0)}$. The corrections due to these two terms are, at worst, $\mathcal{O}(e^{-(E_{N+1} - E_n)(t - t_0)})$ and at least as small as the first order corrections to the eigenvalue. The dominant contribution from term 3 is

$$\sum_{m \neq n} \frac{-\lambda_n^{(0)} |v_{nI}^{(0)*} C_{IJ}^{(1)}(t_0) v_{mJ}^{(0)}|^2}{(v_{nI}^{(0)*} C_{IJ}^{(0)}(t_0) v_{nJ}^{(0)}) (v_{mI}^{(0)*} C_{IJ}^{(0)}(t_0) v_{mJ}^{(0)})} \sum_{k=0}^{\infty} e^{-k(E_m - E_n)(t - t_0)}. \quad (2.87)$$

This term contains mixing between all energy levels, not just those higher than E_N and the dominant correction is $\mathcal{O}(e^{-2E_n t_0} e^{-\Delta_n(t - t_0)})$. By choosing t_0 sufficiently large, we can achieve $e^{-2E_n t_0} e^{-\Delta_n t_0} \ll e^{-(E_{N+1} - E_n)(t - t_0)}$ and the eigenvalues will be described by Eq. (2.82). As discussed in [42], with such a choice of t_0 , corrections

from higher orders of perturbation theory will be similarly suppressed. In practice, the correlator's signal-to-noise ratio decays with time and as we push t_0 to larger values, the signal quality decays. We will need to optimize the choice of t_0 to balance these considerations, ideally selecting a sufficiently large value of t_0 such that Eq. (2.82) holds without significantly harming the signal quality.

2.7 The Monte Carlo Method

To compute the correlator matrix, we perform the numerical calculation of the path integral using Monte Carlo integration. Consider a function $f(x)$ where x is a k -dimensional vector (x_1, \dots, x_k) , and an ensemble of N random k -dimensional vectors x^j , $j = 1 \dots N$ on a domain \mathcal{D} , selected according to a probability density $P(x)$. From the Law of Large Numbers we have

$$\mathbb{E}[f(x)] = \int_{\mathcal{D}} d^k x f(x) P(x) \approx \frac{1}{N} \sum_{j=1}^N f(x^j). \quad (2.88)$$

The ensemble average of $f(x)$ estimates the integral of $g(x) = f(x)P(x)$ on \mathcal{D} . Given an arbitrary $g(x)$, we can always draw our random vectors from a uniform probability density, $P(x) = 1/V$, where V is the volume of \mathcal{D} , and define $f(x) = Vg(x)$. However, if $\int_{\mathcal{D}} d^k x g(x)$ is dominated by a small part of \mathcal{D} , then only a small fraction of the vectors in the uniform ensemble will contribute significantly to the estimate. Ideally, in this situation we would like to write $g(x) = f(x)P(x)$ where $P(x)$ favors vectors in the region of \mathcal{D} which dominates the integral and suppresses vectors which contribute minimally. The variance in this case will be much smaller than for the uniform distribution. This technique is called importance sampling.

In lattice QCD, importance sampling is crucial. We want to calculate integrals of the form

$$\langle \Omega | \mathcal{O} | \Omega \rangle = \frac{1}{Z} \int D[\bar{\psi}] D[\psi] D[U] \mathcal{O}(\bar{\psi}, \psi) e^{-S[\bar{\psi}, \psi, U]}. \quad (2.89)$$

Only configurations which are near the minimum of the action contribute significantly to the integral. With a uniform ensemble, most of the configurations would be very far away from the minimum and their contribution would be exponentially suppressed. We would require an impossibly large number of configurations to obtain an estimate of the path integral with a reasonable uncertainty. In practice we use the e^{-S} factor in the path integral as the probability density function for the importance sampling of field configurations. The e^{-S} is analogous to the Boltzmann factor in statistical mechanics. The resulting ensemble favors gauge configurations which contribute significantly to the path integral, allowing us to perform a wide range of calculations with an ensemble size on the order of a few hundred configurations. Note that had we formulated the discretized theory in Minkowski space, the path integral would have a factor of e^{iS_M} , rather than e^{-S} , making a Monte Carlo estimate of the path integral impossible, as e^{iS_M} cannot be regarded as a probability density. It is for this reason that the Euclidean formulation is needed to perform QCD calculations numerically on a computer.

The Grassmann variables in the QCD are not suitable for numerical work on a computer. However, we are able to explicitly integrate out the Grassmann fields

using the the rules of Grassmann integration. We rewrite the path integral as ³

$$\langle \Omega | \mathcal{O} | \Omega \rangle = \frac{1}{Z} \int D[U] e^{-S_G[U]} \int D[\bar{\psi}] D[\psi] \mathcal{O}(\bar{\psi}, \psi, U) e^{\bar{\psi}_{\bar{a}\bar{\alpha}}(x) K_{\bar{a}\bar{\alpha}; a\alpha}(x, y, U) \psi_{a\alpha}(y)}, \quad (2.90)$$

where we have split up the action into the pure gauge and fermion parts and written the fermion part in terms of the quark matrix, explicitly showing its U dependence. For now we assume only one flavor of quark. We integrate a general function of a Grassmann variable, $f(\eta)$, by expanding in a power series in the elements of the algebra. The power series has a finite number of terms:

$$f(\eta) = f_0 + \sum_i f_i \eta_i + \sum_{i \neq j} f_{ij} \eta_i \eta_j + \dots + f_{123\dots N} \eta_1 \eta_2 \dots \eta_N. \quad (2.91)$$

Following Eqs. (2.5) and (2.6) integrating over the quark fields gives

$$\int D[\bar{\psi}] D[\psi] \mathcal{O}(\bar{\psi}, \psi) e^{\bar{\psi}_{\bar{a}\bar{\alpha}}(x) K_{\bar{a}\bar{\alpha}; a\alpha}(x, y, U) \psi_{a\alpha}(y)} = \det(K) f(K^{-1}[U]), \quad (2.92)$$

where $f(K^{-1}[U])$ is some function of elements of the inverse of $K[U]$. Its exact form depends on the particular operator \mathcal{O} . In this work, we will only be concerned with the case where $\mathcal{O} = \psi_{a\alpha}(y) \bar{\psi}_{\bar{a}\bar{\alpha}}(x)$, as we will use Wick's theorem to reduce more complicated operators to single quark propagators. In this case, $f(K^{-1}[U]) = (K^{-1})_{a\alpha; \bar{a}\bar{\alpha}}(y, x, U)$. For multiple flavors of quarks, we get a factor of $\det(K^A[U])$ for each flavor A .

The integral over the gauge field remains:

$$\langle \Omega | \mathcal{O} | \Omega \rangle = \int D[U] f(K^{-1}[U]) e^{-S_G[U]} \prod_A \det(K^A[U]). \quad (2.93)$$

³From now on, we will not explicitly write sums over repeated space-time coordinates. Unless otherwise noted, these summations are implied.

We calculate this integral using the Monte Carlo method, generating an ensemble of gauge configurations with a probability density given by $e^{-S_G} \prod_A \det(K^A[U])$. The calculation of the determinant is the most demanding part of the calculation. For this reason, until recently most calculations were done using the “quenched” approximation, setting $\det(K^A[U]) = 1$ for every configuration. This effectively makes the masses of the sea quarks infinite, eliminating the effects of quark loops. For this work, we use lattices with two and three flavors of dynamical quarks. Our results include the effects of up and down quark loops (for the $N_f = 2$ lattices) as well as strange quark loops (for the $N_f = 2+1$ lattices). The effects of heavier quarks are likely negligible corrections to the energies of the nucleon and delta resonances as these energies are much less than the masses of the charm, bottom, and top quarks.

The determinant is also an issue in dynamical simulations because it is not necessarily positive. The probability density function used in the importance sampling must be positive definite over the domain of possible gauge configurations. As the determinant of the quark matrix may be negative, the probability density may not be positive. This is not a problem for the $N_f = 2$ case, where we simulate only dynamical up and down quarks. We use the same mass parameter for each quark, and therefore the quark matrix is the same for both the up and the down quarks. As a result, the probability density function is $[\det(K^\ell[U])]^2 e^{-S_G[U]}$, where $K^\ell[U]$ is the quark matrix for either of the light quarks. This probability density is clearly positive semi-definite. For other cases, such as the $N_f = 2 + 1$ case, we use $|\det(K[U])| e^{-S[U]}$ as the probability density for the gauge generation. When observables are computed, the phase $\det(K[U])/|\det(K[U])|$ is reinserted.

The ensemble of gauge configurations is generated using a Markov process. A chain of configurations is generated in which the next configuration is produced by proposing a set of changes to individual links in the last configuration. These changes are then either accepted or rejected based on the value of $\prod_A \det(K^A[U])e^{-S_G[U]}$. Starting from the initial state in the chain, the Markov chain must be allowed to “thermalize”. During thermalization, observables such as the average of the plaquette fluctuate wildly from configuration to configuration before finally settling around an average value. Only configurations generated after thermalization are included in the ensemble. Because configurations are generated from previous states in the Markov chain, measurements are likely to be highly correlated from configuration to configuration. Typically we sample only a subset of configurations, sufficiently separated in the Markov chain that the correlations are reduced.

2.8 Calculation Overview

We present an overview of a baryon spectroscopy calculation:

1. The first step in the calculation is to choose a particular discretization of the action and all the associated parameters. Ideally we would like to choose a lattice spacing a and length L such that $L \gg 1/E \gg a$, where E is the energy scale of the spectrum we are studying. Of course, this must be balanced with the availability of computer resources. With improved lattice discretizations, lattice spacing corrections can be made smaller, allowing for the use of a coarser lattice. The lattice spacing is not an actual parameter appearing in

the action and is therefore not chosen a priori. Instead, we choose values for the gauge coupling β and the bare quark masses and measure the lattice spacing by calculating a physical observable. The quark mass parameters are typically chosen such that the pion mass is unphysically heavy because the computational cost of a calculation is inversely related to the pion mass. Only recently have simple calculations been performed near the physical pion mass.

2. Once the lattice parameters have been chosen, an ensemble of gauge configurations is generated. We use importance sampling, generating an ensemble distributed according to $e^{-S_G[U]} \prod_A \det(K^A[U])$. We typically use several hundred gauge configurations for a spectroscopy calculation.
3. We select a set of baryon creation operators (and corresponding annihilation operators), as described in the next chapter. These operators are optimized for the calculation of the low-lying baryon spectrum and for the identification of the continuum state corresponding to each lattice state. We calculate quark propagators in each gauge configuration and tie them together into three quark baryon propagators. By taking appropriate combinations of the three quark propagators, we obtain the correlation functions for the baryon operators. After calculating these correlation functions in every configuration, we take an ensemble average to obtain estimates of quantum mechanical path integrals.
4. We use the variational method to extract the baryon spectrum, diagonalizing the ensemble averaged correlation matrices. For sufficiently large times, the eigenvalues of the diagonalized correlation matrix can be fit with a single

exponential decay. The decay constant is an energy in the spectrum.

5. All calculated energies are in units of a^{-1} . We determine the lattice spacing by measuring an experimentally known physical observable on the lattice. A comparison of the experimental value and the lattice measurement provides us with a conversion factor between the lattice units and physically relevant units. As we are typically working on lattices with an unphysically heavy pion, we choose an observable which is insensitive to the pion mass. Once the lattice spacing is known, we can convert all the calculated energies to physical units.

2.8.1 Error Analysis

The final step in the calculation is to estimate the statistical uncertainties in the computed quantities. The Monte Carlo estimate for a quantity x such as a correlation function is given by the ensemble average \bar{x} ,

$$\bar{x} = \frac{1}{N} \sum_{i=1}^N x_i, \quad (2.94)$$

where x_i is the measured value of x in configuration i . The statistical uncertainty in the ensemble average is

$$\Delta\bar{x} = \frac{\sigma_x}{\sqrt{N}}, \quad (2.95)$$

where σ_x is the standard deviation,

$$\sigma_x^2 = \frac{1}{N-1} \sum_{i=1}^N (\bar{x} - x_i)^2. \quad (2.96)$$

Many observables are computed from ensemble averaged quantities which cannot be computed on individual configurations. To calculate an excited energy spec-

trum, we first diagonalize the ensemble averaged correlation matrix and then extract the energies from the eigenvalues via either a fit or an effective energy calculation. It does not make sense to do this on a single configuration. The standard deviation is therefore not a useful tool for estimating the statistical uncertainty in energy spectrum calculations. Instead, we use resampling techniques in which we measure the energy spectrum on subsets of the ensemble. We extract the spectrum from the subset averaged correlator matrix using the same procedure as for the entire ensemble. We then use the spread in the measurements from different subsets to estimate the statistical uncertainty in the calculated energy levels. In particular, we use the jackknife method [43], in which the subsets are obtained by eliminating a single configuration from the ensemble.

The i^{th} jackknife estimate of x , which we denote $x^{(i)}$, is the average of x over the entire ensemble, excluding the i^{th} configuration,

$$x^{(i)} = \frac{1}{N-1} \sum_{j \neq i} x_j. \quad (2.97)$$

The jackknife estimate of x is given by the average of the $x^{(i)}$:

$$\bar{x}_{jack} = \frac{1}{N} \sum_{i=1}^N x^{(i)}, \quad (2.98)$$

and the uncertainty is given by

$$\Delta \bar{x}_{jack} = \sigma_{x,jack}, \quad (2.99)$$

with the jackknife variance $\sigma_{x,jack}^2$ given by

$$\sigma_{x,jack}^2 = \left(\frac{N-1}{N} \right) \sum_{i=1}^N (\bar{x}_{jack} - x^{(i)})^2. \quad (2.100)$$

With these definitions, $\bar{x} = \bar{x}_{jack}$ and $\Delta\bar{x} = \Delta\bar{x}_{jack}$. The only difference between the two methods is that we calculate the jackknife quantities from the averaged jackknife ensembles rather than individual configurations. This allows us to estimate the statistical uncertainty for quantities which cannot be calculated on a single configuration.

Applying this to a spectrum calculation, we first calculate the ensemble average of the correlation functions and apply the variational method to obtain an estimate of the energies of the spectrum. The diagonalization and subsequent extraction of the energies is then repeated on each jackknife sample. We use Eq. (2.99) as the uncertainty in the Monte Carlo estimate.

Chapter 3

Optimized Baryon Operators

A considerable effort has been undertaken by the Hadron Spectrum Collaboration to design a set of optimal operators to extract the low lying QCD energy spectrum via the variational method [44, 45]. Ideally, these operators should transform as irreducible representations (irreps) of the lattice symmetry group and couple well to the low-lying spectrum. Furthermore, we would like to connect the extracted lattice states to continuum baryon states with fixed flavor content, momentum, parity, and spin. We construct the operators by first forming a large set of building blocks or “elemental operators” as described in Section 3.1. The elemental operators are then made translationally invariant so that they couple only to zero-momentum states. This is described in 3.2. As described in Section 3.3, we take linear combinations of these elemental operators to form operators with definite isospin and strangeness. The flavor symmetries of the Lagrangian are unaffected by the transition to the lattice so we can use the quark model as a guide to construct operators with the proper flavors.

States of definite parity and angular momentum are related to the symmetries of physical space, which are very different in the continuum and on the lattice. We form operators which transform as irreps of the lattice rotation group with spatial inversion. These irreps have definite parity but identifying the continuum

spins of lattice states is trickier. In particular, there are only a finite number of irreps of the lattice rotation group, whereas the continuum $O(3)$ rotation group has an infinite number of irreps. Furthermore, the lattice irreps have a maximal dimension of four, meaning that continuum states with spin- $\frac{5}{2}$ or greater (continuum irreps with a dimension greater than four) must occur on the lattice across several irreps. We can identify the continuum spins of the lattice states by subducing the continuum rotation group to the lattice rotation group and identifying patterns of degeneracies across the lattice irreps. We describe the lattice rotation group with spatial inversion, as well as the procedure for projecting the operators onto irreps of the group, in Section 3.4

3.1 The Building Blocks

The simplest baryon operator is the product of three single quark operators acting at the same point in space time:

$$\bar{B}_{\bar{\alpha}\bar{\beta}\bar{\gamma}}^{\bar{A}\bar{B}\bar{C}}(x) = \epsilon_{\bar{a}\bar{b}\bar{c}} \bar{\psi}_{\bar{a}\bar{\alpha}}^{\bar{A}}(x) \bar{\psi}_{\bar{b}\bar{\beta}}^{\bar{B}}(x) \bar{\psi}_{\bar{c}\bar{\gamma}}^{\bar{C}}(x). \quad (3.1)$$

The flavor of the quarks is indicated by the capital Roman indices, the color by the lower case Roman indices, and the spin by the Greek indices. The color indices are contracted with the antisymmetric Levi-Civita symbol to produce a gauge-invariant color singlet.

In general, an operator of this form will not be ideal for extracting the low lying QCD energy spectrum. Instead we use smeared quark and gauge fields to reduce the coupling to high lying energy eigenstates, and we covariantly displace

the quarks with respect to each other to capture the radial and orbital structure of low lying states. Three-quark operators built from smeared, displaced single-quark operators form the set of elemental operators.

3.1.1 Quark Smearing

Instead of creating a point source, we can emulate the spatial wave functions of the quarks in low-lying baryons by “smearing” the field operators, taking a weighted average of the field operator at a lattice site with operators at nearby sites. This effectively reduces coupling to high energy, short-wavelength states [46]. The simplest smearing method is Gaussian smearing [47], in which the smeared field at a site is the Gaussian weighted average of surrounding lattice sites. In the continuum, we can define the Gaussian smeared field as

$$\tilde{\psi}(\vec{x}) = e^{\sigma^2 \vec{\nabla}^2 / 2} \psi(\vec{x}), \quad (3.2)$$

where σ is the Gaussian radius. We make the substitution

$$e^x = \lim_{n_\sigma \rightarrow \infty} \left(1 + \frac{x}{n_\sigma} \right)^{n_\sigma}, \quad (3.3)$$

to approximate the Gaussian smearing on the lattice with (no summation over temporal variables)

$$\tilde{\psi}_{a\alpha}^A(\vec{x}, t) = J_{ab}(\vec{x}, \vec{y}, t) \psi_{b\alpha}^A(\vec{y}, t), \quad (3.4)$$

$$\tilde{\bar{\psi}}_{\bar{a}\bar{\alpha}}^A(\vec{x}, t) = \bar{\psi}_{\bar{b}\bar{\alpha}}^A(\vec{y}, t) J_{b\bar{a}}^*(\vec{y}, \vec{x}, t), \quad (3.5)$$

$$J_{ab}(\vec{x}, \vec{y}, t) = \left(1 + \frac{\sigma^2 \Delta(\vec{x}, \vec{y}, t)}{2n_\sigma} \right)_{ab}^{n_\sigma}, \quad (3.6)$$

for some finite n_σ and with¹

$$\Delta(\vec{x}, \vec{y}, t) = \sum_i \left(U_i(\vec{x}, t) \delta_{\vec{y}, \vec{x} + \hat{i}} + U_i^\dagger(\vec{x} - \hat{i}, t) \delta_{\vec{y}, \vec{x} - \hat{i}} - 2\delta_{\vec{x}, \vec{y}} \right), \quad (3.7)$$

the matrix representation of the gauge-covariant lattice Laplacian operator. In effect, we are using a Gaussian weight to favor low momentum modes and suppress higher modes. The Gaussian radius σ and the number of iterations n_σ will be optimized for the calculation of the low lying energy spectrum

3.1.2 Gauge Link Smearing

The operators can be further improved by replacing the gauge links which appear in the smearing matrix, Eq. (3.6), with smeared gauge links. Gauge link smearing typically is a weighted average of a spatial link $U_i(x)$ with the spatial “staples” originating at \vec{x} and ending at $\vec{x} + \hat{i}$. We denote the sum of the spatial staples $C_i(\vec{x})$:

$$C_i(x) = \sum_{j \neq i} \left(U_j(x) U_i(x + \hat{j}) U_j^\dagger(x + \hat{i}) + U_j^\dagger(x - \hat{j}) U_i(x - \hat{j}) U_j(x - \hat{j} + \hat{i}) \right). \quad (3.8)$$

The averaging may be repeated for several iterations.

After averaging, the gauge-links need to be projected back into the SU(3) group, which can be computationally expensive. We avoid this projection by using stout smearing [48] in which each iterate is, in fact an element of SU(3). We define

¹From now on we will be working in units with $a = 1$.

the n^{th} iterate $U_i^{[n]}$ to be

$$U_i^{[n]}(x) = \exp \left(i \rho \Theta_i^{[n-1]}(x) \right) U_i^{[n-1]}(x), \quad (3.9)$$

$$\Theta_i^{[n]}(x) = \frac{i}{2} \left(\Omega_i^{[n]\dagger}(x) - \Omega_i^{[n]}(x) \right) - \frac{i}{6} \text{Tr} \left(\Omega_i^{[n]\dagger}(x) - \Omega_i^{[n]}(x) \right), \quad (3.10)$$

$$\Omega_i^{[n]}(x) = C_i^{[n]}(x) U_i^{[n]\dagger}(x), \quad (3.11)$$

where $U_i^{[0]}(x)$ is the unsmeared field, and the smeared field is $\tilde{U}_i(x) = U_i^{[n_\rho]}(x)$.

The staple weight ρ and the number of iterations n_ρ will also be optimized for the calculation of the low lying spectrum. Fig. 3.1 from [49] shows how quark and gauge link smearing improve the effective energies of nucleon operators. The quark smearing reduces the coupling to higher energy states and thus improves the plateau of the effective energy. The gauge-link smearing reduces the noise. The combination of the two is especially important for the operators with displaced quarks.

3.1.3 Displacements

To capture orbital and radial excitations of the quark fields, we include operators in which the quarks are displaced with respect to one another. This discussion of displaced baryon operators follows [45]. We include a gauge link in the construction of a displaced quark operator to maintain gauge invariance. We define the displaced quark sink operators $\left[\tilde{D}_j^{(p)} \tilde{\psi} \right](x)$ with a displacement length of p links in the j direction ($j = \pm 1, \pm 2, \pm 3$) as

$$\left[\tilde{D}_j^{(p)} \tilde{\psi} \right](x) = \tilde{U}_j(x) \tilde{U}_j(x + \hat{j}) \dots \tilde{U}_j(x + (p-1)\hat{j}) \tilde{\psi}(x + p\hat{j}). \quad (3.12)$$

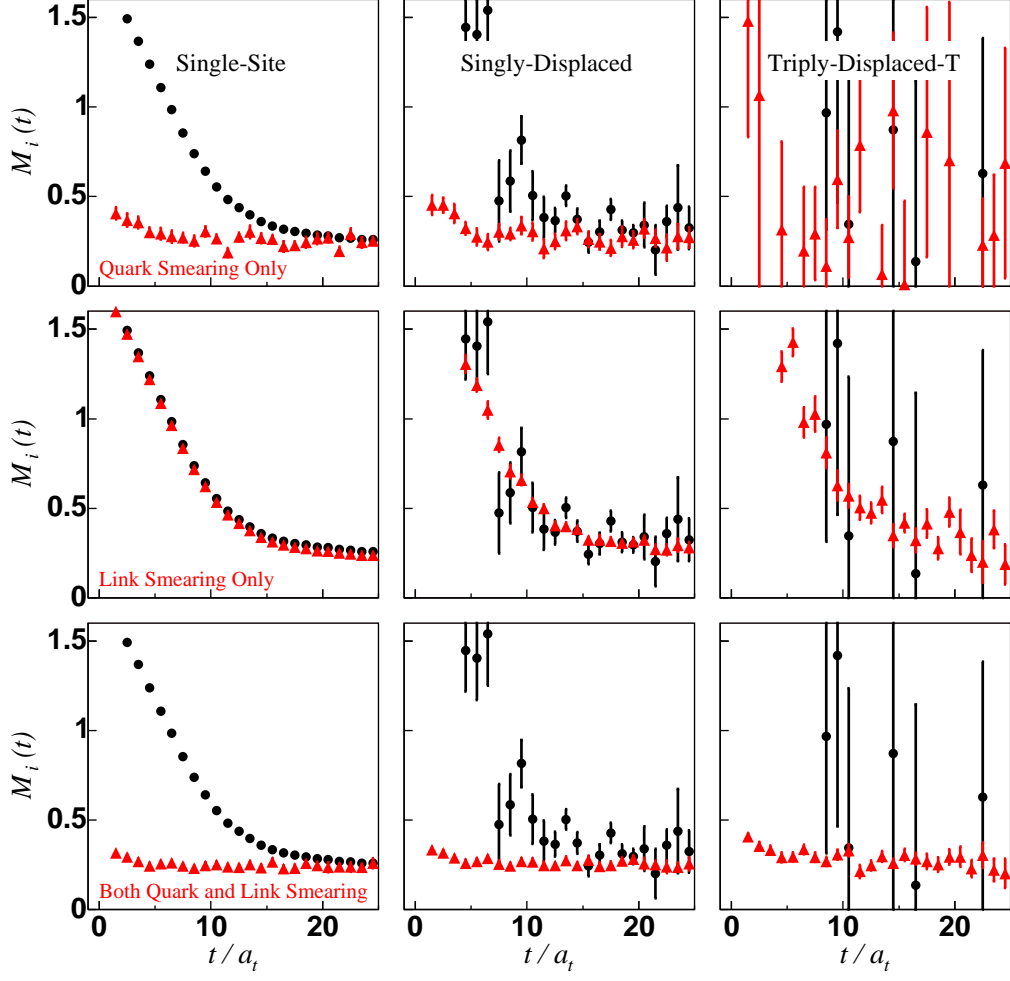


Figure 3.1: From [49], a comparison of the effective energies of three different nucleon operators (See Section 3.1.3 for a description of the operators) with (red triangles) and without smearing (black circles). Results are based on 50 quenched configurations on $12^3 \times 48$ anisotropic Wilson lattices with $a_s \sim 0.1$, $a_s/a_t \sim 3.0$, and $m_\pi = 700$ MeV. The top row shows quark smearing only with $n_\sigma = 32$ and $\sigma = 4.0$. The middle row shows stout link smearing only with $n_\rho = 16$ and $n_\rho \rho = 2.5$. The bottom row shows both quark and link smearing.

Likewise the displaced source operators are

$$\left[\tilde{\psi} \tilde{D}_j^{(p)\dagger} \right] (x) = \tilde{\psi}(x + p\hat{j}) \tilde{U}_j^\dagger(x + (p-1)\hat{j}) \dots \tilde{U}_j^\dagger(x + \hat{j}) \tilde{U}_j^\dagger(x). \quad (3.13)$$

For convenience of notation we also define a zero displacement operator

$$\left[\tilde{D}_0^{(p)} \tilde{\psi} \right] (x) = \tilde{\psi}(x) \quad (3.14)$$

We can write a matrix representation of the displacement operator

$$\left(\tilde{D}_j^{(p)} \right)_{ab} (\vec{x}, \vec{y}, t) = \left(\tilde{U}_j(\vec{x}, t) \tilde{U}_j(\vec{x} + \hat{j}, t) \dots \tilde{U}_j(\vec{x} + (p-1)\hat{j}, t) \right)_{ab} \delta_{\vec{y}, \vec{x} + p\hat{j}}, \quad (3.15)$$

such that (no summation over temporal variables)

$$\left[\tilde{D}_j^{(p)} \tilde{\psi} \right]_{a\alpha} (\vec{x}, t) = \left(\tilde{D}_j^{(p)} \right)_{ab} (\vec{x}, \vec{y}, t) \psi_{b\beta}(\vec{y}, t), \quad (3.16)$$

$$\left[\tilde{\psi} \tilde{D}_j^{(p)\dagger} \right]_{\bar{a}\bar{\alpha}} (\vec{x}, t) = \bar{\psi}_{\bar{b}\bar{\beta}}(\vec{y}, t) \left(\tilde{D}_j^{(p)} \right)_{\bar{b}\bar{\alpha}}^* (\vec{y}, \vec{x}, t). \quad (3.17)$$

The elemental baryon creation operators are then

$$\bar{\Phi}_{\bar{\alpha}\bar{\beta}\bar{\gamma};\bar{i}\bar{j}\bar{k}}^{\bar{A}\bar{B}\bar{C}}(x) = \epsilon_{\bar{a}\bar{b}\bar{c}} \left[\tilde{\psi} \tilde{D}_{\bar{i}}^{(p)\dagger} \gamma_4 \right]_{\bar{a}\bar{\alpha}}^{\bar{A}}(x) \left[\tilde{\psi} \tilde{D}_{\bar{j}}^{(p)\dagger} \gamma_4 \right]_{\bar{b}\bar{\beta}}^{\bar{B}}(x) \left[\tilde{\psi} \tilde{D}_{\bar{k}}^{(p)\dagger} \gamma_4 \right]_{\bar{c}\bar{\gamma}}^{\bar{C}}(x), \quad (3.18)$$

and the elemental baryon annihilation operators are

$$\Phi_{\alpha\beta\gamma;ijk}^{ABC}(y) = \epsilon_{abc} \left[\tilde{D}_i^{(p)} \tilde{\psi} \right]_{a\alpha}^A(y) \left[\tilde{D}_j^{(p)} \tilde{\psi} \right]_{b\beta}^B(y) \left[\tilde{D}_k^{(p)} \tilde{\psi} \right]_{c\gamma}^C(y). \quad (3.19)$$

An explicit factor of γ_4 is inserted into the creation operators so that the resulting correlation matrices are Hermitian. As a simplification, we require the displacement length for all three quarks to be the same.

We also restrict the operators to particular patterns of displacements. These include single-site operators, with no displaced quarks; singly-displaced operators

with only one displaced quark; doubly-displaced-I operators with two quarks displaced in opposite directions; doubly-displaced-L operators with two quarks displaced in different directions; and triply-displaced-T operators with all three quarks displaced to form a “T” shape. The singly-displaced operators model the possibility that the baryon is dominated by a diquark-quark structure. The doubly-displaced operators model the possibility of the Δ -flux formation of the gluon field, while the triply-displaced operators model Y -flux formation. These operators are summarized in Table 3.1.

3.2 Momentum Projections

In this work we are interested in the energy of zero-momentum states. Our operators must therefore be translationally invariant in space. This is accomplished via a summation over all spatial points on a given time slice. The resulting operators depend only on time:

$$\Phi_{\alpha\beta\gamma;ijk}^{ABC}(t) = \frac{1}{L^3} \sum_{\vec{x}} \Phi_{\alpha\beta\gamma;ijk}^{ABC}(\vec{x}, t), \quad (3.20)$$

$$\bar{\Phi}_{\bar{\alpha}\bar{\beta}\bar{\gamma};\bar{i}\bar{j}\bar{k}}^{\bar{A}\bar{B}\bar{C}}(t) = \frac{1}{L^3} \sum_{\vec{x}} \bar{\Phi}_{\bar{\alpha}\bar{\beta}\bar{\gamma};\bar{i}\bar{j}\bar{k}}^{\bar{A}\bar{B}\bar{C}}(\vec{x}, t). \quad (3.21)$$

3.3 Flavor Projections

In designing the operators, we consider only baryons with light valence quarks: up, down, or strange. The mass splitting between the up and down quarks is approximately 1% of the mass of the lightest baryon, the proton. Thus, to a good approximation, the QCD Lagrangian has an SU(2) isospin symmetry. On the lat-

Table 3.1: Patterns of displacements for baryon operators. The left column gives a pictorial representation of the operators. A filled circle represents the location of a smeared quark operator. The right column gives the corresponding displacement indices for that operator type.





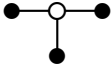
Operator type	Displacement indices
 Single-Site	$i = j = k = 0$
 Singly-Displaced	$i = j = 0, k \neq 0$
 Doubly-Displaced-I	$i = 0, j = -k, k \neq 0$
 Doubly-Displaced-L	$i = 0, j \neq k , jk \neq 0$
 Triply-Displaced-T	$i = -j, j \neq k , jk \neq 0$

Table 3.2: Quark model flavor wave functions for zero strangeness light baryons. Isospin I and isospin projection I_3 is also listed.

Flavor	I	I_3	Baryon
uuu	$\frac{3}{2}$	$\frac{3}{2}$	Δ^{++}
$\frac{1}{\sqrt{3}}(uud + udu + duu)$	$\frac{3}{2}$	$\frac{1}{2}$	Δ^+
$\frac{1}{\sqrt{3}}(ddu + dud + udd)$	$\frac{3}{2}$	$-\frac{1}{2}$	Δ^0
ddd	$\frac{3}{2}$	$-\frac{3}{2}$	Δ^-
$\frac{1}{\sqrt{2}}(ud - du)u$	$\frac{1}{2}$	$\frac{1}{2}$	N^+
$\frac{1}{\sqrt{2}}(ud - du)d$	$\frac{1}{2}$	$-\frac{1}{2}$	N^0

tice, where the effects of this splitting are smaller than the precision of current calculations, we set $m_u = m_d$ and have an exact SU(2) isospin symmetry. We use quark model flavor wave functions to form operators which have definite isospin and strangeness. The flavor wave functions of baryons with zero strangeness are given in Table 3.2.

For strange baryons, we require that the light quark flavors transform as SU(2) irreps. For a singly strange baryon, the light quarks may either be in an $I = 1$ isospin triplet or $I = 0$ isospin singlet. For doubly strange baryons, the light quark is simply a u or d quark. The triply strange baryons have no light quarks. The flavor wave functions of these baryons is summarized in Table 3.3.

To construct operators corresponding to one of these baryons, we simply take the appropriate linear combination of elemental operators with the flavor indices

Table 3.3: Quark model flavor wave functions for strange light baryons. Isospin I , isospin projection I_3 , and strangeness are also listed.

Flavor	I	I_3	S	Particle
uus	1	1	1	Σ^+
$\frac{1}{\sqrt{2}}(ud + du)s$	1	0	1	Σ^0
dds	1	-1	1	Σ^-
$\frac{1}{\sqrt{2}}(ud - du)s$	0	0	1	Λ^0
uss	$\frac{1}{2}$	$\frac{1}{2}$	2	Ξ^+
dss	$\frac{1}{2}$	$-\frac{1}{2}$	2	Ξ^-
sss	0	0	3	Ω^-

permuted to match the flavor structure of particle as indicated in Tables 3.2 and 3.3. We denote a baryon of flavor F as $B_{\alpha\beta\gamma;ijk}^F(t)$ and write the projection as

$$B_{\alpha\beta\gamma;ijk}^F(t) = \sum_{A,B,C} \phi_{ABC}^F \Phi_{\alpha\beta\gamma;ijk}^{ABC}. \quad (3.22)$$

With the exact isospin symmetry of the Lagrangian, the energy in each isospin/strangeness channel is independent of I_3 and thus we only form correlators for operators with a single value of I_3 . In Table 3.4 we give the baryon operators for maximal value of I_3 in each channel. Operators with lower I_3 are obtained by applying the isospin lowering operator.

Table 3.4: Projections of elemental annihilation operators, Eq. (3.19), onto operators of definite isospin and strangeness. Only the operator of maximal isospin in each channel is given.

Baryon	Operator
Δ^{++}	$B_{\alpha\beta\gamma;ijk}^{\Delta}(t) = \Phi_{\alpha\beta\gamma;ijk}^{uuu}(t)$
N^{+}	$B_{\alpha\beta\gamma;ijk}^N(t) = \Phi_{\alpha\beta\gamma;ijk}^{uud}(t) - \Phi_{\alpha\beta\gamma;ijk}^{duu}(t)$
Σ^{+}	$B_{\alpha\beta\gamma;ijk}^{\Sigma}(t) = \Phi_{\alpha\beta\gamma;ijk}^{uus}(t)$
Λ^0	$B_{\alpha\beta\gamma;ijk}^{\Lambda}(t) = \Phi_{\alpha\beta\gamma;ijk}^{uds}(t) - \Phi_{\alpha\beta\gamma;ijk}^{dus}(t)$
Ξ^0	$B_{\alpha\beta\gamma;ijk}^{\Xi}(t) = \Phi_{\alpha\beta\gamma;ijk}^{ssu}(t)$
Ω^{-}	$B_{\alpha\beta\gamma;ijk}^{\Omega}(t) = \Phi_{\alpha\beta\gamma;ijk}^{sss}(t)$

3.4 Spin and Parity Projections

We construct operators which transform as irreps of the lattice rotation group, the octahedral group. We first review the properties of this group and then discuss how we create operators which transform as irreducible representations of the group. A thorough introduction to group theory can be found in [50]. This discussion follows [45] and [51].

3.4.1 The Octahedral Group

The octahedral group O is the subset of $SO(3)$ rotations which leave a cube invariant. The 24 elements of the group can be divided into six conjugacy classes:

the identity I , the 3 rotations by π about the coordinate axes, the 6 rotations by $\pm\pi/2$ by the coordinate axes, 8 rotations of $\pm 2\pi/3$ about each of the four body-diagonal axes, and 6 rotations by π about the six face-diagonal axes. The octahedral group has 5 irreducible representations: two 1-dimensional irreps, denoted A_1 and A_2 ; one 2-dimensional representation, denoted E ; and two 3-dimensional irreps, denoted T_1 and T_2 .

In the continuum, half-integer spin representations of the continuum rotation group are “double-valued”. A rotation by 2π is not the same as the identity operator, but instead rephases the state with an observable non-vanishing phase. A rotation of 4π is needed to rotate a state exactly onto itself. On the lattice, we capture this property by introducing a new element to the group $\bar{I} \neq I$ which represents a rotation by 2π about any axis. This new group, denoted O^D , has 48 elements, the 24 elements of the group O plus the product of \bar{I} with each of these 24 elements. O^D has 8 irreps: A_1 , A_2 , E , T_1 , T_2 , which correspond to integer spins, and three additional irreps: G_1 , G_2 , and H which correspond to half-integer spins. The G irreps both have dimension 2 while the H irrep has dimension 4.

Finally, we consider the group O_h^D , the double-valued octahedral group with spatial inversion. The addition of spatial inversion once again doubles the number of elements in the group to 96. There are 16 irreps: A_{1g} , A_{2g} , E_g , T_{1g} , T_{2g} , A_{1u} , A_{2u} , E_u , T_{1u} , T_{2u} , G_{1g} , G_{2g} , H_g , G_{1u} , G_{2u} , and H_u . The g subscript stands for “gerade” (German for even) and corresponds to even parity representations, while the u subscript stands for “ungerade” (German for odd) and corresponds to odd parity representations. Once again the A_1 , A_2 , E , T_1 , and T_2 irreps correspond to

integer spins, while G_1 , G_2 , and H correspond to half-integer spin. As baryons are fermions with half-integer spins, we will only be concerned with the six half-integer spin representations of O_h^D .

3.4.2 Projecting onto Group Irreps

We would like project our zero-momentum nucleon and delta operators onto irreps of O_h^D . First, we consider what happens to an operator under one of the group transformations R . Each R has a corresponding operator U_R in the Hilbert space of the physical system. Under R , an arbitrary state $|\psi\rangle$ and operator \mathcal{O} transform as

$$|\psi\rangle \rightarrow U_R|\psi\rangle, \quad (3.23)$$

$$\mathcal{O} \rightarrow U_R \mathcal{O} U_R^\dagger. \quad (3.24)$$

The transformation of an elemental operator has two effects: the transformation of the Dirac spinor and a change in the directions of the displacements. A Dirac spinor, under the rotation R transforms as

$$U_R \psi_{a\alpha}^A U_R^\dagger = S_{\alpha\beta}^{-1}(R) \psi_{a\beta}^A, \quad (3.25)$$

$$U_R \bar{\psi}_{\bar{a}\bar{\alpha}}^{\bar{A}} U_R^\dagger = \bar{\psi}_{\bar{a}\bar{\beta}}^{\bar{A}} S_{\bar{\beta}\bar{\alpha}}(R), \quad (3.26)$$

$$S_{\alpha\beta}(R) = \exp\left(\frac{1}{8}\omega_{\mu\nu}[\gamma_\mu, \gamma_\nu]\right), \quad (3.27)$$

where $\omega_{\mu\nu}$ is an antisymmetric tensor which parameterizes the rotation [28]. We only consider spatial rotations and thus have $\omega_{4\mu} = \omega_{\mu 4} = 0$. We can parametrize a rotation as a vector $\vec{\theta}$ where the direction specifies the axis of the rotation and the magnitude specifies the angle of the rotation. We then have $\omega_{ij} = -\epsilon_{ijk}\theta_k$. For

spatial inversion we have $S = \gamma_4$.

Under a transformation by O_h^D , each of the six possible displacement directions gets permuted. For example, after a rotation of the coordinate system by $\pi/2$ about the z -axis, a vector originally lying in the $+\hat{x}$ direction points in the $-\hat{y}$ direction, a vector originally pointing in the $+\hat{y}$ directions points in the $+\hat{x}$ direction, and a vector originally pointing in the $+\hat{z}$ direction remains pointing in that direction. Thus, under this particular rotation, the displacement directions are permuted as $\pm\hat{x} \rightarrow \mp\hat{y}$, $\pm\hat{y} \rightarrow \pm\hat{x}$, and $\pm\hat{z} \rightarrow \pm\hat{z}$. In general, each rotation R changes the displacement direction of a quark j , to some new direction denoted Rj .

The transformation of a smeared, displaced quark sink is given by

$$U_R \left[\tilde{D}_j^{(p)} \tilde{\psi} \right]_{a\alpha}^A(x) U_R^\dagger = S_{\alpha\beta}^{-1}(R) \left[\tilde{D}_{Rj}^{(p)} \tilde{\psi} \right]_{a\beta}^A(x), \quad (3.28)$$

and the transformation of the corresponding source is given by

$$U_R \left[\tilde{\psi} \tilde{D}_j^{(p)\dagger} \right]_{\bar{a}\bar{\alpha}}^{\bar{A}}(x) U_R^\dagger = \left[\tilde{\psi} \tilde{D}_{Rj}^{(p)\dagger} \right]_{\bar{a}\bar{\beta}}^{\bar{A}}(x) S_{\bar{\beta}\bar{\alpha}}(R). \quad (3.29)$$

We transform a baryon operator by simply transforming each quark operator within it:

$$U_R B_{\alpha\beta\gamma;ijk}^F(t) U_R^\dagger = S_{\alpha\delta}^{-1}(R) S_{\beta\sigma}^{-1}(R) S_{\gamma\lambda}^{-1}(R) B_{\delta\sigma\lambda;Ri,Rj,Rk}^F(t), \quad (3.30)$$

$$U_R \bar{B}_{\bar{\alpha}\bar{\beta}\bar{\gamma};\bar{i}\bar{j}\bar{k}}^F(t) U_R^\dagger = \bar{B}_{\bar{\delta}\bar{\sigma}\bar{\lambda};R\bar{i},R\bar{j},R\bar{k}}^F(t) S_{\bar{\delta}\bar{\alpha}}(R) S_{\bar{\sigma}\bar{\beta}}(R) S_{\bar{\lambda}\bar{\gamma}}(R). \quad (3.31)$$

The first step to building operators which transform as irreps of O_h^D is to form a linearly independent basis of operators for each flavor and displacement pattern from which all possible operators of that type can be constructed. Note that if we were to take all possible combinations of spin and displacement indices, we would

Table 3.5: Restrictions on spin and displacement indices for nucleon operators for each displacement pattern. These restrictions give a complete set of linearly independent operators. The size of each set $M_{N,T}$ is also given.

Operator type	Restrictions	$M_{N,T}$
Single-site	$(i = j = k = 0, \alpha \geq \beta, \alpha > \gamma)$	20
Singly-displaced	$(i = j = 0, k \neq 0)$	384
Doubly-displaced-I	$(i = 0, j = -k, k \neq 0)$	384
Doubly-displaced-L	$(i = 0, j \neq 0, k \neq 0, j \neq k)$	1536
Triply-displaced-T	$(i = -j, j \neq 0, k \neq 0, j \neq k)$	1536

have a linearly dependent set of operators. As an example, for the single-site delta operators, switching the spins on two of the quarks introduces a sign change due to the spin statistics of the quarks, i.e. $B_{\alpha\beta\gamma;000}^\Delta = -B_{\beta\alpha\gamma;000}^\Delta$, and thus these two operators are linearly dependent. A linearly independent set is given by $\{B_{\alpha\beta\gamma;000}^\Delta\}$ with $\alpha \leq \beta \leq \gamma$. The specification of the basis depends on both the displacements of the quarks and the flavor structure. We denote the number of basis vectors for a baryon of flavor F and displacement pattern T as $M_{F,T}$. The bases for the nucleon operators are specified in Table 3.5 and for the delta operators in Table 3.6.

We denote the linearly independent basis for a given sink operator type as $\{B_i^{F,T}\}$, where again F stands for the baryon flavor and T the displacement pattern. i labels individual operators in the basis (essentially collecting all spins and displacements into a single index). Any operator Ψ with the same flavor and dis-

Table 3.6: Restrictions on spin and displacement indices for delta operators for each displacement pattern. These restrictions give a complete set of linearly independent operators. The size of each set $M_{\Delta,T}$ is also given.

Operator type	Restrictions	$M_{\Delta,T}$
Single-site	$(i = j = k = 0, \alpha \leq \beta \leq \gamma)$	20
Singly-displaced	$(i = j = 0), k \neq 0, \alpha \leq \beta)$	240
Doubly-displaced-I	$(i = 0, j = -k, k > 0)$	192
Doubly-displaced-L	$(i = 0, j \neq 0, k \neq 0, j < k)$	768
Triply-displaced-T	$(i = -j, j > 0, j \neq k , k \neq 0)$	768

placement pattern can then be represented as a vector v such that

$$\Psi = \sum_{i=1}^{M_{F,T}} v_i B_i^{F,T}. \quad (3.32)$$

Moreover, under a group operation, we can determine from Eq. (3.28) how each of the basis operators transform, and rewrite the transformed operators in terms of the basis operators:

$$U_R B_i^{F,T} U_R^\dagger = \sum_{j=1}^N B_j^{F,T} W_{ji}(R). \quad (3.33)$$

The matrices $W(R)$ form a representation of O_h^D on the linearly independent basis of operators. We reduce this representation by finding a new basis in which the matrices $W(R)$ are in block-diagonal form, and each block is itself irreducible. The new basis vectors form sets which each transform under group operations as an irrep of O_h^D . In general, when we reduce the representation, irreps of O_h^D will occur, or

be “embedded”, more than once. We label the new basis vectors as $B_a^{F,T,\Lambda,i}$, where Λ labels the irrep, i the row, and a the embedding of the irrep. These basis vectors transform under R as

$$U_R B_a^{F,T,\Lambda,i} U_R^\dagger = \sum_{j=1}^{n_\Lambda} B_a^{F,T,\Lambda,j} D^\Lambda(R)_{ji}, \quad (3.34)$$

where n_Λ is the dimension of irrep Λ and $D^\Lambda(R)$ is the matrix corresponding to R in Λ . The transformation of the source operators is

$$U_R \bar{B}_a^{F,T,\Lambda,i} U_R^\dagger = \sum_{j=1}^{n_\Lambda} \bar{B}_a^{F,T,\Lambda,j} D^{\Lambda*}(R)_{ji}, \quad (3.35)$$

We form these new operators via projection operators onto each row of each irrep. We make use of the following orthogonality relation between matrix elements of unitary irreps μ and ν of any group [50]:

$$\sum_R D_{il}^\Lambda(R) D_{jm}^{\Gamma*}(R) = \frac{g}{n_\Lambda} \delta_{\Lambda\Gamma} \delta_{lm} \delta_{ij}, \quad (3.36)$$

where g is the number of elements of the group. The assumption that irreps are unitary is not a problem as all representations of finite groups such as O_h^D are equivalent to a unitary representation. We define the following transformation P_{ij}^Λ on an operator $B_\ell^{F,T}$:

$$P_{ij}^\Lambda B_\ell^{F,T} = \frac{n_\Lambda}{g} \sum_R D_{ij}^{\Lambda*}(R) U_R B_\ell^{F,T} U_R^\dagger. \quad (3.37)$$

The resulting operator transforms as the i^{th} row of irrep Λ :

$$U_S P_{ij}^\Lambda B_\ell^{F,T} U_S^\dagger = \frac{n_\Lambda}{g} \sum_R D_{ij}^{\Lambda*}(R) U_S U_R B_\ell^{F,T} U_R^\dagger U_S^\dagger, \quad (3.38)$$

$$= \frac{n_\Lambda}{g} \sum_R D_{ij}^{\Lambda*}(S^{-1}SR) U_{SR} B_\ell^{F,T} U_{SR}^\dagger, \quad (3.39)$$

$$= \sum_{k=1}^{n_\Lambda} \left(\frac{n_\Lambda}{g} \sum_R D_{kj}^{\Lambda*}(R) U_R B_\ell^{F,T} U_R^\dagger \right) D_{ki}^\Lambda(S), \quad (3.40)$$

$$= \sum_{k=1}^{n_\Lambda} \left(P_{kj}^\Lambda B_\ell^{F,T} \right) D_{ki}^\Lambda(S), \quad (3.41)$$

where in the third line we have used the fact that the set of $\{SR\}$ for constant S contains every element of the group exactly once and thus when we sum over R we can replace SR with simply R . Note the choice of j in Eq. (3.37) is arbitrary, but the choice $j = i$ has the property $(P_{ii}^\Lambda)^2 = P_{ii}^\Lambda$, and is thus a true projection operator:

$$P_{ii}^\Lambda P_{ii}^\Lambda B_\ell^{F,T} = \frac{n_\Lambda^2}{g^2} \sum_R D_{ii}^{\Lambda*}(R) \sum_S D_{ii}^{\Lambda*}(R^{-1}RS) U_{RS} B_\ell^{F,T} U_{RS}^\dagger, \quad (3.42)$$

$$= \frac{n_\Lambda^2}{g^2} \sum_{k=1}^{n_\Lambda} \sum_R D_{ii}^{\Lambda*}(R) D_{ki}^\Lambda(R) \sum_S D_{ki}^{\Lambda*}(S) U_S B_\ell^{F,T} U_S^\dagger, \quad (3.43)$$

$$= \frac{n_\Lambda}{g} \sum_S D_{ii}^{\Lambda*}(S) U_S B_\ell^{F,T} U_S^\dagger, \quad (3.44)$$

$$= P_{ii}^\Lambda B_\ell^{F,T}, \quad (3.45)$$

where on the third line we have used the orthogonality relation in Eq. (3.36). The set of projected operators, $\{P_{jj}^\Lambda B_\ell^{A,T}\}$, $j = 1 \dots n_\Lambda$ is not guaranteed to satisfy Eq. (3.34) as the different rows may have different normalizations and phases and may also mix the separate embeddings of the irrep differently. To guarantee the correct transformation, we instead construct only the first row of each irrep, fix the

normalization and phase as desired, and construct the other rows via

$$B_a^{F,T,\Lambda,i} = \frac{n_\Lambda}{g} \sum_R D_{i1}^{\Lambda*}(R) U_R B_a^{F,T,\Lambda,1} U_R^\dagger. \quad (3.46)$$

We can derive this relation starting from Eq. (3.34) and projecting $B_a^{F,T,\Lambda,i}$ out of the sum on the right hand side by multiplying by $\frac{n_\Lambda}{g} D_{i1}^{\Lambda*}(R)$, summing over R , and using Eq. (3.36).

After defining the projection operators, the next step is to write down their matrix representations in the linearly independent basis of each operator set. This is accomplished by substituting Eq. (3.33) into Eq. (3.37) to obtain

$$B_a^{F,T,\Lambda,i} = \sum_{b=1}^{M_{F,T}} P_{ab}^{F,T,\Lambda,i} B_b^{F,T}, \quad (3.47)$$

$$P_{ab}^{F,T,\Lambda,i} = \frac{n_\Lambda}{g} \sum_R D_{ii}^{\Lambda*}(R) W_{ba}(R). \quad (3.48)$$

This gives us a total of $M_{F,T}$ operators, although, generally the number of linearly independent operators, r (equal to the rank of the matrix $P^{F,\Lambda,i}$) is much smaller. This number r is the number of embeddings of irrep Λ within the basis. Each row of $P^{F,\Lambda,i}$ gives a single operator which transforms as the i^{th} row of Λ in terms of the initial basis operators. We can obtain r linearly independent operators by performing a Gram-Schmidt orthogonalization on the rows. This requires the projection matrix to be unitary, which is guaranteed only if our initial representation $W(R)$ is unitary. The representation can be made unitary via a similarity transformation, effectively changing the initial basis. We can perform the orthogonalization in this new basis and then undo the similarity transformation to obtain projected operators in terms of the initial basis. Equivalently, we can perform the Gram-Schmidt

orthogonalization with a modified metric given by

$$M = \frac{1}{g} \sum_R W^\dagger(R) W(R) \quad (3.49)$$

This gives a set of projection coefficients $c_{a,b}^{A,T,\Lambda,i}$ ($a = 1 \dots r$, $b = 1 \dots M_b$) which satisfy

$$\sum_{c,d=1}^{M_{F,T}} c_{ac}^{F,T,\Lambda,i*} M_{cd} c_{bd}^{F,T,\Lambda,i} = \delta_{ab}. \quad (3.50)$$

The number of embeddings of each irrep for each operator type is given in Table 3.7 for the nucleons and Table 3.8 for the deltas.

As discussed above, this procedure is done to obtain only the row 1 operators. From Eqs. (3.33) and (3.46), the projection coefficients for the other rows are given in terms of the row 1 projection coefficients by

$$c_{ab}^{F,T,\Lambda,i} = \sum_{c=1}^{M_{F,T}} c_{ac}^{F,T,\Lambda,1} \frac{n_\Lambda}{g} \sum_R D_{i1}^{\Lambda*}(R) W_{bc}(R). \quad (3.51)$$

In terms of the linearly independent basis, the projected sink and source operators are

$$B_a^{F,T,\Lambda,i} = \sum_{b=1}^{M_{F,T}} c_b^{F,T,\Lambda,i} B_b^{F,T}, \quad (3.52)$$

$$\bar{B}_a^{F,T,\Lambda,i} = \sum_{b=1}^{M_{F,T}} c_b^{F,T,\Lambda,i*} \bar{B}_b^{F,T}. \quad (3.53)$$

The correlation functions of operators which transform as irreps of the lattice group have several important properties. We consider a correlator between two

Table 3.7: The number of embeddings of irreps of O^D for nucleon operators of each displacement type. The parity label is omitted as the numbers are independent of parity.

Operator type	G_1	G_2	H
Single-site	3	0	1
Singly-displaced	24	8	32
Doubly-displaced-I	24	8	32
Doubly-displaced-L	64	64	128
Triply-displaced-T	64	64	128
Total	179	144	321

baryon operators:

$$\langle \Omega | B_a^{F,S,\Lambda,i}(t) \bar{B}_b^{F,T,\Gamma,j}(0) | \Omega \rangle = \langle \Omega | U_R B_a^{F,S,\Lambda,i}(t) U_R^\dagger U_R \bar{B}_b^{F,T,\Gamma,j}(0) U_R^\dagger | \Omega \rangle, \quad (3.54)$$

$$= \frac{1}{g} \sum_R \langle \Omega | U_R B_a^{F,S,\Lambda,i}(t) U_R^\dagger U_R \bar{B}_b^{F,T,\Gamma,j}(0) U_R^\dagger | \Omega \rangle, \quad (3.55)$$

$$= \frac{1}{g} \sum_R \sum_{k=1}^{n_\Lambda} \sum_{\ell=1}^{n_\Gamma} (D_{ki}^{\Lambda*}(R) D_{\ell j}^\Gamma(R)) \langle \Omega | B_a^{F,S,\Lambda,k}(t) \bar{B}_b^{F,T,\Gamma,\ell}(0) | \Omega \rangle, \quad (3.56)$$

$$= \delta_{\Lambda\Gamma} \delta_{ij} \frac{1}{n_\Lambda} \sum_{k=1}^{n_\Lambda} \langle \Omega | B_a^{F,S,\Lambda,k}(t) \bar{B}_b^{A,T\Lambda,k}(0) | \Omega \rangle, \quad (3.57)$$

where on the last line, we have once again used Eq. (3.36). Correlation functions between operators of different irreps vanish. This is to be expected as the group transformations commute with the Hamiltonian. We also see that operators must

Table 3.8: The number of embeddings of irreps of O^D for delta operators of each displacement type. The parity label is omitted as the numbers are independent of parity

Operator type	G_1	G_2	H
Single-site	1	0	2
Singly-displaced	14	6	20
Doubly-displaced-I	12	4	16
Doubly-displaced-L	32	32	64
Triply-displaced-T	32	32	64
Total	91	74	166

transform as the same row of the irrep to obtain a non-vanishing correlation function. Furthermore, the correlation functions are independent of row. We can improve our statistics by averaging the correlation functions over rows. From the flavor symmetries of the Lagrangian we also know that the correlation functions between two different baryon flavors vanish. We therefore form correlation matrices from operators with the same flavor, irrep and row, but varying displacement pattern and embedding. We average these matrices over rows and use the variational method to extract zero-momentum energy eigenstates which are labeled by flavor and lattice irrep. Since the irreps have definite parity we can readily identify the parity of the extracted states. The identification of the continuum spin is discussed below.

3.4.3 Continuum Spin Identification

The identification of the continuum spin of lattice states is accomplished by subducing the continuum rotation group, $O(3)$ to the lattice rotation group [52]. The lattice rotation group is a subgroup of the continuum group. Given a representation of $SO(3)$,² those matrices which correspond to elements of O^D form the “subduced” representation of O^D . Even if we start with an irreducible representation of $SO(3)$, the subduced representation is, in general, reducible. This must be the case for continuum states with spin- $\frac{5}{2}$ or greater, which belong to continuum irreps of dimension 6 or higher. The subduced representation has this same dimension and must be reducible since the lattice irreps have a maximal dimension of 4.

By reducing the subduced representation to lattice irreps, we determine how the lattice states corresponding to continuum spins states should be distributed across the lattice irreps. As an example, the subduction of continuum spin- $\frac{5}{2}$ states to O^D reduces to $G_2 \oplus H$. Continuum spin- $\frac{5}{2}$ states occur on the lattice within both the G_2 and H spectra. Sufficiently close to the continuum limit, these states will appear to be degenerate. A degeneracy between the G_2 and H irreps is therefore evidence for a spin $\frac{5}{2}$ state. Table 3.9, adapted from [53], gives the reduction of the subduced representations to irreps of O^D . In general, we look for patterns of degeneracies between irreps which match the occurrences of the irreps in the subduction of continuum $SO(3)$ irreps to O^D .

²We consider the subduction $SO(3)$ to O^D , ignoring spatial inversion. The subduction of $O(3)$ to O_h^D is identical, except continuum irreps have parity labels which match the parity of the subduced representations.

Table 3.9: The number of occurrences of each irrep of O^D in the subduction of $SO(3)$. We can identify continuum spins of lattice states by identifying patterns of degeneracies across irreps which match the occurrences of lattice in irreps in the subduced representations.

J	G_1	G_2	H
$\frac{1}{2}$	1	0	0
$\frac{3}{2}$	0	0	1
$\frac{5}{2}$	0	1	1
$\frac{7}{2}$	1	1	1
$\frac{9}{2}$	1	0	2
$\frac{11}{2}$	1	1	2
$\frac{13}{2}$	1	2	2
$\frac{15}{2}$	1	1	3
$\frac{17}{2}$	2	1	3
$\frac{19}{2}$	2	2	3
$\frac{21}{2}$	1	2	4
$\frac{23}{2}$	2	2	4

Chapter 4

The Excited Nucleon Spectrum

In this chapter we describe the extraction of the excited nucleon spectrum using lattices with two flavors of dynamical quarks [54]. We first describe in Section 4.1 how to calculate nucleon correlation functions on a computer. These correlation functions are best calculated on anisotropic lattices, which are described in Section 4.2. In Sections 4.3 - 4.9 we present the details of the calculation. Finally, the results are given in Section 4.10.

4.1 Nucleon Correlation Functions

We begin by discussing how to calculate correlation functions between the nucleon operators described in the previous chapter. We first make several simplifications to the notation. We absorb the factors of γ_4 in the creation operators into the projection coefficients, defining

$$\bar{c}_{I;\bar{\alpha}\bar{\beta}\bar{\gamma};\bar{i}\bar{j}\bar{k}}^{F,\Lambda} = c_{I;\bar{\delta}\bar{\sigma}\bar{\lambda};\bar{i}\bar{j}\bar{k}}^{F,\Lambda*} \gamma_{\bar{\delta}\bar{\alpha}}^4 \gamma_{\bar{\sigma}\bar{\beta}}^4 \gamma_{\bar{\lambda}\bar{\gamma}}^4. \quad (4.1)$$

and redefine the elemental creation operators without the factors of γ_4 in Eq. (3.18). We relabel the sink operators $B_I^{F,\Lambda}$, where F labels the flavor, Λ the irrep, and I collects the displacement type, embedding, and row into one index. Finally, for brevity the displacement indices will be implicit.

The operators now satisfy

$$B_I^{F,\Lambda}(t) = \sum_{\alpha,\beta,\gamma} \sum_{A,B,C} c_{I;\alpha\beta\gamma}^{F,\Lambda} \phi_{ABC}^F \Phi_{\alpha\beta\gamma}^{ABC}, \quad (4.2)$$

$$\bar{B}_I^{F,\Lambda}(t) = \sum_{\bar{\alpha},\bar{\beta},\bar{\gamma}} \sum_{\bar{A}\bar{B}\bar{C}} \bar{c}_{I;\bar{\alpha}\bar{\beta}\bar{\gamma}}^{F,\Lambda} \phi_{\bar{A}\bar{B}\bar{C}}^F \bar{\Phi}_{\bar{\alpha}\bar{\beta}\bar{\gamma}}^{\bar{A}\bar{B}\bar{C}}. \quad (4.3)$$

The correlation function between two baryon operators is

$$C_{IJ}^{F,\Lambda}(t) = c_{I;\alpha\beta\gamma}^{F,\Lambda} \bar{c}_{J;\bar{\alpha}\bar{\beta}\bar{\gamma}}^{F,\Lambda} \phi_{ABC}^F \phi_{\bar{A}\bar{B}\bar{C}}^F \langle \Omega | \Phi_{\alpha\beta\gamma}^{ABC}(t_f) \bar{\Phi}_{\bar{\alpha}\bar{\beta}\bar{\gamma}}^{\bar{A}\bar{B}\bar{C}}(t_i) | \Omega \rangle. \quad (4.4)$$

This reduces the baryon correlation function to correlation functions of elemental operators. In terms of the quark fields, these correlators are

$$\begin{aligned} \langle \Omega | \Phi_{\alpha\beta\gamma}^{ABC}(t_f) \bar{\Phi}_{\bar{\alpha}\bar{\beta}\bar{\gamma}}^{\bar{A}\bar{B}\bar{C}}(t_i) | \Omega \rangle = \\ \frac{1}{L^6} \sum_{\vec{x}_f, \vec{x}_i} \langle \Omega | \epsilon_{abc} \left[\tilde{D}_i^{(p)} \tilde{\psi} \right]_{a\alpha}^A(\vec{x}_f, t_f) \left[\tilde{D}_j^{(p)} \tilde{\psi} \right]_{b\beta}^B(\vec{x}_f, t_f) \left[\tilde{D}_k^{(p)} \tilde{\psi} \right]_{c\gamma}^C(\vec{x}_f, t_f) \\ \times \epsilon_{\bar{a}\bar{b}\bar{c}} \left[\tilde{\bar{\psi}} \tilde{D}_i^{(p)\dagger} \right]_{\bar{a}\bar{\alpha}}^{\bar{A}}(\vec{x}_i, t_i) \left[\tilde{\bar{\psi}} \tilde{D}_j^{(p)\dagger} \right]_{\bar{b}\bar{\beta}}^{\bar{B}}(\vec{x}_i, t_i) \left[\tilde{\bar{\psi}} \tilde{D}_k^{(p)\dagger} \right]_{\bar{c}\bar{\gamma}}^{\bar{C}}(\vec{x}_i, t_i) | \Omega \rangle. \end{aligned} \quad (4.5)$$

Using Wick's theorem we rewrite the elemental correlation function in terms of single-quark propagators between like-flavored quarks. We define a product of three single-quark propagators as follows:

$$\tilde{G}_{\alpha\beta\gamma;\bar{\alpha}\bar{\beta}\bar{\gamma}}^{ABC}(t) = \frac{1}{L^6} \sum_{\vec{x}_f, \vec{x}_i} \epsilon_{abc} \epsilon_{\bar{a}\bar{b}\bar{c}} \tilde{S}_{a\alpha;\bar{a}\bar{\alpha}}^A(\vec{x}_f, t_f; \vec{x}_i, t_i) \tilde{S}_{b\beta;\bar{b}\bar{\beta}}^B(\vec{x}_f, t_f; \vec{x}_i, t_i) \tilde{S}_{c\gamma;\bar{c}\bar{\gamma}}^C(\vec{x}_f, t_f; \vec{x}_i, t_i), \quad (4.6)$$

where the single quark propagators are

$$\tilde{S}_{a\alpha;\bar{a}\bar{\alpha}}^A(\vec{x}_f, t_f; \vec{x}_i, t_i) = \langle \Omega | \left[\tilde{D}_i^{(p)} \tilde{\psi} \right]_{a\alpha}^A(\vec{x}_f, t_f) \left[\tilde{\bar{\psi}} \tilde{D}_i^{(p)\dagger} \right]_{\bar{a}\bar{\alpha}}^A(\vec{x}_i, t_i) | \Omega \rangle. \quad (4.7)$$

In this work, we use the nucleon operators with the maximal value of I_3 , which have two up-flavored quarks and one down-flavored quark. The correlator between two

elemental operators with this flavor structure has two possible Wick contractions.

Expanding the nucleon correlation function and performing the Wick contractions,

$$C_{IJ}^{N,\Lambda}(t) = c_{I;\alpha\beta\gamma}^{N,\Lambda} \bar{c}_{J;\bar{\alpha}\bar{\beta}\bar{\gamma}}^{N,\Lambda} [\tilde{G}_{\alpha\beta\gamma;\bar{\alpha}\bar{\beta}\bar{\gamma}}^{rud}(t) + \tilde{G}_{\alpha\beta\gamma;\bar{\beta}\bar{\alpha}\bar{\gamma}}^{rud}(t) - \tilde{G}_{\alpha\beta\gamma;\bar{\gamma}\bar{\beta}\bar{\alpha}}^{rud}(t) - \tilde{G}_{\alpha\beta\gamma;\bar{\beta}\bar{\gamma}\bar{\alpha}}^{rud}(t) \\ - \tilde{G}_{\beta\gamma\alpha;\bar{\beta}\bar{\alpha}\bar{\gamma}}^{rud}(t) - \tilde{G}_{\beta\gamma\alpha;\bar{\alpha}\bar{\beta}\bar{\gamma}}^{rud}(t) + \tilde{G}_{\gamma\beta\alpha;\bar{\gamma}\bar{\beta}\bar{\alpha}}^{rud}(t) + \tilde{G}_{\gamma\beta\alpha;\bar{\beta}\bar{\gamma}\bar{\alpha}}^{rud}(t)]. \quad (4.8)$$

This reduces the nucleon correlation function to single quark propagators between smeared and displaced fields. We first consider the propagator from a point source to a point sink. As discussed in Section 2.7, this is given by

$$\langle \Omega | \psi_{a\alpha}^A(y) \bar{\psi}_{\bar{a}\bar{\alpha}}^A(x) | \Omega \rangle = \frac{1}{N} \sum_U (K^{-1})_{a\alpha;\bar{a}\bar{\alpha}}^A(y, x, U). \quad (4.9)$$

For fixed x , \bar{a} , and $\bar{\alpha}$, we solve, in each configuration, the equation

$$K_{\bar{b}\bar{\beta};a\alpha}^A(z, y) \eta_{a\alpha}(y) = \delta_{z,x} \delta_{\bar{\beta}\bar{\alpha}} \delta_{\bar{b}\bar{a}}, \quad (4.10)$$

to obtain

$$\eta_{a\alpha}(y) = (K^{-1})_{a\alpha;\bar{a}\bar{\alpha}}^A(y, x). \quad (4.11)$$

This is called the “point-to-all” propagator as it is the propagator from a single fixed source point to a sink at any point on the lattice (in a single gauge configuration).

Using the matrix representations of the smearing and displacement operators, Eqs. (3.6) and (3.15), the point-to-all propagator for smeared, displaced quarks is (in a single configuration)¹

$$\tilde{S}_{a\alpha;\bar{a}\bar{\alpha}}^A(\vec{x}_f, t_f; \vec{x}_i, t_i) = F_{ab}(\vec{x}_f, \vec{z}, t_f) (K^{-1})_{b\alpha;\bar{b}\bar{\alpha}}^A(\vec{z}, t_f; \vec{w}, t_i) F_{\bar{b}\bar{a}}^*(\vec{w}, \vec{x}_i, t_i), \quad (4.12)$$

¹For the rest of this section, there will be no implied summation over repeated temporal variables.

where F is the product of the displacement and smearing matrices:

$$F_{ab}(\vec{y}, \vec{z}, t) = (\tilde{D}_i^{(p)})_{ac}(\vec{y}, \vec{x}, t) (J(\vec{x}, \vec{z}, t)^{n_\sigma})_{cb}. \quad (4.13)$$

To obtain the propagator we first invert the quark matrix on a displaced, smeared point source,

$$\sum_t K_{b\bar{\alpha};b\alpha}^A(\vec{v}, t_f; \vec{z}, t) \eta_{b\alpha}(\vec{z}, t) = \delta_{\vec{v}, \vec{w}} \delta_{\bar{\alpha}\alpha} \delta_{\bar{b}c} F_{c\bar{a}}^*(\vec{w}, \vec{x}, t_i), \quad (4.14)$$

to get

$$\eta_{b\alpha}(\vec{z}, t_f) = (K^{-1})_{b\alpha; \bar{b}\bar{\alpha}}^A(\vec{z}, t_f; \vec{w}, t_i) F_{\bar{b}\bar{a}}^*(\vec{w}, \vec{x}, t_i). \quad (4.15)$$

We then smear and displace the solution vector η^A to obtain

$$F_{ab}(\vec{y}, \vec{z}, t_f) \eta_{b\alpha}(\vec{z}, t_f) = F_{ab}(\vec{y}, \vec{z}, t_f) (K^{-1})_{b\alpha; \bar{b}\bar{\alpha}}^A(\vec{z}, t_f; \vec{w}, t_i) F_{\bar{b}\bar{a}}^*(\vec{w}, \vec{x}, t_i), \quad (4.16)$$

$$= \tilde{S}_{a\alpha; \bar{a}\bar{\alpha}}^A(\vec{y}, t_f; \vec{x}, t_i). \quad (4.17)$$

4.1.1 Minimizing Matrix Inversions

Each inversion of the quark matrix on a source vector is computationally expensive and we would like to minimize the number of times this step is performed. With each quark-matrix inversion, we obtain the propagators from a source with a single displacement acting at a single point in space-time to sinks with all possible displacements acting at all possible points in space-time. Changing the source displacement or location, however, requires an additional matrix inversion. We construct nucleon correlation functions by calculating a set of single-quark propagators which are combined into correlators using Eqs. (4.6) and (4.8). We build this set of single-quark propagators in such a way that the number of different sources is kept

at a minimum, while still allowing us to construct all possible nucleon correlation functions.

We can use the rotational symmetry of the lattice to reduce the number of sources. For each operator type, we select a canonical orientation. For example, for the singly-displaced operators we always choose the displacement to be in the $+\hat{z}$ direction. Of all possible baryon propagators involving a singly-displaced source, we calculate only those which have the source operator oriented in the $+\hat{z}$ direction. We can then perform rotations on these propagators to obtain those which have a source displacement in one of the other directions. Table 4.1 gives the quark displacements for the canonical orientations of each operator type. Baryon propagators involving sources with these canonical displacements involve source quark operators with only four different displacements: $0, \pm\hat{z}$, and $+\hat{y}$. We need to generate single-quark propagators involving sources with only these four displacements.

We use momentum conservation to further reduce the number of sources needed. Baryon states with different momentum are orthogonal to each other and the correlation function between operators with different momenta vanishes. As a result, we do not need to perform the zero-momentum projection on both the source and the sink. Since the zero-momentum projection at the source requires point-to-all baryon propagators for sources at every spatial point on a given time slice, we instead only do the zero-momentum projection at the sink and calculate the point-to-all baryon propagator only for a single spatial source point. Furthermore, we restrict the source operator to act only on a single timeslice.

The single quark propagators were calculated with the bi-conjugate gradient

Table 4.1: Canonical orientations for each displacement pattern in baryon operators. To minimize the number of quark matrix inversions, we calculate only those baryon propagators with the source operator having the canonical orientation. Propagators with a source oriented differently can be calculated through a rotation.

Displacement Type	Quark displacements
Singly-Displaced	$+\hat{z}$
Doubly-Displaced-I	$+\hat{z}, -\hat{z}$
Doubly-Displaced-L	$+\hat{y}, +\hat{z}$
Triply-Displaced-T	$+\hat{z}, +\hat{y}, -\hat{z}$

algorithm [55] using the Chroma software library [56]. Propagators are calculated for smeared sources at the origin with each of the four possible displacements discussed above and for all 12 possible spin-color indices. The propagators are smeared and displaced at the sinks (using all seven possible displacements). From this set of propagators, we can then construct all possible baryon correlation functions.

4.1.2 Charge Conjugation

In calculating the time dependence of correlation functions, Eq. (2.53), we made the simplification that the lattice had an infinite temporal extent. With a finite extent, there are contributions from states which propagate backward in time. Each quark source operator not only creates a state, but annihilates an antiquark state. With a finite lattice with periodic boundary conditions, these states propagate

backwards in time from the far temporal end of the lattice. We use the charge conjugation operator to understand the properties of these states.

We define the charge conjugation operator in the Hilbert space such that

$$U_C \psi_\alpha U_C^\dagger = \bar{\psi}_\beta C_{\beta\alpha} \quad (4.18)$$

$$U_C \bar{\psi}_{\bar{\alpha}} U_C^\dagger = \psi_{\bar{\beta}} \bar{C}_{\bar{\beta}\bar{\alpha}}. \quad (4.19)$$

Requiring the action to be invariant under charge conjugation leads to the common choice for C and \bar{C} in the Dirac-Pauli basis

$$C = \bar{C} = \gamma_4 \gamma_2. \quad (4.20)$$

Applying the charge conjugation operator to a meson state yields an antimeson state with the same parity and mass. As a result, when we consider a meson correlation function, the forward and backward propagating states are identical and the correlation function has the property $C(t) = C(L_t - t)$. Of course, this equality does not exactly hold in practice due to statistical errors. We can reduce this error by “folding” the correlator or averaging

$$C(t) \rightarrow \frac{1}{2} (C(t) + C(L - t)). \quad (4.21)$$

The situation for baryons is slightly different. Applying the charge conjugation operator to a baryon yields a state of opposite parity, and thus, a different energy. The forward and backward propagating parts of baryon correlation functions corre-

spond to states of opposite parity. We derive

$$C_{IJ}^\Lambda(t) = \langle \Omega | B_I^\Lambda(t) \bar{B}_J^\Lambda(0) | \Omega \rangle, \quad (4.22)$$

$$= c_{I;\alpha\beta\gamma}^\Lambda \bar{c}_{J;\bar{\alpha}\bar{\beta}\bar{\gamma}}^\Lambda \langle \Omega | U_C^\dagger U_C B_{\alpha\beta\gamma}(t) U_C^\dagger U_C \bar{B}_{\bar{\alpha}\bar{\beta}\bar{\gamma}}(0) U_C^\dagger U_C | \Omega \rangle, \quad (4.23)$$

$$= \bar{c}_{I;\alpha\beta\gamma}^{*\Lambda} c_{J;\bar{\alpha}\bar{\beta}\bar{\gamma}}^{*\Lambda} \langle \Omega | \bar{B}_{\delta\sigma\lambda}(t) B_{\bar{\delta}\bar{\sigma}\bar{\lambda}}(0) | \Omega \rangle \gamma_{\delta\alpha}^2 \gamma_{\sigma\beta}^2 \gamma_{\lambda\gamma}^2 \gamma_{\bar{\delta}\bar{\alpha}}^2 \gamma_{\bar{\sigma}\bar{\beta}}^2 \gamma_{\bar{\lambda}\bar{\gamma}}^2, \quad (4.24)$$

$$= \bar{c}_{I;\alpha\beta\gamma}^{*\Lambda} c_{J;\bar{\alpha}\bar{\beta}\bar{\gamma}}^{*\Lambda} \langle \Omega | \bar{B}_{\delta\sigma\lambda}(0) B_{\bar{\delta}\bar{\sigma}\bar{\lambda}}(-t) | \Omega \rangle \gamma_{\delta\alpha}^2 \gamma_{\sigma\beta}^2 \gamma_{\lambda\gamma}^2 \gamma_{\bar{\delta}\bar{\alpha}}^2 \gamma_{\bar{\sigma}\bar{\beta}}^2 \gamma_{\bar{\lambda}\bar{\gamma}}^2, \quad (4.25)$$

$$= -\langle \Omega | B_J^{-\Lambda}(-t) \bar{B}_I^{-\Lambda}(0) | \Omega \rangle, \quad (4.26)$$

$$= C_{JI}^{-\Lambda}(L_t - t), \quad (4.27)$$

where on the fourth line we have used the invariance of the correlation function with time translation and on the sixth line we have assumed antiperiodic temporal boundary conditions. We have defined

$$B_I^{-\Lambda}(t) = c_{I;\alpha\beta\gamma}^{*\Lambda} \bar{B}_{\delta\sigma\lambda}(t) \gamma_{\delta\alpha}^2 \gamma_{\sigma\beta}^2 \gamma_{\lambda\gamma}^2, \quad (4.28)$$

$$\bar{B}_I^{-\Lambda}(t) = \bar{c}_{I;\bar{\alpha}\bar{\beta}\bar{\gamma}}^{*\Lambda} B_{\bar{\delta}\bar{\sigma}\bar{\lambda}}(t) \gamma_{\bar{\delta}\bar{\alpha}}^2 \gamma_{\bar{\sigma}\bar{\beta}}^2 \gamma_{\bar{\lambda}\bar{\gamma}}^2. \quad (4.29)$$

$-\Lambda$ is the opposite parity partner of irrep Λ . We modify the our operator production such that only the positive parity operators are generated using the procedure in the previous chapter and we obtain the corresponding negative parity operators using Eqs. (4.28) and (4.29). This guarantees that Eq. (4.27) holds. We can then fold baryon correlation functions as follows:

$$C_{IJ}^\Lambda(t) \rightarrow \frac{1}{2} [C_{IJ}^\Lambda(t) + C_{JI}^{-\Lambda}(L - t)]. \quad (4.30)$$

We further reduce the statistical uncertainty by exploiting the Hermiticity of the correlation matrix and averaging the matrix with its Hermitian conjugate.

4.2 Anisotropic Lattices

We extract the energies of excited states via the time dependence of correlation matrices. Each measurement of a correlation function consists of the calculation of a matrix element of the form

$$C(t) \sim \langle \Omega | \psi(t_f) \psi(t_f) \psi(t_f) \bar{\psi}(t_i) \bar{\psi}(t_i) \bar{\psi}(t_i) | \Omega \rangle. \quad (4.31)$$

We have not specified any indices on the quark fields or included the projection coefficients. The main point is that we calculate the time-ordered vacuum expectation value of an operator consisting of three single-quark annihilation operators and three single-quark creation operators. The calculation has a statistical uncertainty stemming from the use of stochastic methods to estimate the QCD path integral. This statistical uncertainty is given by Eq. (2.95),

$$\Delta_C(t) = \frac{\sigma_C(t)}{\sqrt{N}}, \quad (4.32)$$

$$\sigma_C^2(t) = \frac{1}{N-1} \sum_{i=1}^N (\bar{C}(t) - C_i(t))^2, \quad (4.33)$$

$$\approx \frac{1}{N} \sum_{i=1}^N (C_i(t))^2 - (\bar{C}(t))^2, \quad (4.34)$$

where N_U is the number of configurations, $\bar{C}(t)$ is the ensemble averaged correlation function, and $C_i(t)$ is the correlation function in configuration i . Combining Eqs. (4.31) and (4.34) gives

$$\begin{aligned} \sigma_C^2(t) \approx & \langle \Omega | \psi(t_f) \psi(t_f) \psi(t_f) \bar{\psi}(t_f) \bar{\psi}(t_f) \bar{\psi}(t_f) \bar{\psi}(t_i) \bar{\psi}(t_i) \bar{\psi}(t_i) \psi(t_i) \psi(t_i) \psi(t_i) | \Omega \rangle \\ & - (\bar{C}(t))^2. \end{aligned} \quad (4.35)$$

The first term is the correlation function between states consisting of three quarks and three anti-quarks. As $t \rightarrow \infty$, this is dominated by a three pion state. We thus expect the statistical uncertainty in a baryon correlator to be

$$\Delta_C \sim \frac{e^{-\frac{3}{2}m_\pi t}}{\sqrt{N}}. \quad (4.36)$$

The signal-to-noise ratio in the correlator for a baryon of flavor F therefore is [57]

$$\frac{\bar{C}(t)}{\Delta_C(t)} \sim \sqrt{N} e^{-(m_F - \frac{3}{2}m_\pi)t}, \quad (4.37)$$

where m_F is the lowest energy state with flavor F .

Since the signal-to-noise ratio decays with time, we only have a limited time window in which to extract an energy spectrum. We would like to maximize the number of lattice points within this window by using a small lattice spacing in the temporal direction. To avoid making the lattice unnecessarily large in the spatial directions, we employ an anisotropic lattice with a finer spacing in the temporal direction as compared to the spatial directions.

The spatial lattice spacing is denoted by a_s , the temporal spacing by a_t , and the corresponding lattice extents by L_s and L_t . We parameterize the action in terms of a_t and ξ_0 , the bare anisotropy. ξ_0 is tuned such that the renormalized anisotropy $\xi = a_t/a_s$ takes on the desired value. For the nucleon spectrum analysis, we used the anisotropic Wilson gauge action [58]. We obtain this action from the isotropic Wilson action, Eq (2.38), by separating the sum over plaquettes into spatial and temporal pieces and explicitly adding necessary factors of ξ_0 to produce the correct

continuum limit:

$$S_G^\xi = \sum_x \beta \left\{ 1 - \frac{1}{2N_c} \left(\sum_{j < k} \frac{1}{\xi_0} \text{Tr}[U_{jk}(x) + U_{jk}^\dagger(x)] + \sum_j \xi_0 \text{Tr}[U_{j4}(x) + U_{j4}^\dagger(x)] \right) \right\}, \quad (4.38)$$

In the fermion sector, we used the Wilson anisotropic action [59]. We rescale the fields and quark masses as in Eqs. (2.10) and (2.11), but use factors of a_s in the field rescaling and a_t for the quark mass. We also include a factor of the bare speed of light ν which will be tuned so that the renormalized quantity equals 1. Once again, we derive the action by taking the isotropic Wilson action, splitting it up into spatial and temporal pieces, and adding necessary factors of ν and ξ_0 . This gives

$$S_F^\xi = \sum_A \sum_x \bar{\psi}_{\bar{a}\bar{\alpha}}^A(x) K_{\bar{a}\bar{\alpha};a\alpha}^A(x, y) \psi_{a\alpha}^A(y), \quad (4.39)$$

$$\begin{aligned} K_{\bar{a}\bar{\alpha};a\alpha}^A(x, y) = & (M^A + \frac{3\nu}{\xi_0} + 1) \delta_{x,y} \delta_{\bar{\alpha},\alpha} \delta_{\bar{a},a} \\ & - \frac{\nu}{2\xi_0} \sum_j \left[(1 - \gamma_j)_{\bar{\alpha},\alpha} U_j(x)_{\bar{a}a} \delta_{y,x+\hat{j}} + (1 + \gamma_j)_{\bar{\alpha}\alpha} U_j^\dagger(x)_{\bar{a},a} \delta_{y,x-\hat{j}} \right] \\ & - \frac{1}{2} \left[(1 - \gamma_4)_{\bar{\alpha},\alpha} U_j(x)_{\bar{a}a} \delta_{y,x+\hat{4}} + (1 + \gamma_4)_{\bar{\alpha}\alpha} U_j^\dagger(x)_{\bar{a},a} \delta_{y,x-\hat{4}} \right]. \end{aligned} \quad (4.40)$$

4.2.1 Tuning the Action

The bare parameters in the action must be tuned to produce the desired renormalized quantities. The anisotropy is determined through Klassen's "Wilson-loop ratio" [58]. We look at the sideways static quark potential $V_s(r)$, in which the static quarks propagate in a spatial direction. We compare the potential for spatial separations $r = ya_s$ and temporal separations $r = ta_t$. If the separations in physical

units are the same, then the potentials are equal,

$$V_s(ya_s) = V_s(ta_t) \quad \text{if } t = \xi y. \quad (4.41)$$

We measure the static quark potential through the ratio of Wilson loops:

$$R_{ss}(x, y) = \frac{W_{ss}(x, y)}{W_{ss}(x+1, y)} \underset{x \rightarrow \infty}{=} e^{-V_s(ya_s)}, \quad (4.42)$$

$$R_{st}(x, t) = \frac{W_{st}(x, t)}{W_{st}(x+1, t)} \underset{x \rightarrow \infty}{=} e^{-V_s(ta_t)}, \quad (4.43)$$

where $W_{ss}(x, y)$ is a spatial Wilson loop and W_{st} is a temporal Wilson loop. If ξ_0 is chosen such that $y = \xi t$ then $R_{ss}(x, y) = R_{st}(x, t)$. In practice, we choose the desired ξ and tune ξ_0 to minimize [60]

$$L(\xi_0) = \sum_{x, y} \frac{(R_{ss}(x, y) - R_{st}(x, \xi y))^2}{(\Delta R_s(x, y))^2 + (\Delta R_t(x, y))^2}, \quad (4.44)$$

where $\Delta R_s(x, y)$ and $\Delta R_t(x, y)$ are the statistical errors in R_{ss} and R_{st} .

The bare speed of light is tuned using the dispersion relation

$$E^2 = \frac{\vec{p}^2}{\xi^2} + m^2. \quad (4.45)$$

We first measure the energy of a meson both at rest and with several different non-zero momenta. We tune the bare speed of light to a value such that the dispersion relation holds.

4.3 Setting the Scale

All energies measured on the lattice are in dimensionless lattice units, $E_{lat} = E_{phys}a_t$, where E_{lat} is the energy as measured on the lattice, and E_{phys} is the energy

in physical units. As the lattice spacing itself is not a parameter that appears in the action, it is unknown a priori. It is therefore necessary to use one lattice measurement to determine the lattice spacing. In this work, we use the Sommer parameter [61], the separation r_0 such that

$$\left. -r^2 \frac{\partial V(r)}{\partial r} \right|_{r=r_0} = 1.65, \quad (4.46)$$

where the $V(r)$ is the static quark potential modeled as

$$V(r) = C + \frac{\alpha}{r} + \sigma r. \quad (4.47)$$

The value 1.65 is chosen as this corresponds to a separation between the quarks of about 0.5 fm, where the static quark potential best describes phenomenological results in charmonium and bottomonium. From [62, 63], $r_0 = 0.462(11)(4)$ fm. The static quark potential is determined by measuring Wilson loops on the lattice for all available r . These measurements can then be fit to extract the constants C , α , and σ in Eq. (4.47). We use Eq. (4.46) to solve for r_0/a_s and determine the spatial lattice spacing. We determine the temporal lattice spacing from $\xi = a_s/a_t$.

4.4 Gauge Configurations

For the nucleon study, we used $24^3 \times 64$ lattices with two flavors of degenerate light dynamical quarks. Setting $\beta = 5.5$ and tuning the bare anisotropy to $\xi_0 = 2.38$ gave a renormalized anisotropy equal to 3. We used two different values for the bare light quark mass, $m_\ell = -0.4086$ and $m_\ell = -0.4125$. To determine the masses of light meson ground states, we calculated correlation functions between operators of

the form $\bar{\psi}_{a\bar{\alpha}}^{\bar{A}}\Gamma_{\bar{\alpha}\alpha}\psi_{a\alpha}^A$ and $\bar{\psi}_{a\bar{\alpha}}^{\bar{A}}(\Gamma\gamma_4)_{\bar{\alpha}\alpha}\psi_{a\alpha}^A$, where the quark flavors and Γ are chosen to produce an operator with the correct quantum numbers. Choosing the quarks to be the light flavors and $\Gamma = \gamma_5$ gives a pion operator, while $\Gamma = \gamma_i$ gives a ρ operator. We used both smeared and unsmeared operators, but no diagonalization was performed on the correlator matrix.

We fit the correlation functions to

$$C(t) = A(e^{-mt} + e^{-m(L_t-t)}). \quad (4.48)$$

The second term captures the backwards-in-time propagating state. In Fig. 4.1 we plot the effective energy of several pion correlators for the $m_\ell = -0.4125$ lattices. We determined the pion mass from a weighted average of masses extracted from fits of the correlators to Eq. (4.48). We obtained pion masses of 416 MeV and 578 MeV for the two ensembles. The ensemble for the lighter pion mass had 430 gauge configurations, and for the heavier pion mass, 363 configurations.

The bare speed of light was tuned by measuring the π and ρ energies for momenta $\vec{p} = \frac{2\pi\vec{n}}{L_s}$ with $\vec{n} = (0, 0, 0)$, $(1, 0, 0)$, $(1, 1, 0)$, and $(2, 0, 0)$ (averaging over all possible directions of \vec{n}). We determined the fermion anisotropy through a linear fit of $E^2(\vec{p})$ as a function of \vec{p}^2 and using Eq. (4.45). It was found that setting $\nu = 1$ gave a renormalized fermion anisotropy consistent with 3. These fits are shown in Fig. 4.2. We summarize the parameters used for the two ensembles of gauge configurations in Table 4.2.

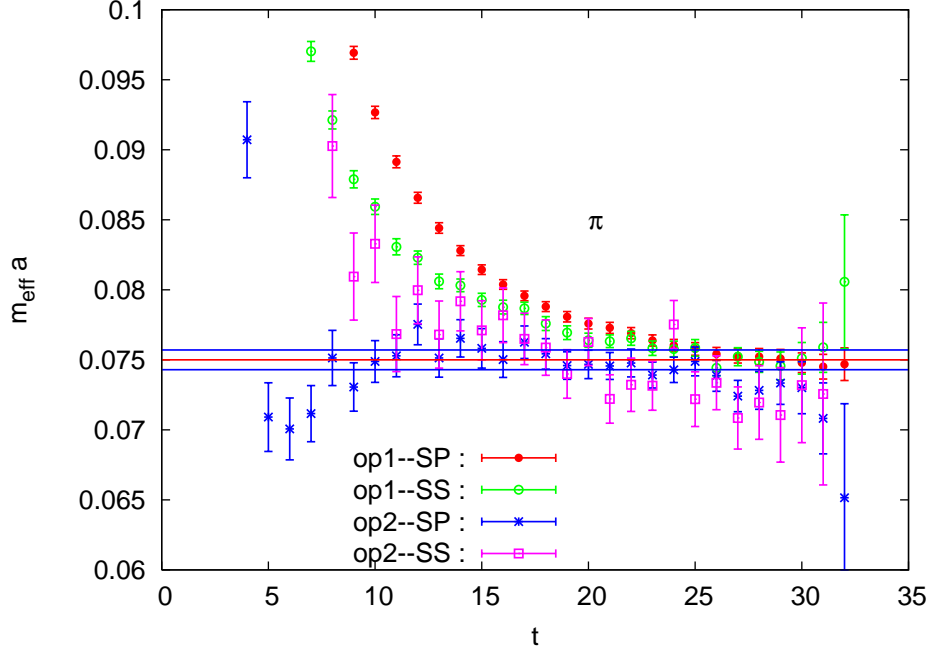


Figure 4.1: From [54], effective energies of correlation functions used to calculate the pion mass for the lattices with $m_\ell = -0.4125$. op1 indicates operators of the form $\bar{\psi}\gamma_5\psi$ while op2 indicates operators of the form $\bar{\psi}\gamma_5\gamma_4\psi$. Sources are smeared while sinks are both smeared (indicated by SS) and point source (indicated by PS). The horizontal band is the pion mass with statistical errors, as determined by fitting the correlators.

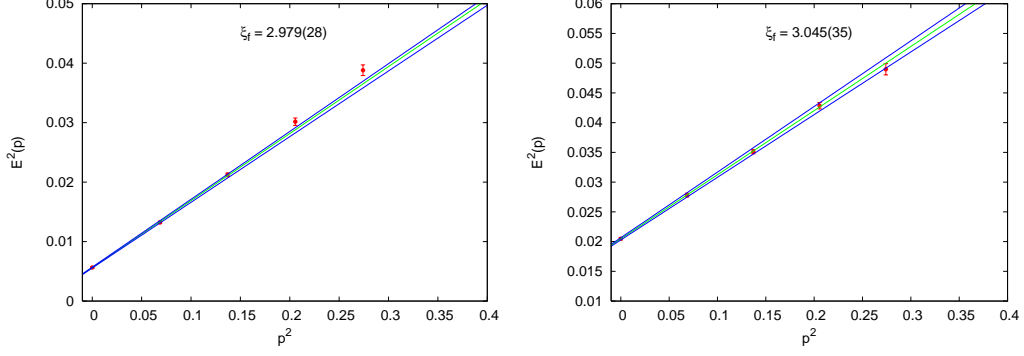


Figure 4.2: From [54], energies of pion (left) and ρ (right) states with different momenta and corresponding fits (with error bands) to the energy-momentum dispersion relation, Eq. (4.45). With the bare speed of light $\nu = 1$, the fermion anisotropy is consistent with 3, the gauge anisotropy.

4.4.1 Smearing Parameters

The smearing parameters were optimized for the extraction of the low lying baryon spectrum [49, 30]. As was shown in Fig. 3.1, quark smearing is crucial for reducing the coupling of operators to higher energy states and gauge link smearing is crucial for reducing noise. The effective energy was used as to judge the effectiveness of the smearing; in particular the effective energy at fixed time, $t = 4$ was used to tune the quark smearing parameters, and the jackknife error at that time was used to tune the link smearing parameters. This study was done on 50 quenched $12^3 \times 48$ lattices with $a_s \sim 0.1$, $a_s/a_t \sim 3$, and a pion mass of about 700 MeV.

The smearing matrix is defined to be

$$J_{ab}(\vec{x}, \vec{y}, t) = \left(1 + \frac{\sigma^2 \Delta(\vec{x}, \vec{y}, t)}{2n_\sigma} \right)_{ab}^{n_\sigma}, \quad (4.49)$$

which should approximate the operator $e^{\sigma^2 \vec{\nabla}^2/2}$. This approximation requires $n_\sigma \gg$

Table 4.2: Parameters used in the generation of gauge configurations for $N_f = 2$ Wilson gauge and Wilson fermion lattices used in the nucleon spectrum calculation. The anisotropy is tuned to be consistent with $a_s/a_t = 3$. Corresponding lattice lengths and pion masses in lattice and physical units are also given.

$m_\ell a_t$	β	ξ_0	ν	r_0/a_s	a_s (fm)	a_t^{-1} (MeV)	$m_\pi a_t$	m_π (MeV)	N_U
-0.4086	5.5	2.38	1	4.10(8)	0.113(7)	5310(265)	0.1088(37)	578(29)	363
-0.4125	5.5	2.38	1	4.26(12)	0.108(7)	5556(333)	0.0750(24)	416(36)	430

σ . As we make σ large for fixed n_σ and the approximation starts to break down, higher energy modes begin to contribute more significantly than in the unsmeared operators. It is thus necessary to tune the parameters to avoid “over-smearing”. Link smearing was used to reduce the noise in the effective energies of correlation functions. The link smearing parameters ρ and n_ρ were first optimized for unsmeared operators, giving $n_\rho = 16$ and $n_\rho \rho = 2.5$. Fixing these parameters, the quark smearing parameters σ and n_σ were varied and the effective energy was measured for several different operators. For small σ , $E_{eff}(4)$ was independent of n_σ . As σ was increased, initially the effective energy decreased, indicating the coupling to higher energy states was decreasing, but if it was made too large, $E_{eff}(4)$ began to rapidly increase. The threshold where this occurred increased with n_σ . These results are shown in Fig. 4.3.

Fixing $\sigma = 4$ and $n_\sigma = 32$, the link smearing parameters were then varied. The jackknife error on the effective energy at $t = 4$ was measured for various correlation

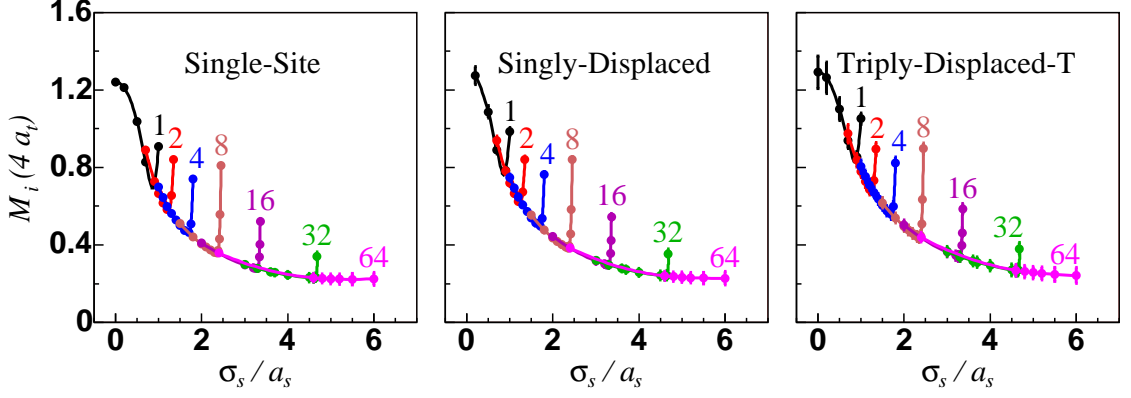


Figure 4.3: From [49], effective energy at $t = 4$ for a single-site, singly-displaced, and a triply-displaced-T nucleon operator as a function of σ_s for various choices n_σ , as indicated by the numbers on the plot. Gauge link smearing with $n_\rho = 16$ and $n_\rho \rho = 2.5$ is used. Results are based on 50 quenched configurations on $12^3 \times 48$ lattices with $a_s \sim 0.1$ fm, $a_t/a_s \sim 3.0$, and $m_\pi \sim 700$ MeV.

functions. The results were qualitatively similar to the quark smearing results. For small ρ , the jackknife error was independent of n_ρ . The error decreased with increasing ρ until a threshold was reached where the jackknife error began to rapidly increase. This threshold increased with n_ρ . The effect of link smearing on the static quark potential was also examined. In this case, the link smearing is analogous to quark smearing; it should reduce the coupling of the Wilson loop to higher energy modes. The Wilson loop was measured for a spatial separation of $5a_s$ at $t = 0$ for the same set of ρ and n_ρ . The results were again similar to the quark smearing case. Plots of the static quark potential and the jackknife errors on the correlators are shown in Fig. 4.4.

It was also observed that increasing the quark smearing radius increased the

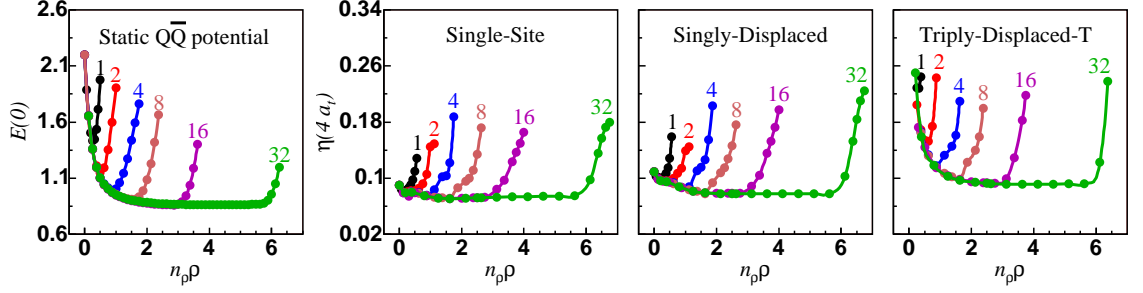


Figure 4.4: From [49], jackknife error in the effective energy at $t = 4$ for a single-site, singly-displaced, and a triply-displaced-T nucleon operator as a function of $n_\rho\rho$ for various choice of n_ρ , as indicated by the numbers on the plot. Quark smearing with $\sigma_s = 4.0$ and $n_\sigma = 32$ is used. Results are based on 50 quenched configurations on $12^3 \times 48$ lattices with $a_s \sim 0.1$ fm, $a_t/a_s \sim 3.0$, and $m_\pi \sim 700$ MeV. Also shown is the static quark potential at a separation of $R = 5$ at $t = 0$ calculated on at 16^4 lattice with $\beta = 6.0$.

noise in excited states, as shown in Fig. 4.5. Based on all these results, the smearing parameters were selected to be $\sigma = 3.0$, $n_\sigma = 32$, $n_\rho = 2.5$, and $n_\rho = 16$.

4.5 Operator Pruning

From Table 3.7, there are 179 nucleon operators in the G_1 channels, 144 in the G_2 channels, and 321 in the H_g channels. These large sets of operators were pruned down to optimized sets of 16 operators in each channel [30]. The criteria for choosing the operators was that they have low intrinsic noise and minimal linear dependence. It was also required that the positive and negative parity irreps both have the same operators so that Eq. (4.30) could be used to improve the statistics.

The effective energies of the diagonal elements of the correlation matrices for the positive parity irreps were used to prune based on noise. For each operator, the jackknife error in the effective energy was averaged over $t = 1 \dots 16$. For each displacement pattern, the operators with the ten lowest average jackknife errors were kept. All single-site operators were kept. The same operators were kept in the negative parity irreps.

The next step was to select a set of these low noise operators which coupled to states which were as linearly independent as possible. First a normalized correlation matrix was \hat{C}_{IJ} defined

$$\hat{C}_{IJ} = \frac{C_{IJ}(1)}{\sqrt{C_{II}(1)C_{JJ}(1)}}, \quad (4.50)$$

and the condition number of this matrix, the ratio of the largest eigenvalue to the smallest eigenvalue, was used to measure the linear independence of the operators.

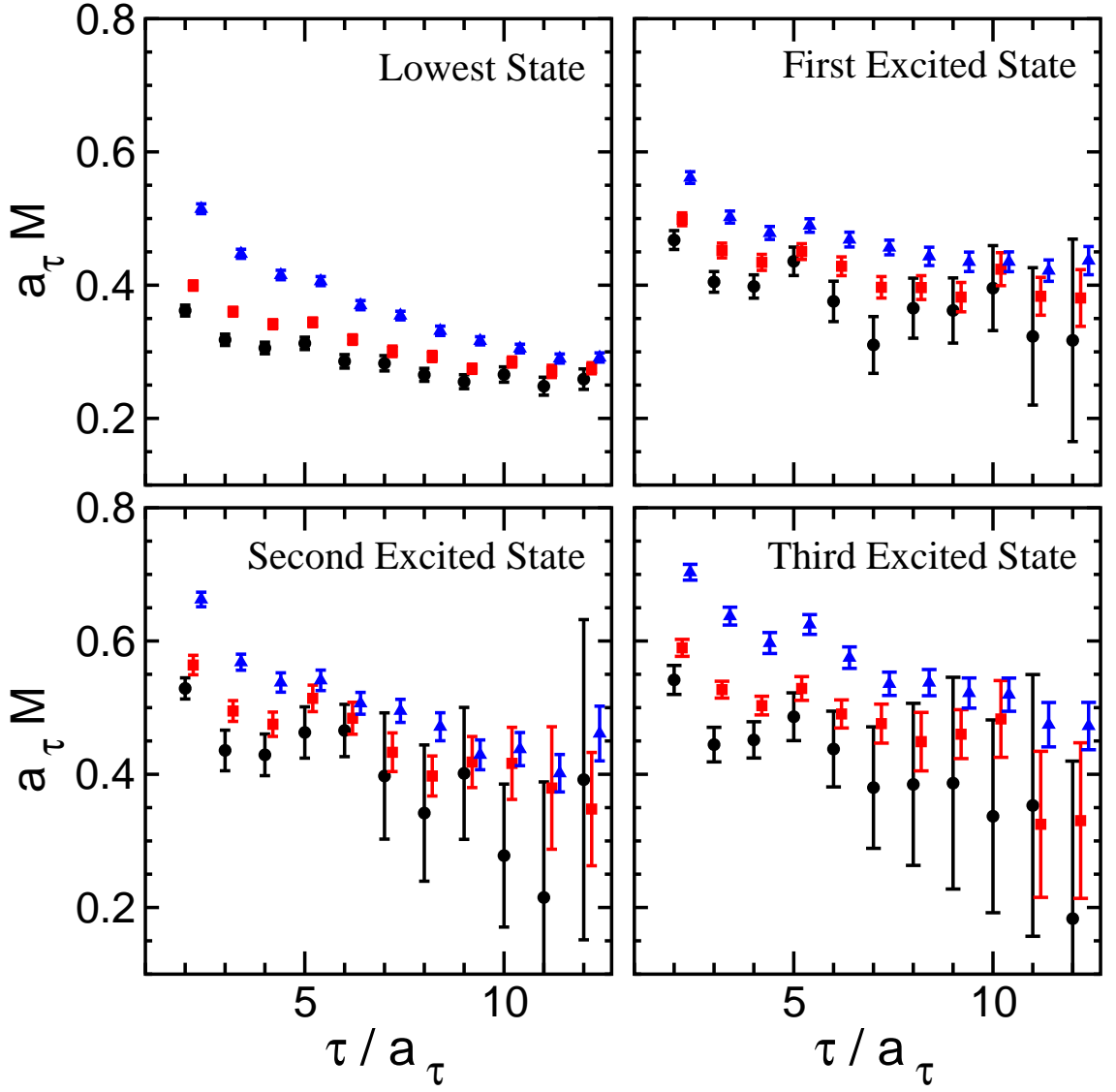


Figure 4.5: From [30] effective energy of the nucleon G_{1g} ground and three excited states for different choices of the Gaussian quark smearing radius. Link smearing with $n_\rho \rho = 2.5$ and $n_\rho = 16$ is used throughout. For the quark smearing we have $n_\sigma = 32$ and $\sigma_s=4.0$ (black circles), $\sigma_s = 3.0$ (red squares), and $\sigma_s = 2.0$ (blue triangles). Decreasing the quark smearing radius improves the noise in excited states.

In the extreme case where the operators were all orthogonal, all eigenvalues of \hat{C}_{IJ} would be equal to 1, as would the condition number. In the other extreme case where the operators were linearly dependent, one of the eigenvalues would be 0 and the condition number would diverge. Operators were selected so as to minimize the condition number of the renormalized matrix.

First, pruning was done only within each displacement pattern. The full 10×10 correlator matrix was calculated for the ten operators of each displacement type for all the irreps. Using a singular value decomposition, the condition number of the normalized correlation matrix was calculated for all possible 5×5 subsets of operators. We define

$$\kappa_{>}^{\Lambda}(x) = \max_x \left(\kappa^{\Lambda_g}(x), \kappa^{\Lambda_u}(x) \right), \quad (4.51)$$

where $\kappa^{\Lambda_g}(x)$ is the condition number of the normalized correlation matrix for a set of five operators x in positive parity irrep Λ_g , and $\kappa^{\Lambda_u}(x)$ is the condition number for the matrix in the corresponding negative parity irrep. The set of five operators in each channel which minimized $\kappa_{>}^{\Lambda}(x)$ was chosen, assuring good linear independence in both positive and negative parity irreps. Once again, all single-site operators were chosen.

After this step, there remained 23 G_1 operators, 20 G_2 operators, and 21 H operators. These sets were pruned to the 16 best operators based on the condition number of normalized correlation matrix by the same procedure as the pruning within the displacement types. The final sets of pruned operators are given in Appendix A.

4.6 Backward State Contamination

As discussed above, baryon creation operators of parity p create a state of parity p which propagates forward in time and a state of parity $-p$ which propagates backward in time. With the periodic boundary conditions, we see this in the correlation functions as a sum of exponential decays propagating backward from the opposite temporal end of the lattice. For an irrep Λ of parity p ,

$$C_{IJ}^\Lambda = \sum_n Z_{nI}^* Z_{nJ} e^{-E_n^\Lambda t} + \sum_n Z_{nI}'^* Z_{nJ}' e^{-E_n^{-\Lambda}(L-t)}, \quad (4.52)$$

where Z_{nI} is the coupling of the I^{th} operator in Λ to the n^{th} energy eigenstate within Λ , and Z_{nI}' is the coupling of the corresponding opposite-parity operator to the n^{th} energy eigenstate in $-\Lambda$. As the backward-in-time part propagates, it decays exponentially, eventually reaching the level of the noise. At earlier times, the correlation function is described only by the forward-in-time propagating state. By restricting ourselves to just these slices, we can ignore the backward signal and extract the energy spectrum in the usual way. As an example, Fig. 4.6 shows the G_{1g} ground state. The backward signal dominates for timeslices greater than $t = 38$ or so. It is insignificant for timeslices below $t = 30$ or so. We extract the energy spectrum by ignoring timeslices higher than $t = 30$.

Every channel looked very similar to this, except for the G_{1u} channel in the ensemble with $m_\pi = 416$ MeV. In that channel, the backward propagating state is dominated by the G_{1g} ground state, which is the lowest energy state in the nucleon spectrum. With the anisotropy, the time extent of the lattice was sufficiently small and the G_{1g} ground state decayed sufficiently slowly, that the backward signal con-

taminated the G_{1u} signal even on small time slices. In Fig. 4.7, we show the G_{1u} ground state. The backward signal dominates for timeslices greater than $t = 23$ or so. Even at time slices as low as $t = 12$, there is small, but detectable backward state contamination. We had to modify our analysis for this channel due to the presence of this contamination.

4.7 Operator Rephasing

We attempted to make the correlators real through a rephasing of the operators

$$B_I^\Lambda \rightarrow e^{i\phi_I} B_I^\Lambda, \quad (4.53)$$

and corresponding transformation of the correlation functions.

$$C_{IJ}(t) \rightarrow e^{i(\phi_I - \phi_J)} C_{IJ}(t). \quad (4.54)$$

By choosing the ϕ_I correctly, we observed that all elements of the correlator matrix could be made real.

As rephasing every operator by a constant phase does not change the correlator matrix, we can set $\phi_1 = 0$ and then determine the $N - 1$ relative phases between the operators, by measuring the phase of $C_{1i}(t)$ at $t = 1$,

$$\phi_I = \arctan \left(\frac{\text{Im}(C_{1I}(1))}{\text{Re}(C_{1I}(1))} \right). \quad (4.55)$$

We found that for all the channels, every phase was, within error bars, equal to 0, $\pi/2$, π , or $3\pi/2$. In fact, if all matrix elements could be made real through a rephasing of the operators, then every single matrix element would have phase

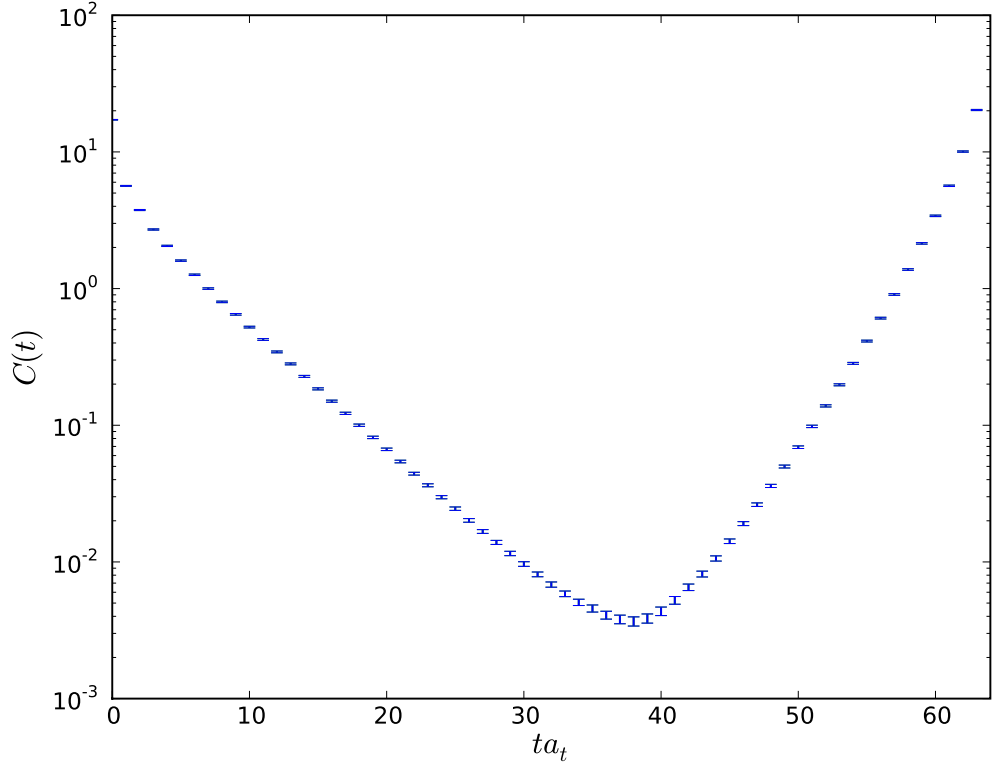


Figure 4.6: Nucleon G_{1g} ground state correlator at $m_\pi = 416$ MeV obtained using the variational method. We used the fixed eigenvector method with $t_0 = 7$ and $t^* = 10$ (as described in Section 4.8). There is no backward state contamination for $t < 30$ or so.

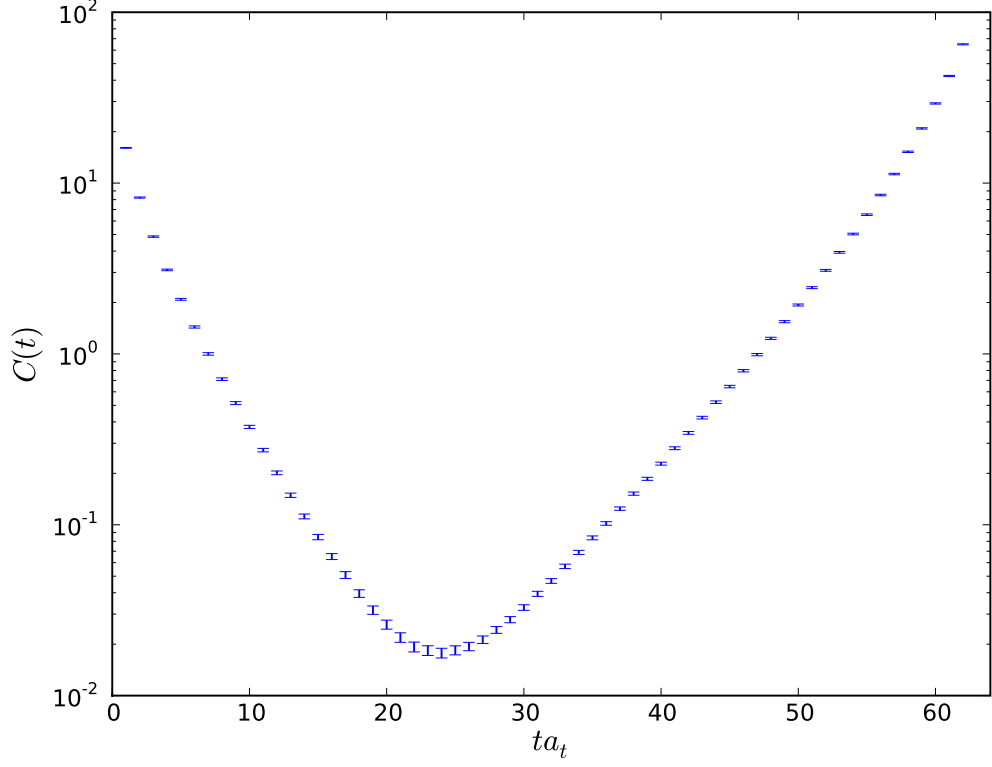


Figure 4.7: Nucleon G_{1u} ground state correlator at $m_\pi = 416$ MeV obtained using the variational method. We used the fixed eigenvector method with $t_0 = 7$ and $t^* = 9$ (as described in Section 4.8). Backward state contamination occurs even at timeslices as small as $t = 12$ or so.

equal (within error bars) to one of these four values. Indeed, this was the case, as shown in Fig. 4.8. Essentially, each matrix element had a real or imaginary part equivalent to zero. We therefore rounded each measured phase to the closest multiple of $\pi/2$. The rephased correlators had a small imaginary part, which we assumed to be noise and dropped.

It is important to consider the time dependence of the measured phase. We found that corresponding operators in opposite parity channels had phases which were complex conjugates of each other. Therefore, for those matrix elements which were completely imaginary, the forward and backward propagating parts of a correlator had different phases. The time dependence of one such correlator is shown in Fig. 4.9. At times where the forward propagating signal dominates, the phase is constant. As the backward signal become significant, the phase rapidly changes sign and then becomes constant again at times where the correlator is dominated by the backward propagating part. The phases for the forward and backward part are equal in magnitude, but have opposite signs. This time dependence of the phase is only a problem in the G_{1u} channel, as in all other channels we effectively ignore time slices where the backward propagating part of the correlator is significant. In the G_{1u} channel we did not do the rephasing.

4.8 The Variational Method

When we use the variational method, we rotate the correlation matrix to a new basis (the basis of eigenvectors obtained from the diagonalization) in which the

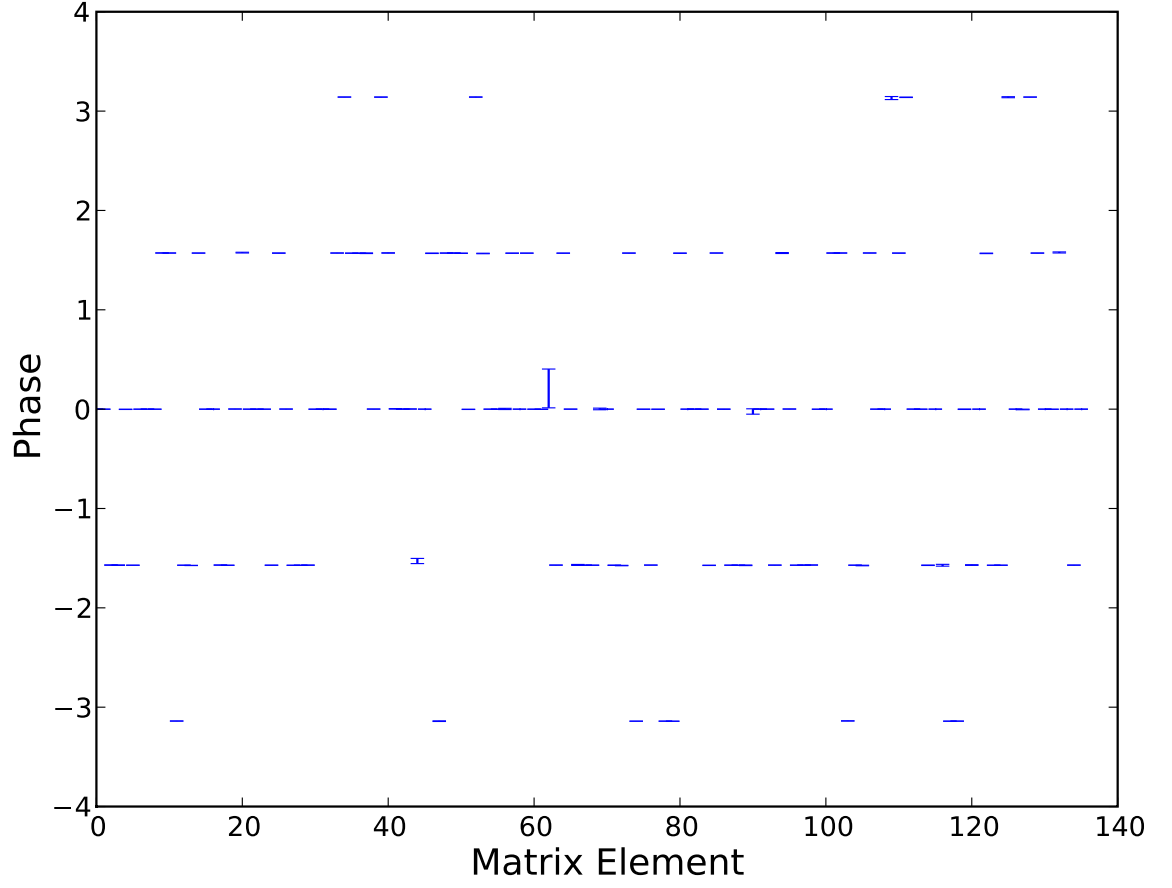


Figure 4.8: Phases of the matrix elements of the G_{1g} nucleon correlator matrix at $t = 1$ for the 136 upper triangle elements. Every phase is consistent with 0, $\pm\pi/2$, or $\pm\pi$.

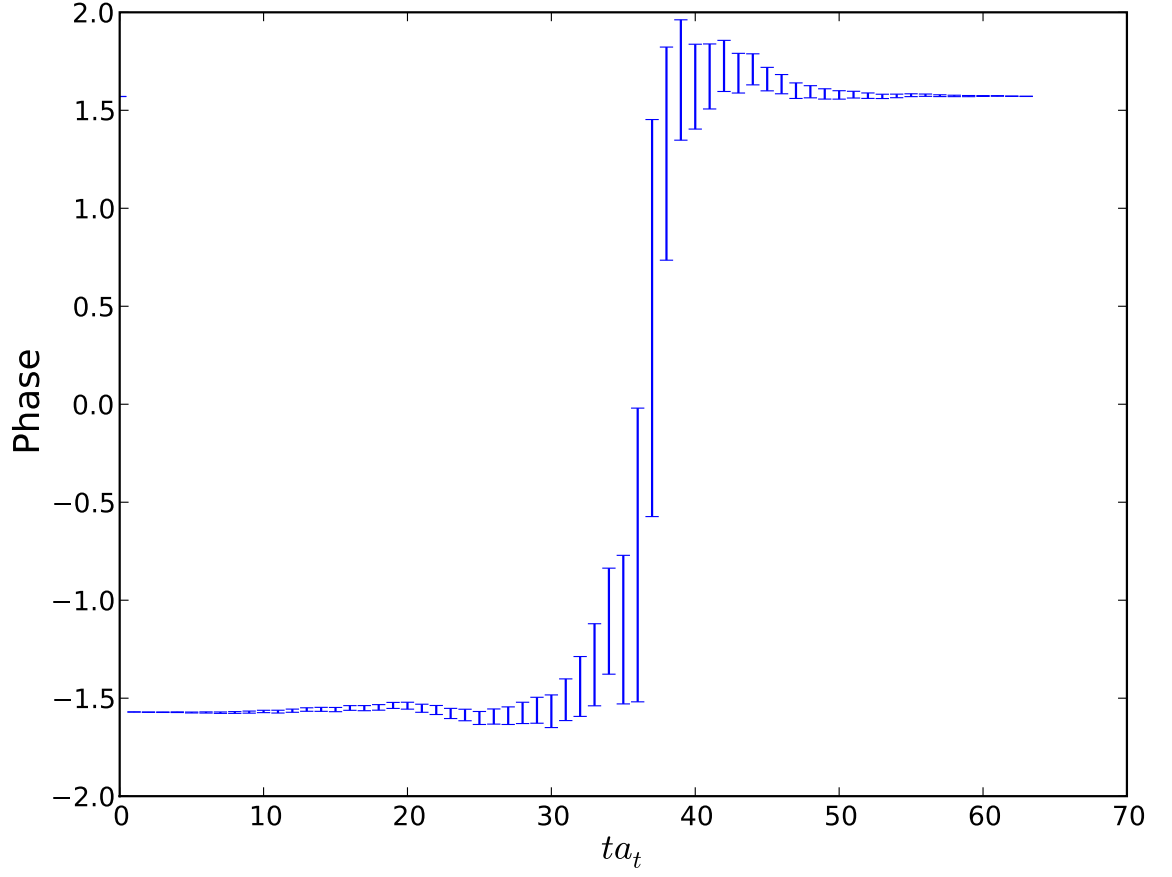


Figure 4.9: Time dependence of the phase of an imaginary correlator matrix element. The forward and backward states have phases of opposite sign. Early times are dominated by the forward state and late times by the backward state. In the middle there is a rapid transition from the phase of the forward state to that of the backward state.

matrix is diagonal. This new basis of nucleon operators, which we denote $\tilde{B}_i^N(t)$, has the property

$$\langle \Omega | \tilde{B}_i^N(t_f) \tilde{B}_j^N(t_i) | \Omega \rangle = \lambda_i(t) \delta_{ij}, \quad (4.56)$$

where $\lambda_i(t)$ is the i^{th} eigenvalue in the diagonalization, and the time dependence of the \tilde{B}_i^N is given by

$$\tilde{B}_i^N(t) = e^{Ht} \tilde{B}_i^N e^{-Ht}. \quad (4.57)$$

In practice, we have statistical errors in the correlation matrices and the eigenvectors obtained by diagonalizing the correlator depend on time. There are two methods for handling this time dependence. The first is the principle correlator method, in which we diagonalize the correlator matrix on each time slice. The eigenvectors have some fluctuations as a function of time, which means the optimized operators have some time dependence not given by Eq. (4.57). These variations should be random and remain small within a time window in which the signal-to-noise ratio is large. Eq. (4.57) should then hold, up to small statistical fluctuations.

The second method is the fixed eigenvector method, in which we pick a particular time slice t^* on which to solve the eigenvalue equation and rotate the correlator matrix at all times to this basis of eigenvectors:

$$\tilde{C}_{IJ}^\Lambda(t; t^*, t_0) = V_{IK}^*(t^*, t_0) C_{KL}^\Lambda(t) V_{LJ}(t^*, t_0), \quad (4.58)$$

where $V(t^*, t_0)$ is the matrix whose columns are the eigenvectors of generalized eigenvalue problem

$$C_{IJ}(t^*) v_{nI} = \lambda_n C_{IJ}(t_0) v_{nJ}, \quad (4.59)$$

for fixed t^* and t_0 . Since we use the same eigenvectors to diagonalize the matrix on all time slices, the optimal operators are fixed and Eq. (4.57) holds exactly. With fixed eigenvectors, the rotated correlation matrix is diagonal only at times t_0 and t^* , but the off-diagonal elements at all other times should be consistent with zero. The diagonal elements of the rotated matrix should approximate the eigenvalues of the principle correlator method, i.e.

$$\tilde{C}_{II}(t; t^*, t_0) = e^{-E_I(t-t_0)} [1 + \mathcal{O}(e^{-(E_{N+1}-E_I)(t-t_0)})], \quad (4.60)$$

for a sufficiently large t_0 , as described in Section 2.6.1. With such a choice of t_0 , the results should also remain independent of t^* (within statistical errors) for those t^* larger than t_0 , but small enough that the signal has not decayed to the noise level.

When there is significant backward state contamination, as in the G_{1u} channel at the lower pion mass, the time dependence of the eigenvalues obtained using the principle correlator method cannot be easily characterized. To see this, we first rewrite the Hamiltonian as

$$H = \sum_{\Lambda} H_{\Lambda}, \quad (4.61)$$

where

$$H_{\Lambda} = \sum_{n_{\Lambda}} E_{n_{\Lambda}} |n_{\Lambda}\rangle \langle n_{\Lambda}|. \quad (4.62)$$

The $\{|n_{\Lambda}\rangle\}$ are the eigenstates of the Hamiltonian which transform as rows of irrep Λ . When we use the variational method, we diagonalize the operator e^{-Ht} in some subspace of the Hilbert space. When the correlation functions are part of a single irrep Λ , this subspace only contains energy eigenstates which transform as Λ . Ignoring the backward-in-time propagating state, we effectively diagonalize $e^{-H_{\Lambda}t}$

in that subspace. Including the backward-in-time propagating state, which transforms as irrep $-\Lambda$, we effectively diagonalize the operator $e^{-H_\Lambda t} + e^{-H_{-\Lambda}(L_t-t)}$. In the typical case, early time slices are dominated only by the forward propagating signal, and when we diagonalize, we obtain eigenvectors of $e^{-H_\Lambda t}$. In this region, the eigenvectors remain stable, with only statistical fluctuations. Likewise, late times are dominated by the backward propagating signal and when we diagonalize we obtain eigenvectors of $e^{-H_{-\Lambda}(L_t-t)}$. Again, in this region the eigenvectors remain stable within statistical fluctuations. In the middle, we have some combination of the two and we expect the eigenvectors to be transforming from eigenvectors of $e^{-H_\Lambda t}$ to $e^{-H_{-\Lambda}(L_t-t)}$, and thus rapidly changing from time slice to time slice. In this region, the optimized operators have a non-trivial time dependence which cannot be described by Eq. (4.57). In effect, we are calculating the correlation function of different operators on every time slice. As a result when we used the principle correlator method in the G_{1u} channel, the exact time dependence of the eigenvalues was unclear. In contrast, when we used the fixed eigenvector method, we transformed the correlation matrix the same way on every time slice. The backward propagating part was still present in the diagonal elements of the rotated correlator matrix, but we knew exactly what its expected time dependence was:

$$\tilde{C}_{II}^{G_{1u}}(t; t^*, t_0) = Ae^{-E_I^{G_{1u}}(t-t_0)} + Be^{-E_0^{G_{1g}}(L_t-t)}, \quad (4.63)$$

where $E_I^{G_{1u}}$ is the energy of I^{th} G_{1u} level and $E_0^{G_{1g}}$ is the G_{1g} ground state energy. We extracted the G_{1u} energy levels by using the fixed eigenvector method and including the backward propagating G_{1g} ground state in the fit. We used the fixed eigenvector

method on all channels for both pion masses.

4.8.1 Filtering

We also tested a method which attempted to filter out the backward propagating part of the correlator prior to the diagonalization, allowing the use of the principle correlator method [64]. We assume that there is a time t_1 where for all $t < t_1$, elements of the correlation matrix can be written in the form

$$C_{IJ}^\Lambda(t) = \sum_n Z_{nI}^* Z_{nJ} e^{-E_n^\Lambda t} + Z_{0I}^{\prime*} Z_{0J}' e^{-E_0^{-\Lambda}(L_t-t)}. \quad (4.64)$$

We define the filtered correlator matrix

$$C_{filt,IJ}^\Lambda(t) \equiv C_{IJ}^\Lambda(t) - C_{IJ}^\Lambda(t_1) + (1 - e^{-E_0^{-\Lambda}}) \sum_{j=t+1}^{t_1} C_{IJ}^\Lambda(j), \quad (4.65)$$

$$\begin{aligned} &= \sum_n \left(Z_{nI}^* Z_{nJ} e^{-E_n^\Lambda t} + Z_{nI}^{\prime*} Z_{nJ}' e^{-E_0^{-\Lambda}(L_t-t)} \right) \\ &\quad - \sum_n \left(Z_{nI}^* Z_{nJ} e^{-E_n^\Lambda t_1} + Z_{nI}^{\prime*} Z_{nJ}' e^{-E_0^{-\Lambda}(L_t-t_1)} \right) \\ &\quad + (1 - e^{-E_0^{-\Lambda}}) \sum_{j=t+1}^{t_1} \left(Z_{nI}^* Z_{nJ} e^{-E_n^\Lambda j} + Z_{nI}^{\prime*} Z_{nJ}' e^{-E_0^{-\Lambda}(L_t-j)} \right), \end{aligned} \quad (4.66)$$

$$= \sum_n Z_{nI}^* Z_{nJ} \left[1 + \frac{1 - e^{-E_0^{-\Lambda}}}{e^{E_n^\Lambda} - 1} \right] \left(e^{-E_n^\Lambda t} - e^{-E_n^\Lambda t_1} \right). \quad (4.67)$$

As before, we solve the generalized eigenvalue problem

$$C_{filt,IJ}^\Lambda(t) v_{nJ} = \lambda_n C_{filt,IJ}^\Lambda(t_0) v_{nJ}. \quad (4.68)$$

We analyze this problem as in Section 2.6.1, considering the case where the number of energy eigenstates contributing to the correlator matrix is equal to the rank of

the matrix. We get for the eigenvalues,

$$\lambda_n^{(0)}(t) = \left(e^{-E_n^\Lambda t_0} - e^{-E_n^\Lambda t_1} \right)^{-1} \left(e^{-E_n^\Lambda t} - e^{-E_n^\Lambda t_1} \right), \quad (4.69)$$

$$\approx e^{E_n^\Lambda t_0} \left(1 + e^{-E_n^\Lambda (t_1 - t_0)} \right) \left(e^{-E_n^\Lambda t} - e^{-E_n^\Lambda t_1} \right), \quad (4.70)$$

$$\approx e^{-E_n^\Lambda (t - t_0)} - e^{-E_n^\Lambda (t_1 - t_0)}. \quad (4.71)$$

The filtering enables us to perform a principle correlator analysis on the correlator matrix. We can then extract the energy spectrum by including a constant term in the fit of the eigenvalues. We did not find any advantage to using the principle correlator method with filtered correlators, as opposed to the fixed eigenvector method.

4.8.2 Choosing t_0 and t^*

We find optimal values for the two parameters which enter into the fixed eigenvector method, t_0 and t^* . Choosing optimal values for these parameters balances the improved signal-to-noise ratio in the correlator at earlier times and the reduction in the excited state contamination which occurs at larger t_0 . To determine the optimal choices, we used a method adapted from that in [65], which selected the optimal t_0 for the principle correlator method. For an $N \times N$ correlator matrix, the ideal choice for t_0 would be the time when the matrix is saturated by exactly N states. At that time, the correlation matrix is described by

$$C_{IJ}(t) = \sum_{n=1}^N Z_{nI}^* Z_{nJ} e^{-E_n t}. \quad (4.72)$$

The number of energy eigenstates contributing to the correlator is equal to the rank of the correlator matrix. From the discussion Section 2.6.1, each eigenvalue from

the generalized eigenvalue problem has a contribution from only a single energy eigenstate. By fitting all N eigenvalues, we obtain the energies of the first N states. We can also compute the Z_{nI} from the eigenvectors,

$$Z_{nI} = (V^{-1})_{nI} e^{-E_n t_0/2}. \quad (4.73)$$

We can then reconstruct the correlation function from the extracted energies and Z_{nI} using Eq. (4.72). With this ideal choice of t_0 , the reconstructed correlator should be close to the actual correlator for $t > t_0$. The reconstructed correlator will differ from the actual correlator if t_0 is chosen too small and there are large contributions to the correlator from excited states above the N^{th} state or if t_0 is chosen to be too large and the energies and Z_{nI} are poorly determined due to the increased noise. A χ^2 -like quantity was used to determine how well the reconstructed correlator replicated the original correlator:

$$\begin{aligned} \chi^2 = & \frac{1}{\frac{1}{2}N(N+1)(t_{max} - t_0) - \frac{1}{2}N(N+3)} \\ & \times \sum_{I,J \geq I} \sum_{t,t'=t_0+1}^{t_{max}} (C_{IJ}(t) - C_{IJ}^{rec}(t)) \mathbf{C}_{IJ}^{-1}(t,t') (C_{IJ}(t') - C_{IJ}^{rec}(t')), \end{aligned} \quad (4.74)$$

where $C_{IJ}^{rec}(t)$ is the reconstructed correlator matrix and \mathbf{C}_{IJ} is the correlation matrix.² The correlator is reconstructed for all timeslices larger than t_0 up to some maximum time t_{max} . The Z_{nI} have some time dependence due to the statistical

²This “correlation matrix” is the one used in statistics, the matrix of correlation coefficients between each measurement, and is not to be confused with the matrix of correlation functions of quantum mechanical operators.

fluctuations in the correlators. These fluctuations, similar to those in the eigenvectors themselves, should be minimal in a time window where the noise is small, leading to a relatively small dependence of χ^2 on the choice of $Z_{nI}(t)$. Let t_Z be the time where the $Z_{nI}(t)$ minimize the χ^2 . For each t_0 , the $\chi^2(t_Z)$ is calculated and the t_0 with the minimal χ^2 was used to compute the energy spectrum. Fig. 4.10, from [65] shows the dependence of the χ^2 on the choice of t_0 for the extraction of the charmonium spectrum. The χ^2 decreases with increasing t_0 , until a minimum is reached. Further increases to t_0 yield noisier results and a higher χ^2 .

We computed the optimal t_0 and t^* pair for the fixed eigenvector method in an analogous way; we selected t_0 and t^* such that the χ^2 for the reconstructed correlator was minimized. In fact, the optimal t^* should correspond to t_Z in the optimization for the principle correlator method. We found that for the optimal choice of t_0 , there was very little variation in the χ^2 with varying t^* , as shown in Fig. 4.11. The only real difference between the optimization of the two methods is how the energies are extracted; with the principle correlator method we fit the time dependent eigenvalues, while with fixed eigenvector method we fit the diagonal elements of the rotated correlator matrix.

To demonstrate what happens when we select a non-optimal t_0 and t^* , we first plot in Fig. 4.12 the reconstruction for a G_{1g} diagonal correlator using the optimal choice. For $t > t_0$, the correlator is consistent with the reconstruction, indicating the decomposition of the correlation function into individual energy levels has been done accurately (for smaller values of t , we do not expect agreement as the number of states which contribute to the correlation matrix is larger than the number used in

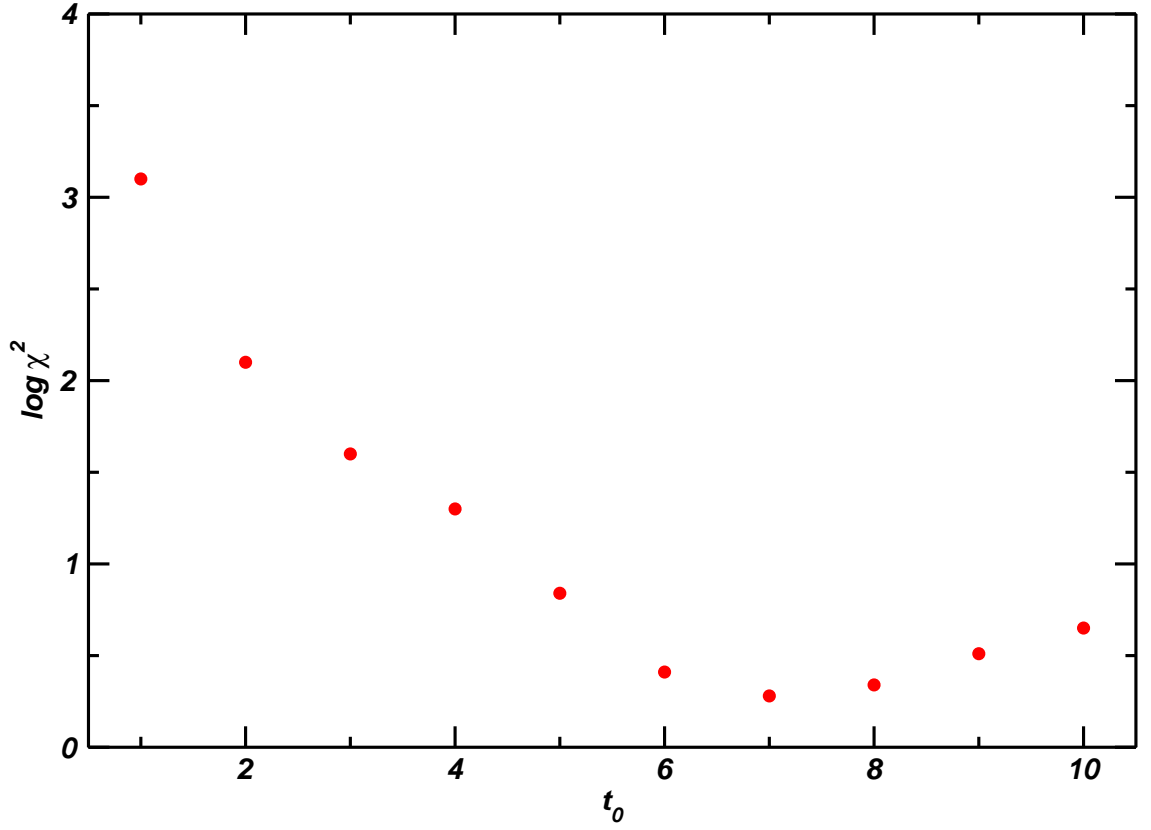


Figure 4.10: From [65], χ^2 of the reconstructed correlator matrix, Eq. (4.74), for charmonium, diagonalized using the principle correlator method, as a function of t_0 . Initially χ^2 decreases with increasing t_0 until a minimum is reached. Further increases to t_0 yield noisier results resulting in a higher χ^2 .

the reconstruction). To contrast, in Fig. 4.13, we plot the same correlation function but with a smaller choice of t_0 . At this non-optimal value, the correlator is not well described by the reconstruction, indicating we have inaccurately determined the spectrum.

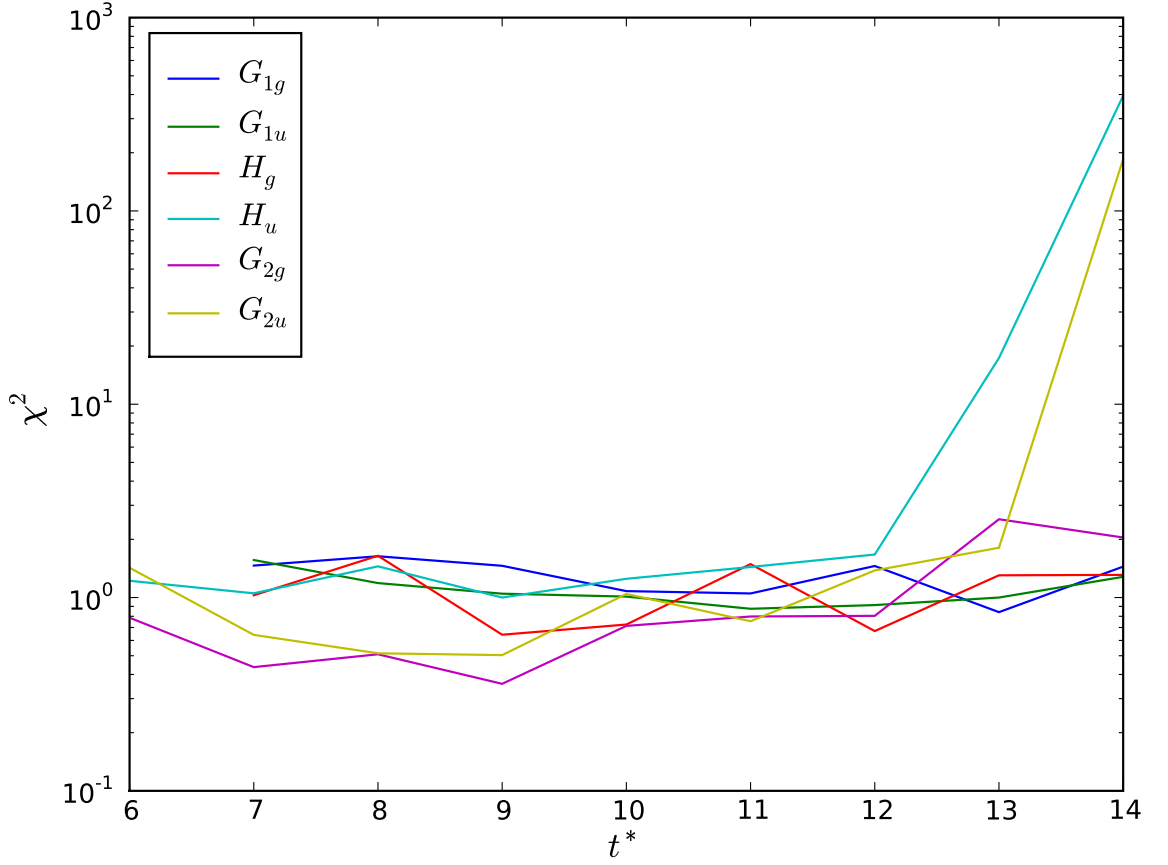


Figure 4.11: χ^2 for the reconstructed nucleon correlator matrices, diagonalized using the fixed eigenvector method, at the optimal t_0 and varying t^* . There are only small fluctuations in the χ^2 with increasing t^* until noise becomes significant.

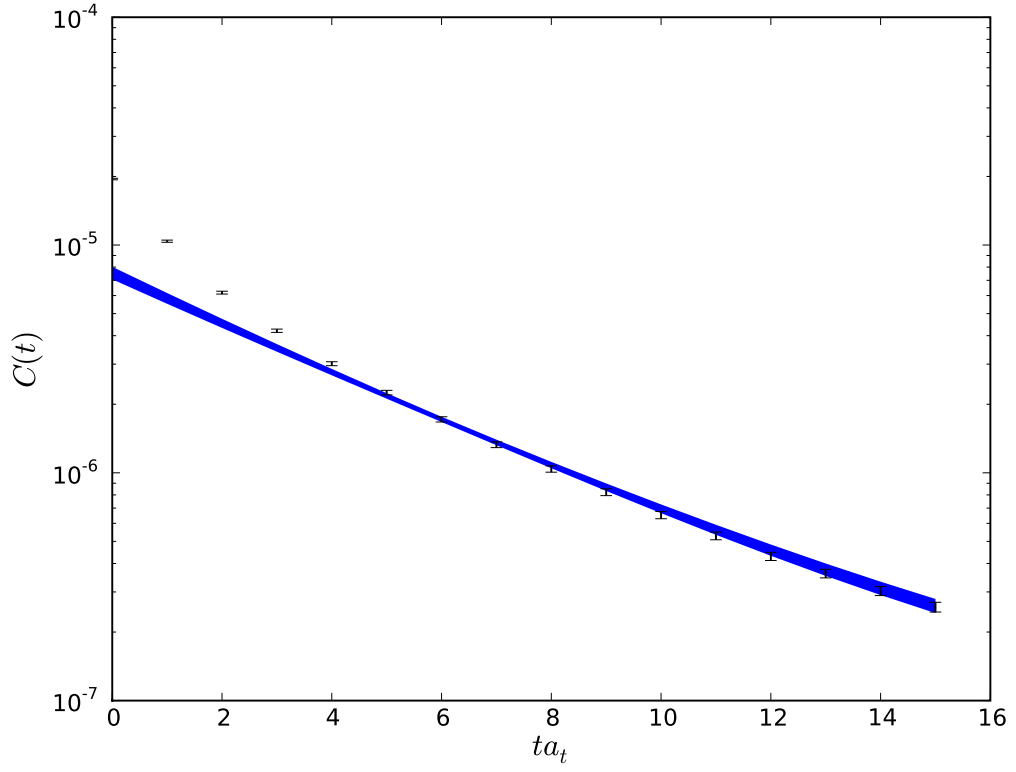


Figure 4.12: A diagonal G_{1g} nucleon correlator matrix element and its reconstruction, using the optimal choice for t_0 and t^* . The reconstruction and its jackknife error are indicated by the light blue band. For $t > t_0 = 6$, there is good agreement between the correlator and the reconstruction.

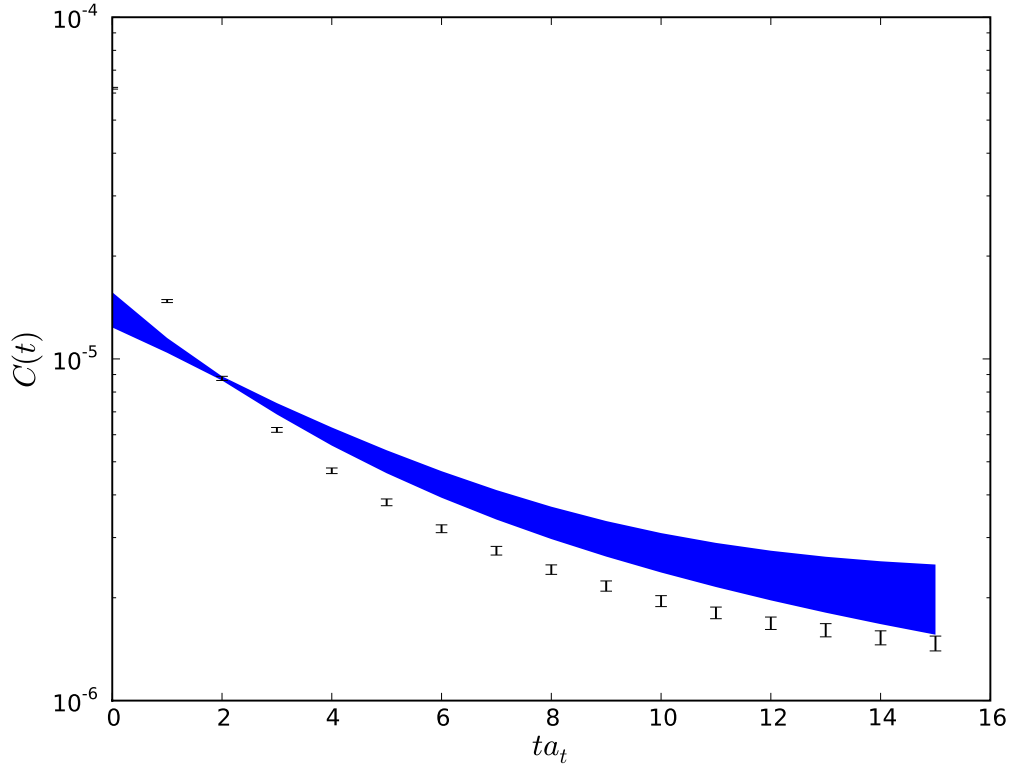


Figure 4.13: A diagonal nucleon G_{1g} correlator matrix element and its reconstruction, choosing t_0 smaller than the optimal value. The reconstruction and its jackknife error are indicated by the light blue band. Even at large times, the correlator does not agree with the reconstruction.

4.9 Fitting Method

To extract the correlation functions we did fully correlated χ^2 minimization fits [66]. We modeled the diagonal elements of the rotated correlation matrix as a double exponential decay,

$$\tilde{C}_{II}^{fit} = Ae^{-E_I(t-t_0)} + (1-A)e^{-E'(t-t_0)}. \quad (4.75)$$

The first exponential captures the dominant contribution to the correlator and has a decay constant equal to the I^{th} energy level, while the second exponential captures the corrections from other states. The generalized eigenvalue problem fixes the normalization of the diagonal elements to be exactly 1 at $t = t_0$ (with no statistical error). The coefficients in the fit function guarantee that it, too, is fixed to exactly 1 at $t = t_0$. With the optimized choices of t_0 , the contribution from the correction term should be small and E' should be higher than the N^{th} energy level we extract. When we include the correction, we are able to accurately model the correlator starting on time slices as early as 2.

To calculate the χ^2 we first calculate the covariance matrix

$$\sigma(t, t') = \frac{1}{N(N-1)} \sum_{i=1}^{N_U} (\tilde{C}_{II,i}(t) - \bar{\tilde{C}}_{II}(t))(\tilde{C}_{II,i}(t') - \bar{\tilde{C}}_{II}(t')), \quad (4.76)$$

where $t, t' \in [t_{min}, t_{max}]$, the range over which the fit is performed. We then compute

$$\chi^2 = \sum_{t, t'} (\tilde{C}_{II}(t) - \tilde{C}_{II}^{fit}(t))\sigma^{-1}(t, t')(\tilde{C}_{II}(t') - \tilde{C}_{II}^{fit}(t')). \quad (4.77)$$

We looked for a range of time slices over which to fit such that the χ^2 is minimized and the fit parameters are stable when we eliminate one of the end points of the fit.

We also checked the sensibility of the fit results. One technique would have been to look at the effective energy and to ensure that it plateaued to a value consistent with the energy obtained from the fit. However, the computation of the effective energy involves taking the difference in the correlator between successive time slices, which tends to enhance noise. To avoid this, we computed $\tilde{C}_{II}^\Lambda(t)e^{E_I^\Lambda(t-t_0)}$, which should plateau to a value consistent with the parameter A in Eq. (4.75).

In the G_{1u} channel at the lower pion mass, we included the backward-in-time propagating state in the fit. We required the energy of the backward state to have the same energy as the G_{1g} ground state by fitting the G_{1u} correlators simultaneously with the G_{1g} ground state:

$$C_{II}^{G_{1u}} = Ae^{-E_I^{G_{1u}}(t-t_0)} + Be^{-E_0^{G_{1g}}(L_t-t)} + (1-A-B)e^{-E'(t-t_0)}, \quad (4.78)$$

$$C_{00}^{G_{1g}} = A'e^{-E_I^{G_{1g}}(t-t_0)} + (1-A')e^{-E''(t-t_0)}. \quad (4.79)$$

These fits succeeded only for the lowest two energy levels in the G_{1u} channel. For higher energy levels, we obtained convergence from the fitter by modeling the forward-in-time propagating state in the G_{1u} channel as a single exponential and using a larger value for t_{min} . To test the sensibility of the parameters, we used a similar method as in the other channels. We calculated $(\tilde{C}_{II}^\Lambda(t) - Be^{-E_0^{G_{1g}}(L_t-t)})e^{E_I^\Lambda(t-t_0)}$ (subtracting off the backward signal and then proceeding as before) and confirmed that it plateaued to a value consistent with A .

The minimization of the χ^2 was performed using `pyminuit`, a python wrapper for the Minuit minimization package [67].

4.10 Results

We extracted four energy levels from each channel for both pion masses. We present the spectra, including the choices of t_0 and t^* and the ranges for the fits in Table 4.3 for the 416 MeV pion and Table 4.4 for the 578 MeV pion.

In Figs. 4.14-4.25, we plot $C_{II}^\Lambda(t)e^{E_I^\Lambda(t-t_0)}$ for the lowest four energy states in each channel.

4.10.1 Multi-particle Thresholds

In this work, we do not attempt to identify multi-hadron states in the spectrum. Instead, we estimate the energies of the lowest two particle state in each channel. The two particle states we consider are those consisting of a pion and the ground state in each channel. We allow the two particles to be at rest or have one unit of momentum each, in opposite directions. We estimate the energies of these states by simply taking the sum of the energies of the two particles. For single particle states with non-zero momentum, we calculate the energy with the dispersion relation. Finally, we determine in which channel each of these two particle states shows up. We report the lowest such state in each channel.

Given two single-particle states which transform as irreps Λ_1 and Λ_2 , we determine the transformation properties of the combined two-particle state by reducing the direct product $\Lambda_1 \otimes \Lambda_2$ to a direct sum of irreducible representations. We first consider states with both particles at rest. In the continuum, this would be a nucleon state with parity p and angular momentum J with a pion, which has negative

Table 4.3: The nucleon spectrum at $m_\pi = 416$ MeV with jackknife errors. We do not include the error in the the determination of the scale that acts as an overall multiplicative factor in the range 0.94 to 1.06.

$G_{1g}, t_0 = 7, t^* = 10$			$G_{1u}, t_0 = 7, t^* = 9$		
time	Ea_t	E (MeV)	time	Ea_t	E (MeV)
3 – 21	0.2044(18)	1136(10)	3 – 14	0.3146(61)	1748(34)
2 – 14	0.3747(126)	2082(70)	2 – 14	0.3343(67)	1857(37)
2 – 12	0.4177(137)	2321(76)	7 – 14	0.5014(136)	2786(76)
2 – 12	0.4201(277)	2334(154)	7 – 13	0.5238(158)	2910(88)
$H_g, t_0 = 8, t^* = 10$			$H_u, t_0 = 8, t^* = 9$		
time	Ea_t	E (MeV)	time	Ea_t	E (MeV)
3 – 16	0.4004(74)	2225(41)	3 – 23	0.3208(87)	1782(48)
3 – 17	0.4146(126)	2304(70)	3 – 21	0.3320(86)	1845(48)
3 – 18	0.4193(120)	2330(67)	3 – 19	0.3535(87)	1964(48)
3 – 16	0.4144(202)	2302(112)	2 – 11	0.5157(174)	2865(97)
$G_{2g}, t_0 = 6, t^* = 8$			$G_{2u}, t_0 = 6, t^* = 9$		
time	Ea_t	E (MeV)	time	Ea_t	E (MeV)
2 – 12	0.4448(122)	2471(68)	2 – 17	0.3523(92)	1957(51)
2 – 12	0.4593(104)	2552(58)	2 – 12	0.5035(119)	2797(66)
2 – 11	0.4659(110)	2589(61)	2 – 12	0.5373(162)	2985(90)
2 – 14	0.4796(127)	2665(71)	2 – 10	0.5446(131)	3026(73)

Table 4.4: The nucleon spectrum at $m_\pi = 578$ MeV with jackknife errors. We do not include the error in the the determination of the scale that acts as an overall multiplicative factor in the range 0.95 to 1.05.

$G_{1g}, t_0 = 6, t^* = 10$			$G_{1u}, t_0 = 6, t^* = 9$		
time	Ea_t	E (MeV)	time	Ea_t	E (MeV)
2 – 27	0.2463(17)	1308(9)	2 – 11	0.3719(48)	1975(25)
2 – 15	0.4291(110)	2279(58)	2 – 11	0.3811(56)	2024(30)
2 – 15	0.4643(116)	2465(62)	2 – 11	0.5186(141)	2754(75)
2 – 11	0.4631(123)	2459(65)	2 – 11	0.5431(121)	2884(64)
$H_g, t_0 = 6, t^* = 9$			$H_u, t_0 = 5, t^* = 7$		
time	Ea_t	E (MeV)	time	Ea_t	E (MeV)
2 – 14	0.4450(90)	2363(48)	2 – 11	0.3802(86)	2019(46)
2 – 11	0.4789(96)	2543(51)	2 – 11	0.3975(89)	2111(47)
2 – 11	0.4758(95)	2526(50)	2 – 11	0.4110(72)	2182(38)
2 – 11	0.4996(99)	2653(53)	2 – 11	0.5670(215)	3011(114)
$G_{2g}, t_0 = 5, t^* = 9$			$G_{2u}, t_0 = 5, t^* = 9$		
time	Ea_t	E (MeV)	time	Ea_t	E (MeV)
2 – 15	0.4422(144)	2348(76)	2 – 11	0.4017(81)	2133(43)
2 – 15	0.4887(113)	2595(60)	2 – 11	0.5223(188)	2773(100)
2 – 12	0.5030(94)	2671(50)	2 – 11	0.5399(139)	2867(74)
2 – 14	0.5035(108)	2674(57)	2 – 11	0.5601(142)	2974(75)

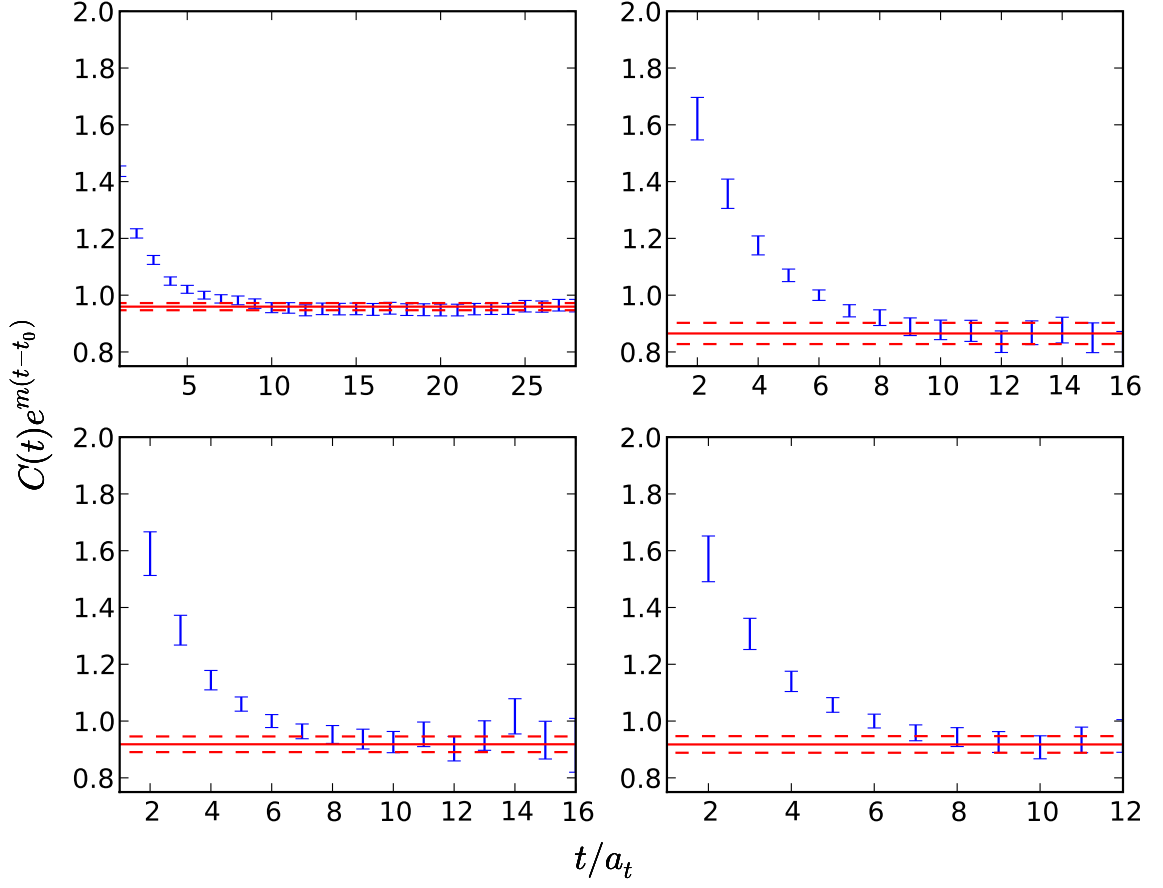


Figure 4.14: From [54], plots of $C_{II}^{\Lambda}(t)e^{E_I^{\Lambda}(t-t_0)}$ for the ground (top left), first excited (top right), second excited (bottom left) and third excited (bottom right) nucleon states in the G_{1g} channel at $m_{\pi} = 578$ MeV. The plot plateaus to the value of A in Eq. (4.75), as determined by the fit, indicated by solid horizontal line. Horizontal dotted lines are jackknife errors on A .

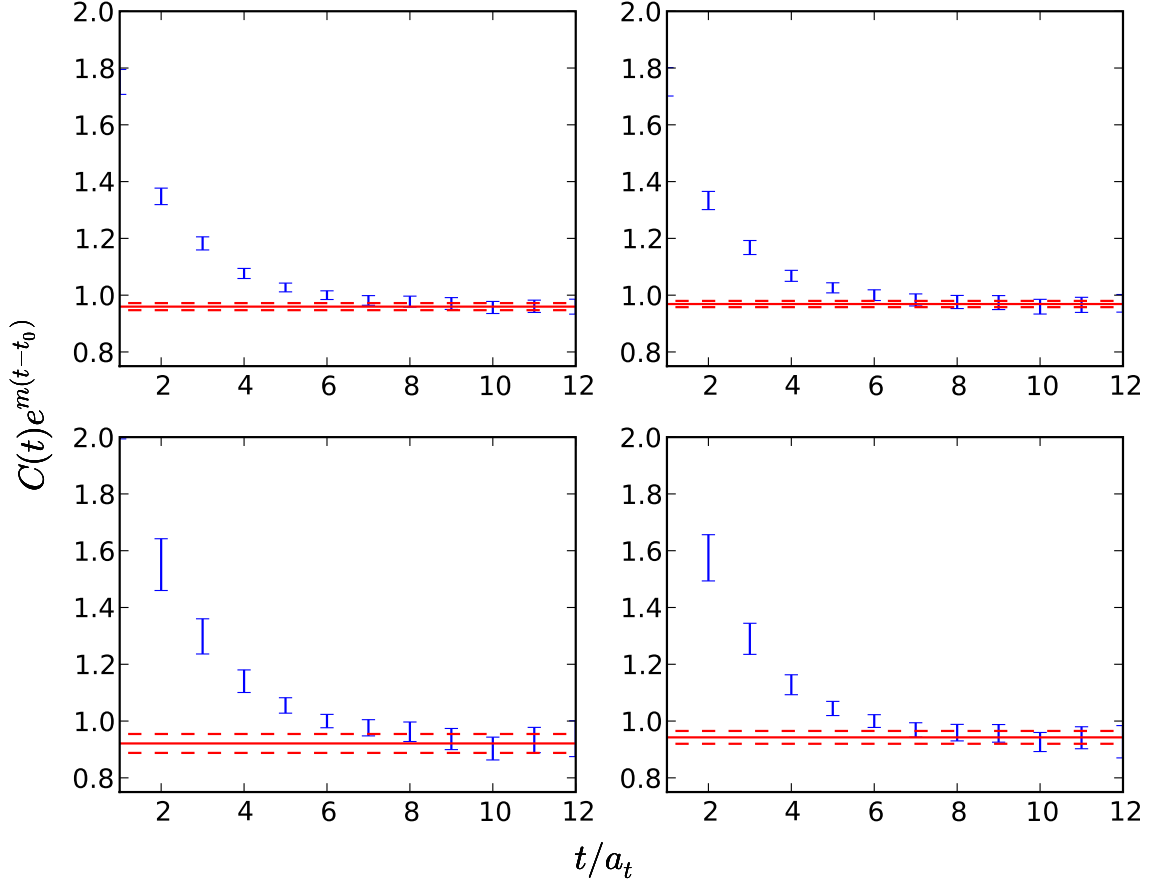


Figure 4.15: From [54], plots of $C_{II}^{\Lambda}(t)e^{E_I^{\Lambda}(t-t_0)}$ for the ground (top left), first excited (top right), second excited (bottom left) and third excited (bottom right) nucleon states in the G_{1u} channel at $m_{\pi} = 578$ MeV. The plot plateaus to the value of A in Eq. (4.75), as determined by the fit, indicated by solid horizontal line. Horizontal dotted lines are jackknife errors on A .

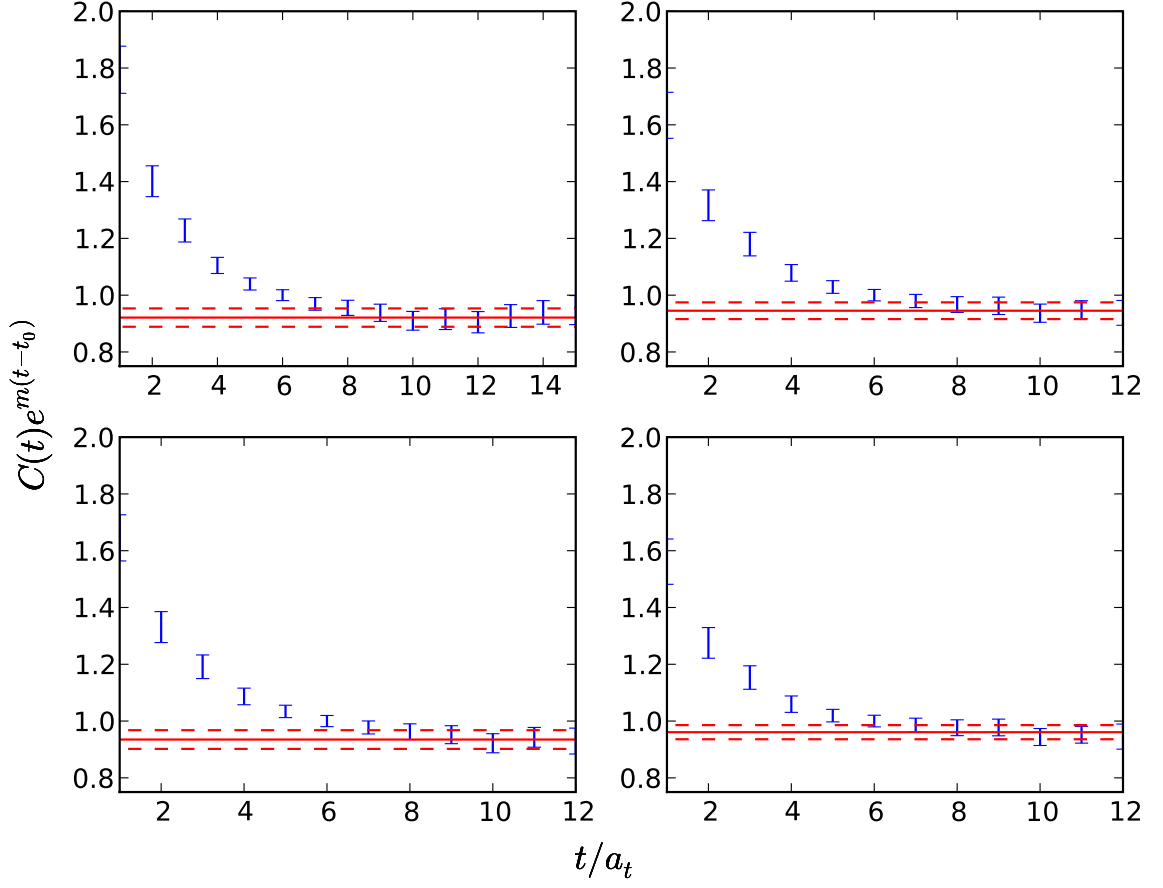


Figure 4.16: From [54], plots of $C_{II}^\Lambda(t)e^{E_I^\Lambda(t-t_0)}$ for the ground (top left), first excited (top right), second excited (bottom left) and third excited (bottom right) nucleon states in the H_g channel at $m_\pi = 578$ MeV. The plot plateaus to the value of A in Eq. (4.75), as determined by the fit, indicated by solid horizontal line. Horizontal dotted lines are jackknife errors on A .

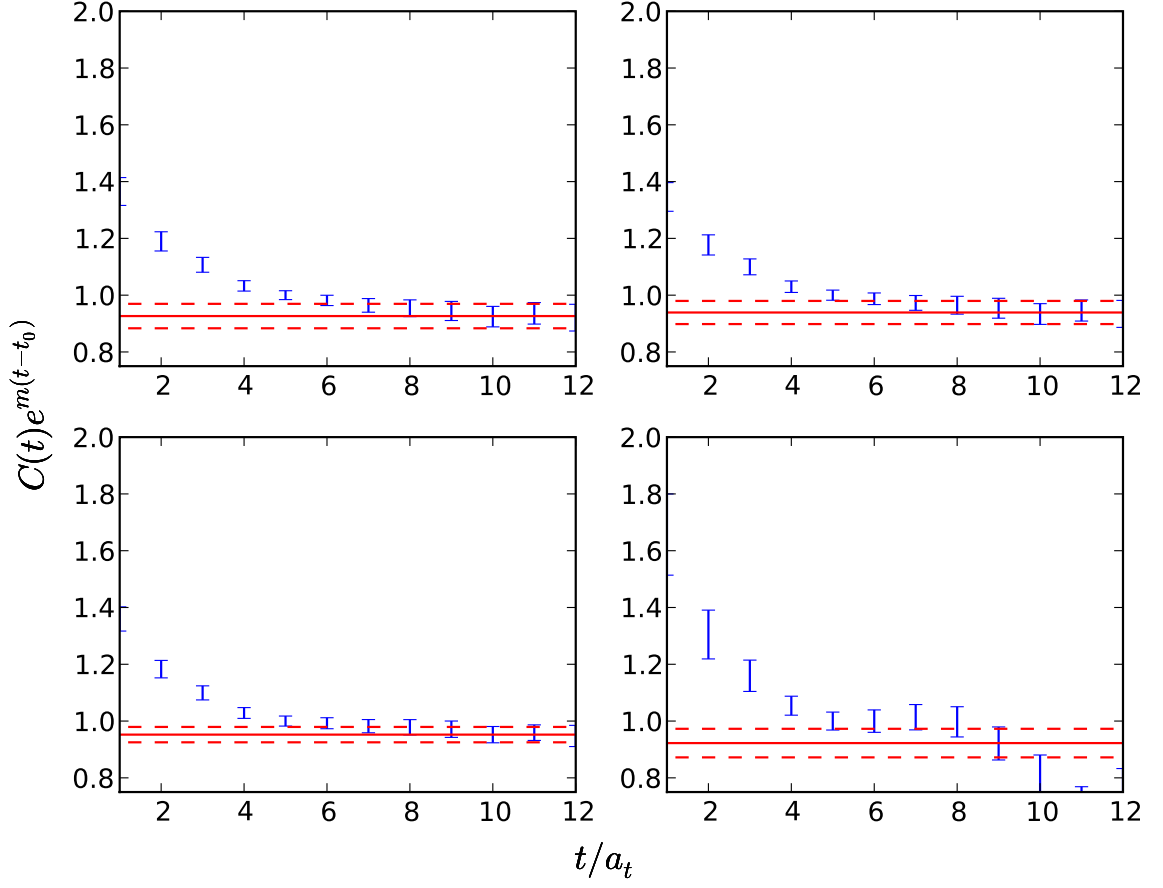


Figure 4.17: From [54], plots of $C_{II}^{\Lambda}(t)e^{E_I^{\Lambda}(t-t_0)}$ for the ground (top left), first excited (top right), second excited (bottom left) and third excited (bottom right) nucleon states in the H_u channel at $m_{\pi} = 578$ MeV. The plot plateaus to the value of A in Eq. (4.75), as determined by the fit, indicated by solid horizontal line. Horizontal dotted lines are jackknife errors on A .

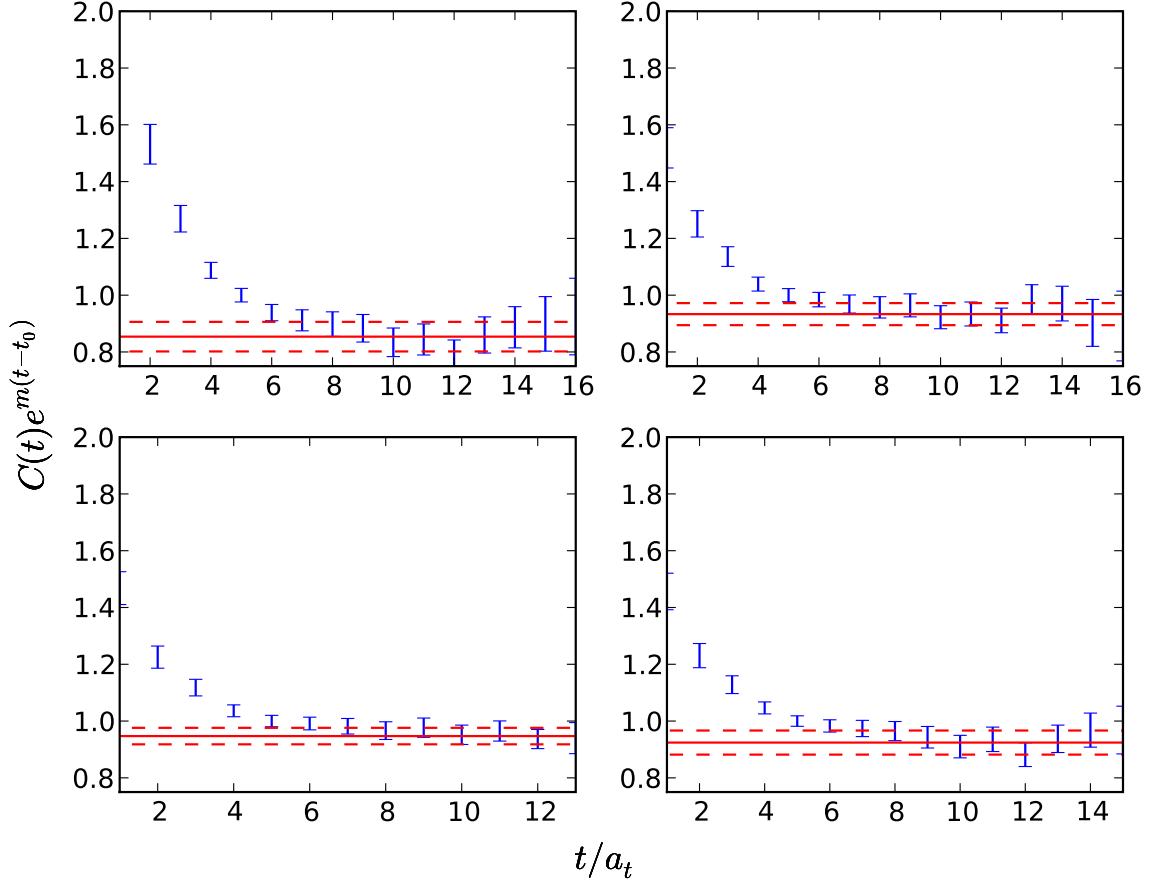


Figure 4.18: From [54], plots of $C_{II}^{\Lambda}(t)e^{E_I^{\Lambda}(t-t_0)}$ for the ground (top left), first excited (top right), second excited (bottom left) and third excited (bottom right) nucleon states in the G_{2g} channel at $m_{\pi} = 578$ MeV. The plot plateaus to the value of A in Eq. (4.75), as determined by the fit, indicated by solid horizontal line. Horizontal dotted lines are jackknife errors on A .

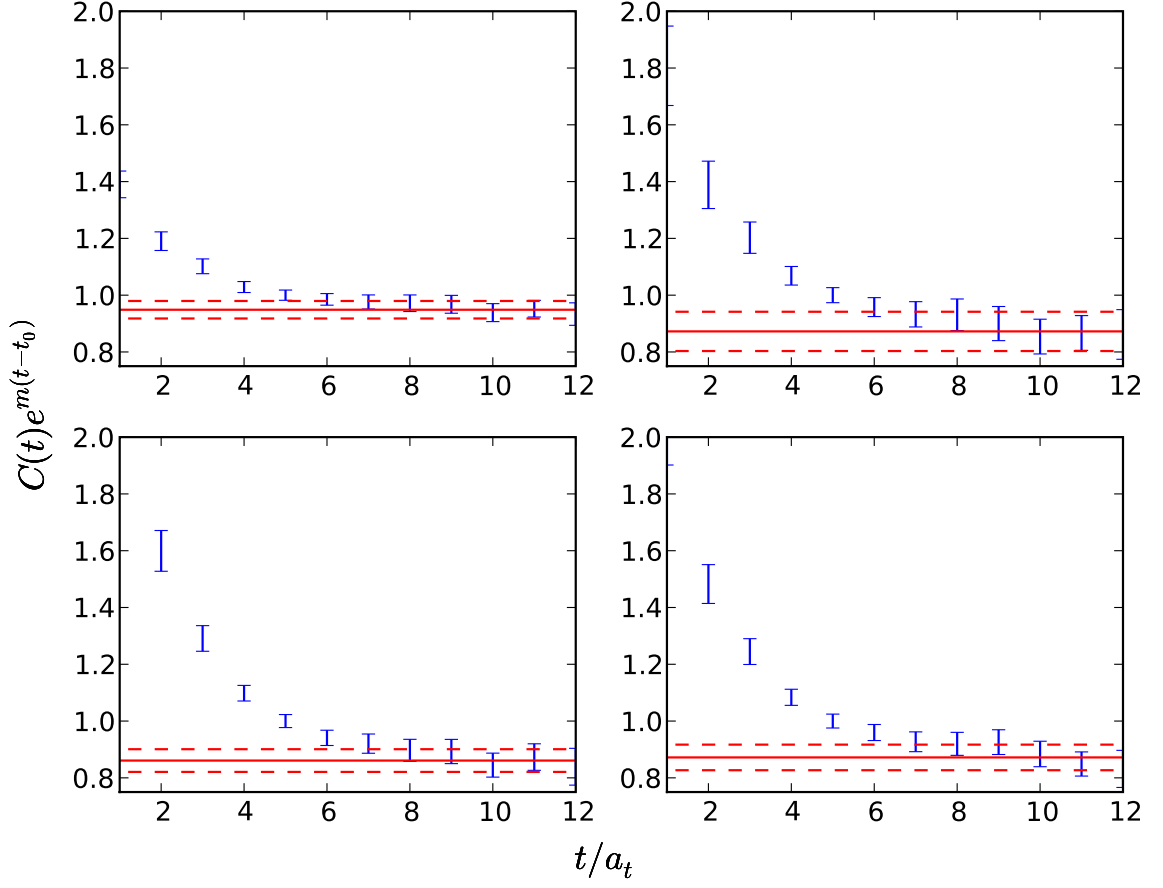


Figure 4.19: From [54], plots of $C_{II}^{\Lambda}(t)e^{E_I^{\Lambda}(t-t_0)}$ for the ground (top left), first excited (top right), second excited (bottom left) and third excited (bottom right) nucleon states in the G_{2u} channel at $m_{\pi} = 578$ MeV. The plot plateaus to the value of A in Eq. (4.75), as determined by the fit, indicated by solid horizontal line. Horizontal dotted lines are jackknife errors on A .

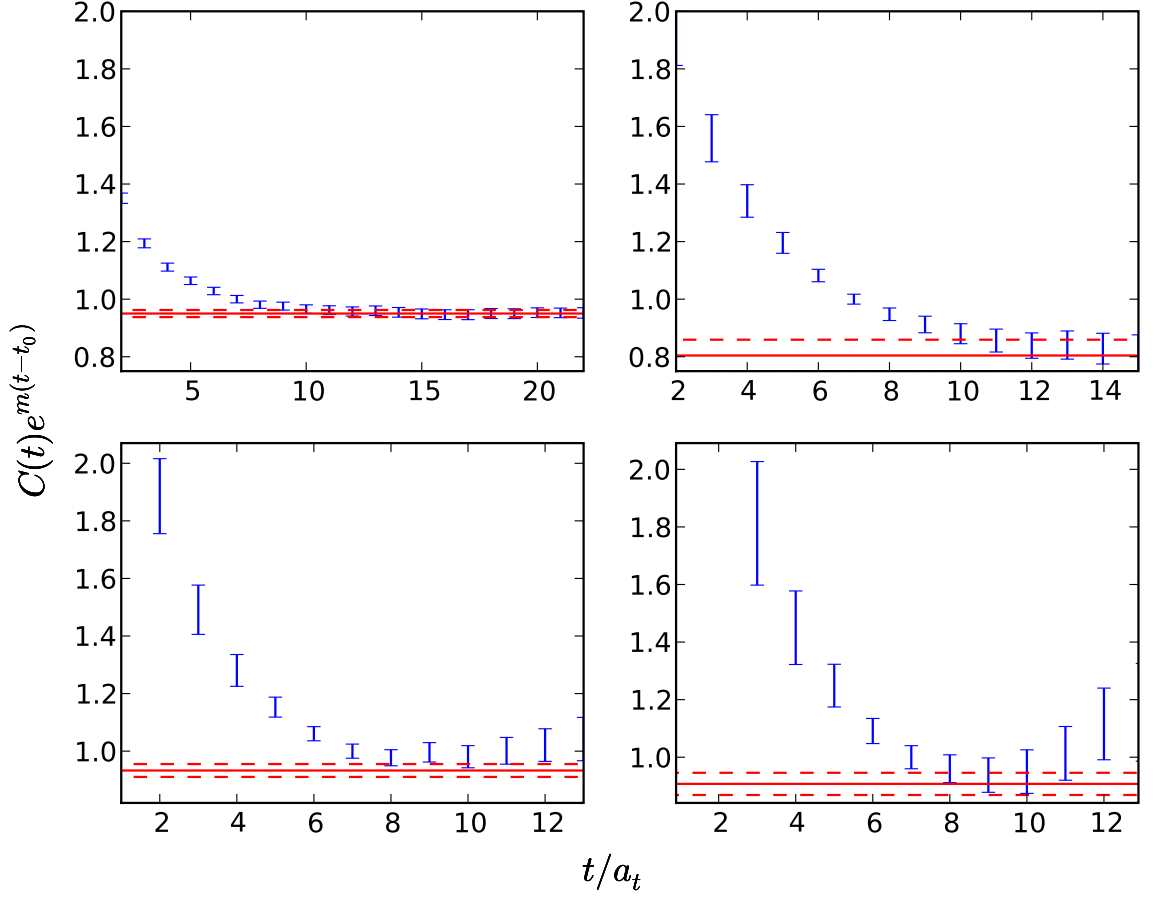


Figure 4.20: From [54], plots of $C_{II}^{\Lambda}(t)e^{E_I^{\Lambda}(t-t_0)}$ for the ground (top left), first excited (top right), second excited (bottom left) and third excited (bottom right) nucleon states in the G_{1g} channel at $m_{\pi} = 416$ MeV. The plot plateaus to the value of A in Eq. (4.75), as determined by the fit, indicated by solid horizontal line. Horizontal dotted lines are jackknife errors on A .

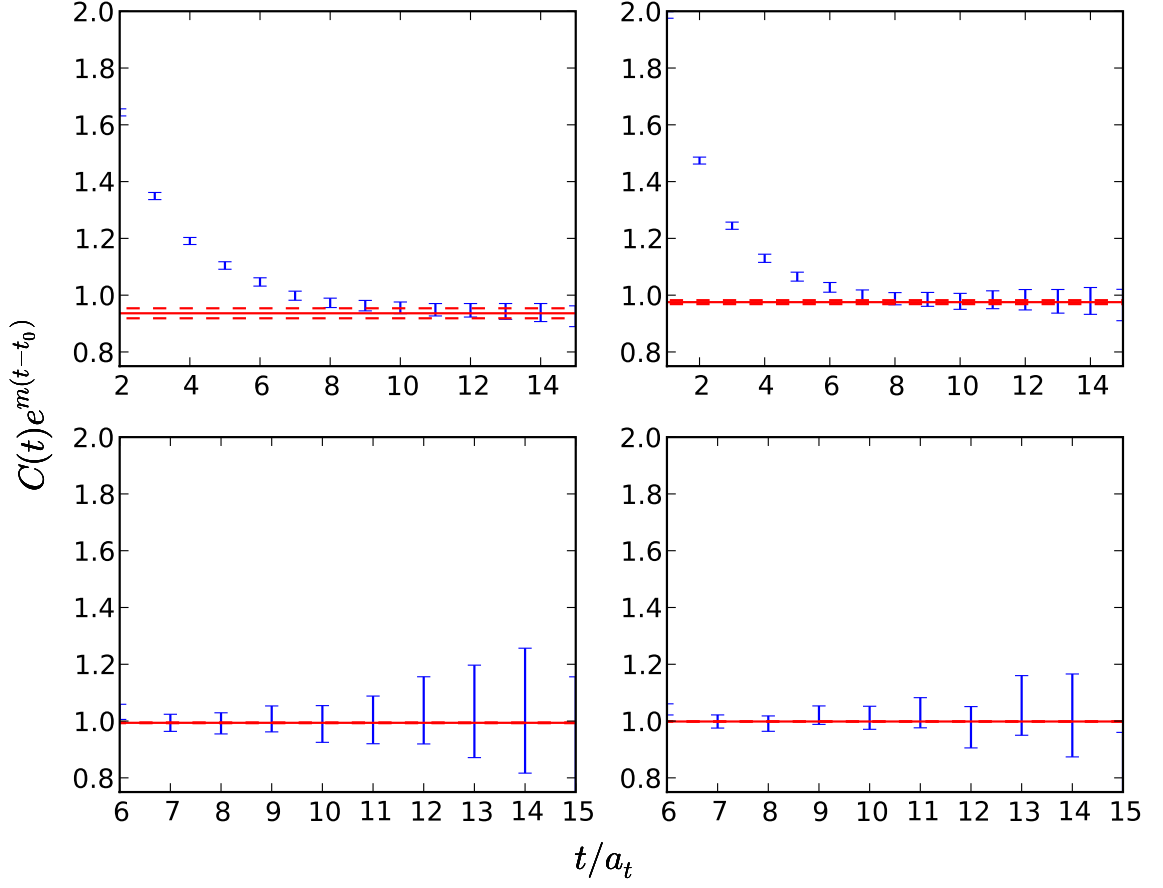


Figure 4.21: From [54], plots of $C_{II}^{\Lambda}(t)e^{E_I^{\Lambda}(t-t_0)}$ for the ground (top left), first excited (top right), second excited (bottom left) and third excited (bottom right) nucleon states in the G_{1u} channel at $m_{\pi} = 416$ MeV. The plot plateaus to the value of A in Eq. (4.75), as determined by the fit, indicated by solid horizontal line. Horizontal dotted lines are jackknife errors on A .

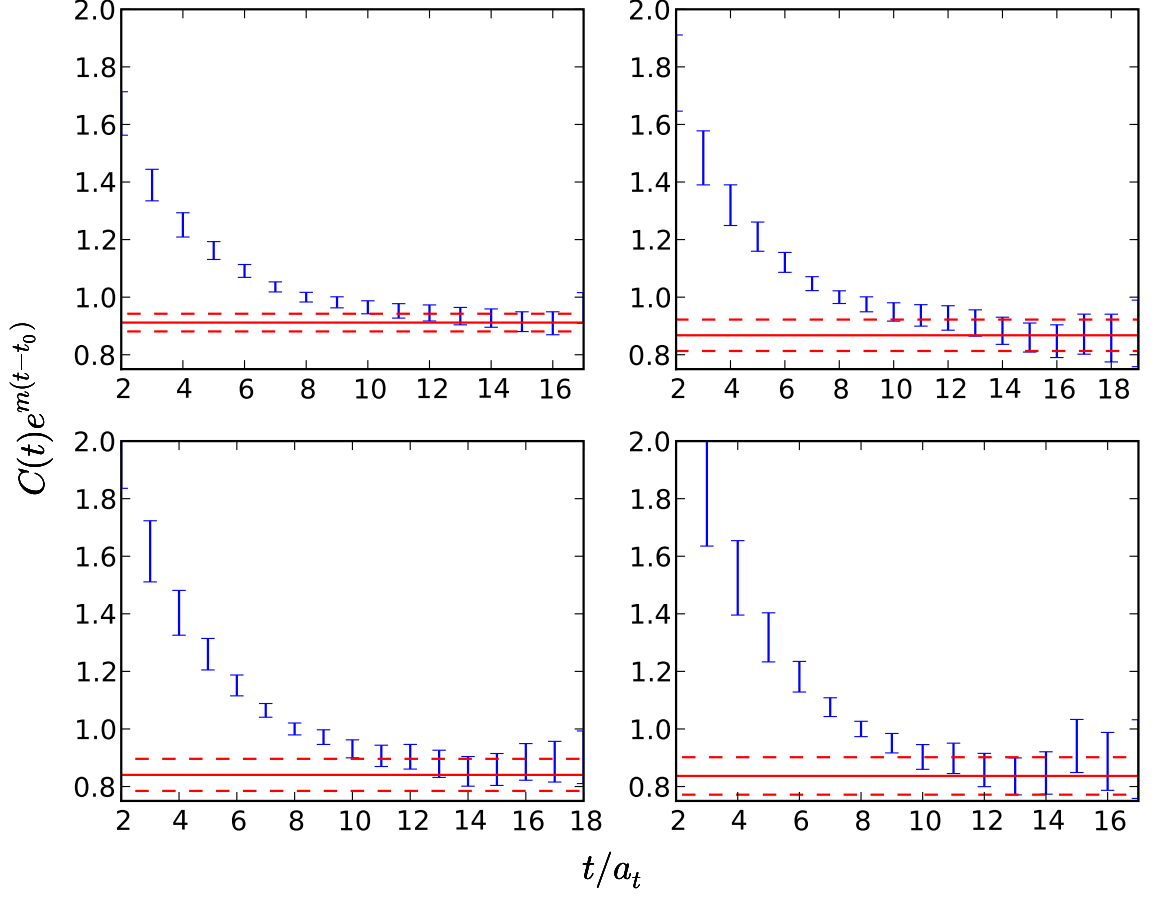


Figure 4.22: From [54], plots of $C_{II}^{\Lambda}(t)e^{E_I^{\Lambda}(t-t_0)}$ for the ground (top left), first excited (top right), second excited (bottom left) and third excited (bottom right) nucleon states in the H_g channel at $m_{\pi} = 416$ MeV. The plot plateaus to the value of A in Eq. (4.75), as determined by the fit, indicated by solid horizontal line. Horizontal dotted lines are jackknife errors on A .

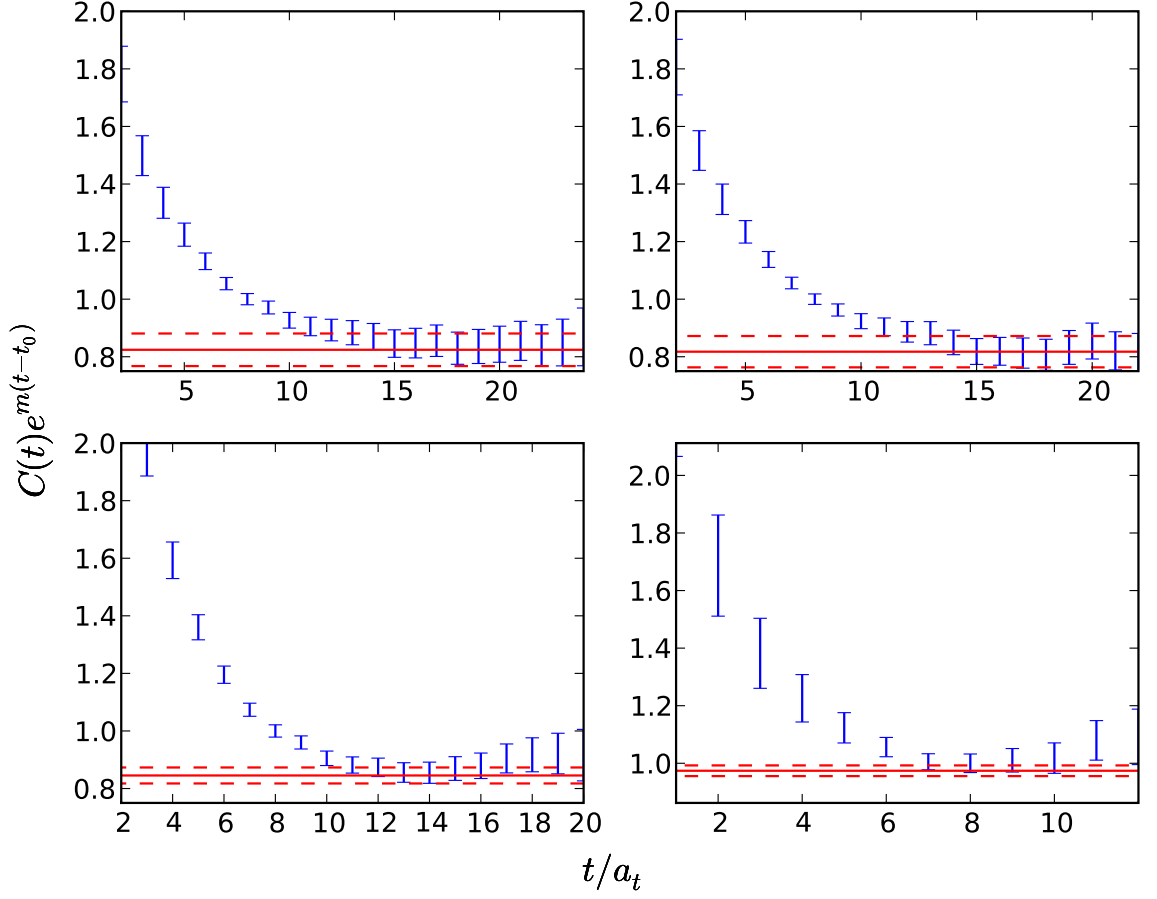


Figure 4.23: From [54], plots of $C_{II}^{\Lambda}(t)e^{E_I^{\Lambda}(t-t_0)}$ for the ground (top left), first excited (top right), second excited (bottom left) and third excited (bottom right) nucleon states in the H_u channel at $m_{\pi} = 416$ MeV. The plot plateaus to the value of A in Eq. (4.75), as determined by the fit, indicated by solid horizontal line. Horizontal dotted lines are jackknife errors on A .

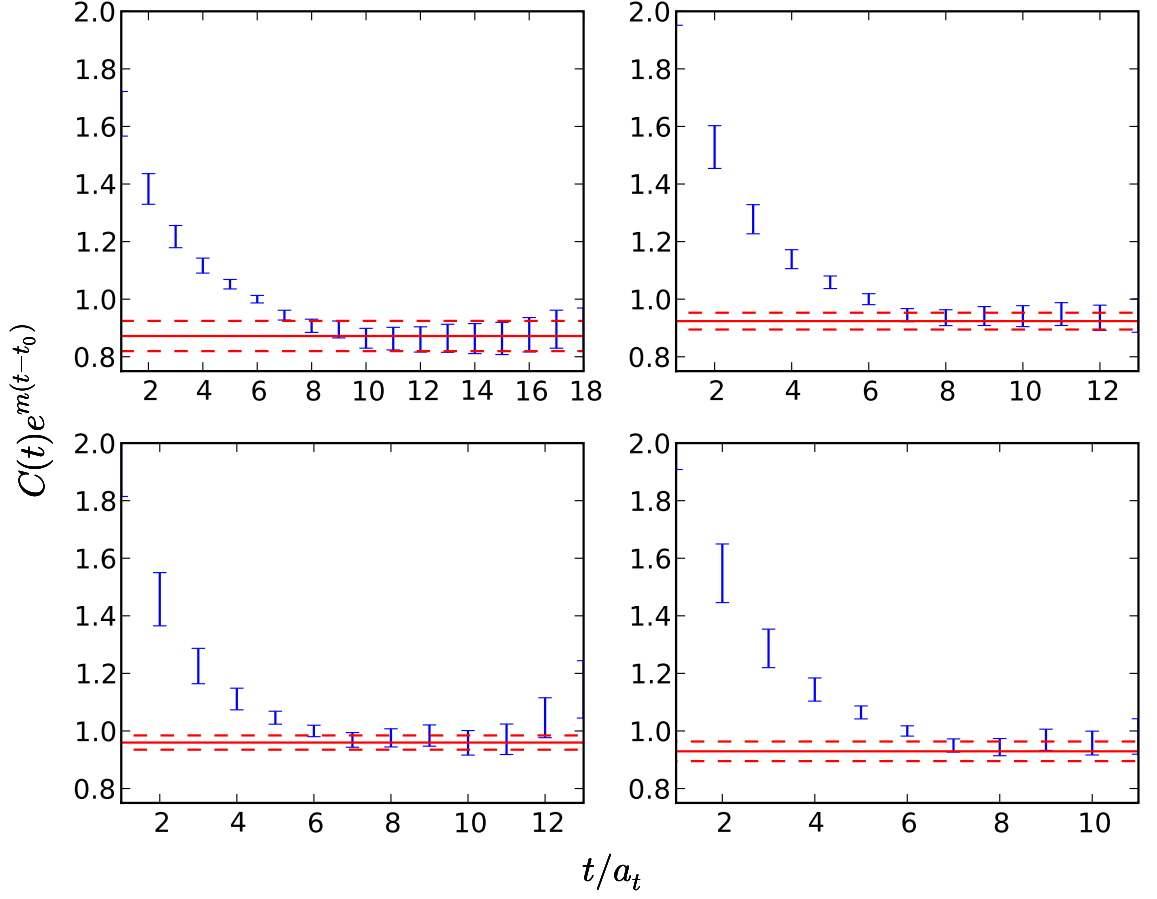


Figure 4.24: From [54], plots of $C_{II}^{\Lambda}(t)e^{E_I^{\Lambda}(t-t_0)}$ for the ground (top left), first excited (top right), second excited (bottom left) and third excited (bottom right) nucleon states in the G_{2g} channel at $m_{\pi} = 416$ MeV. The plot plateaus to the value of A in Eq. (4.75), as determined by the fit, indicated by solid horizontal line. Horizontal dotted lines are jackknife errors on A .

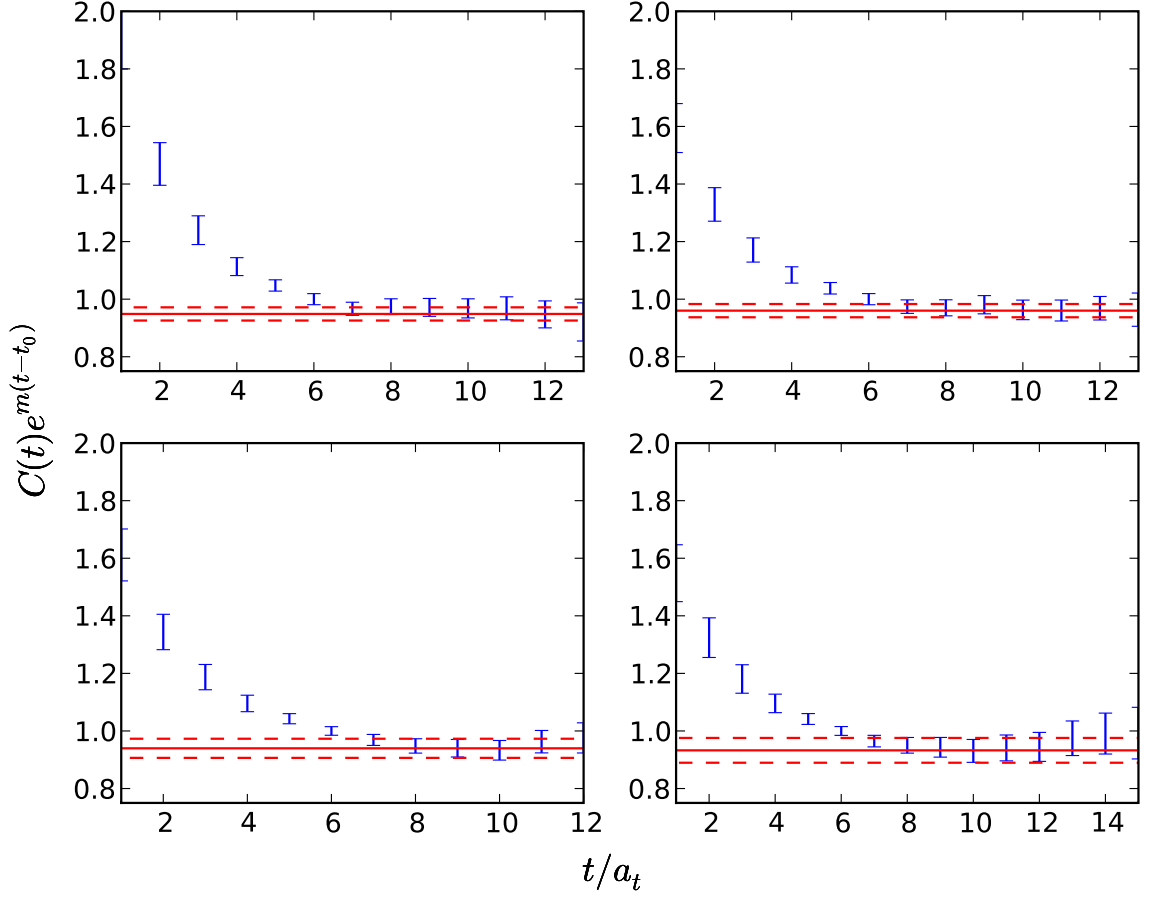


Figure 4.25: From [54], plots of $C_{II}^\Lambda(t)e^{E_I^\Lambda(t-t_0)}$ for the ground (top left), first excited (top right), second excited (bottom left) and third excited (bottom right) nucleon states in the G_{2u} channel at $m_\pi = 416$ MeV. The plot plateaus to the value of A in Eq. (4.75), as determined by the fit, indicated by solid horizontal line. Horizontal dotted lines are jackknife errors on A .

parity and zero angular momentum. The two particle state, must therefore have parity $-p$ and angular momentum J . On the lattice, we expect the two particle state consisting of the ground state nucleon in irrep Λ and a pion, with particles at rest, to show up in the opposite parity channel $-\Lambda$. To be more precise, in terms of the lattice irreps, the pion state transforms as the A_{1u} irrep. The direct product of the A_{1u} irrep with any lattice irrep Λ reduces to the opposite parity irrep $-\Lambda$. A similar reduction of direct products of lattice states with non-zero momentum can be done using the tables in [68].

In Figs. 4.26 and 4.27, we show the energy spectrum for both ensembles with the multi-particle thresholds for each channel.

4.10.2 Discussion

For some of the extracted states, we are able to identify the corresponding continuum states. The G_{1g} ground state we identify with the continuum proton/neutron. Extrapolating the mass using the form $M = a + bm_\pi^2$, we get a continuum mass of 917(27) MeV.

There are several conclusions we can draw for the negative parity spectrum. There are two G_{1u} states with energies approximately 1.5 and 1.6 times the G_{1g} ground state energy with the next state much higher. This pattern is similar to the physical spectrum, where the two lowest $\frac{1}{2}^-$ resonances occur at 1535 MeV and 1650 MeV with the third well above them at 2090 MeV. These states are all above the multi-particle threshold for that channel. Since our operator set did not contain

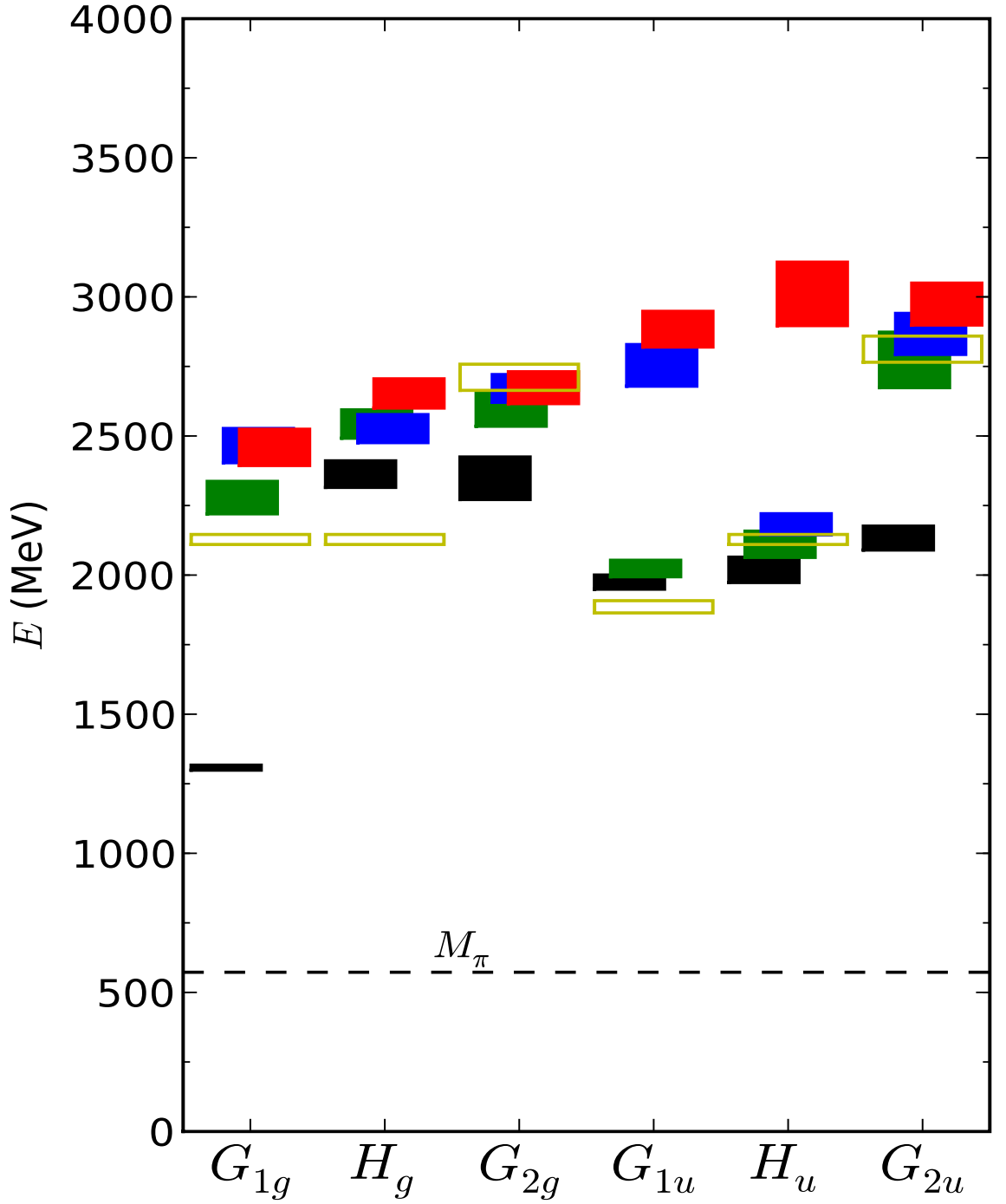


Figure 4.26: From [54], the nucleon spectrum at $m_\pi = 578$ MeV. We plot the lowest four extracted energy levels in each channel. The location of each box indicates the energy, while the height is the jackknife error. The empty box in each channel is an estimate of the lowest multi-particle state in each channel.

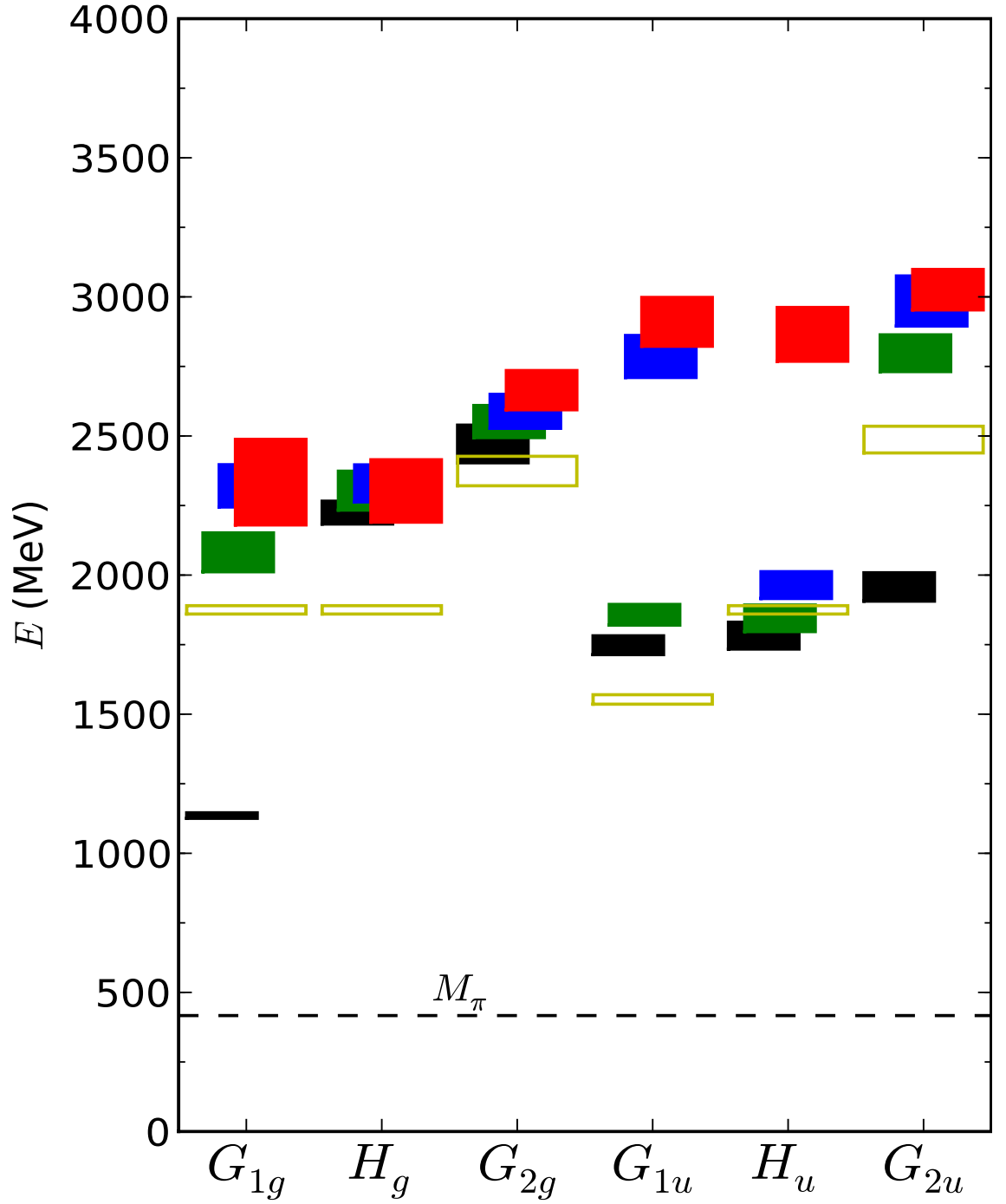


Figure 4.27: From [54], the nucleon spectrum at $m_\pi = 416$ MeV. We plot the lowest four extracted energy levels in each channel. The location of each box indicates the energy, while the height is the jackknife error. The empty box in each channel is an estimate of the lowest multi-particle state in each channel.

multi-hadron operators, we expect the coupling to multi-particle states to be low, suggesting that the lowest G_{1u} state is, in fact, the $N^*(1535)$. However, further study is needed to conclusively identify the multi-particle states.

In the H_u channel, the ground state energy is isolated, indicating a continuum $\frac{3}{2}^-$ state. The lowest such physical state is the $N(1520)$ resonance. In the G_{2u} channel at both pion masses, the ground state is degenerate with an H_u state with no corresponding state in the G_{1u} channel. This is indicative of a $\frac{5}{2}^-$ state. A previous work [29] also showed evidence for a spin $\frac{5}{2}^-$ state, but a nearby G_{1u} state made it difficult to distinguish between the case where there is a spin $\frac{5}{2}^-$ state degenerate with a spin $\frac{1}{2}^-$ state and the case where there is a single a $\frac{7}{2}^-$ state. This work shows the clear evidence for a spin- $\frac{5}{2}^-$ state. In the continuum this corresponds to the $N(1675)$.

The first excited G_{1g} state is at approximately twice the mass of the lowest G_{1g} state and is above the lowest G_{1u} state. This does differ from the physical spectrum, in which the first excited positive parity state is below the negative parity ground state. Whether the energy of first excited G_{1g} state will decrease toward the Roper state at lower values of the pion mass remains an open question.

Chapter 5

Distillation

In the nucleon spectrum computation, many of the extracted energies were higher than the multi-particle thresholds. Our interpretation of the spectrum is hindered by our inability to identify which states consist of multiple hadrons. In the future, we would like to include multi-hadron operators in the variational basis to aid in the identification of these multi-particle states. However, correlators between multi-hadron operators cannot be computed using the point-to-all method because quark-antiquark pair creation and annihilation can occur at any point on the lattice. Instead, all-to-all propagators are necessary. Typically, stochastic techniques have been employed to estimate the all-to-all propagator as an exact calculation would be prohibitively expensive. We describe a new method in this chapter in which instead of smearing our operators, we project them onto the space spanned by a small number of low-lying eigenmodes of the Laplacian operator. These projected, or “distilled” operators have a rank small enough that an exact all-to-all propagator calculation is possible.

In Section 5.1 we describe all-to-all propagators and why they are necessary for excited spectrum calculations. We briefly describe the stochastic methods typically used to estimate the all-to-all propagator. We introduce the distillation method in Section 5.2 and describe how we can use it to extract the excited state spectrum.

Finally, in Section 5.3 we show the results of tests of the method in the calculation of excited baryon spectra.

5.1 All-to-all Propagators

In the nucleon spectrum study, we used point-to-all propagators in which source operators were constrained to a single point on the lattice, while the location of the sink operator was varied to all points on the lattice. Using symmetries of the lattice we were able to calculate correlation functions for all the operators discussed in Chapter 3 using point-to-all propagators on only four different source points. A wide range of calculations in lattice QCD can be performed using point-to-all techniques, in which the quark matrix is inverted on a small number of sources.

The all-to-all propagator is the propagator from any source point on the lattice to any sink, effectively the set of point-to-all propagators for all source points. While this is prohibitively expensive to calculate for all but the smallest sized lattices, there exist stochastic techniques [69, 70, 71, 72] for estimating the matrix elements of the all-to-all propagator. All-to-all propagators provide a way to solve a number of problems which are impossible with point-to-all propagators.

Correlation functions may have contributions from “connected” Feynman diagrams in which all quark lines are connected to the sources and sinks through other quarks lines and “disconnected” Feynman diagrams in which there exist quark lines which are connected to the sources and sinks only through gluons. These diagrams may occur in flavorless mesons, in which the quark and antiquark of the meson can

annihilate at the source into gluons, which then propagate to the sink and reform into the meson state. We give an example of a connected and disconnected Feynman diagram for such a meson in Fig. 5.1.

To calculate the disconnected contribution to the correlation function, we generally need all-to-all propagators. Each quark line in the Feynman diagrams represents a propagator. For the connected diagram in Fig. 5.1, all the quark lines flow from source to sink and thus can be calculated from point-to-all propagators. In the disconnected diagram, we have a quark line flowing from the sink to the sink. To calculate the correlation function, we need to calculate the single quark propagators $\tilde{S}_{a\alpha;\bar{a}\bar{\alpha}}^A(x;x)$ for all points x on the lattice. This requires the calculation of the point-to-all propagator for all source points, or the all-to-all propagator. In many cases, the disconnected contribution is zero due to cancellations among the different terms of the flavor wave function.¹ For example, in the case of the π^0 , the flavor wave function, $\frac{1}{\sqrt{2}}(u\bar{u} - d\bar{d})$, causes the disconnected part stemming from the $u\bar{u}$ to cancel the part stemming from the $d\bar{d}$. All flavor octet states have this property in which the disconnected part is zero. Flavor singlets, such as the η' have significant disconnected contributions and thus correlators between flavor singlets require the all-to-all propagator.

The all-to-all propagator is of particular interest to spectroscopy because it is needed to calculate correlation functions between multi-hadron operators. As an example, the lightest multi-hadron state in the baryon spectrum would consist of a pion and a nucleon. The pion consists of a light quark and a light antiquark

¹Assuming degenerate light quarks.

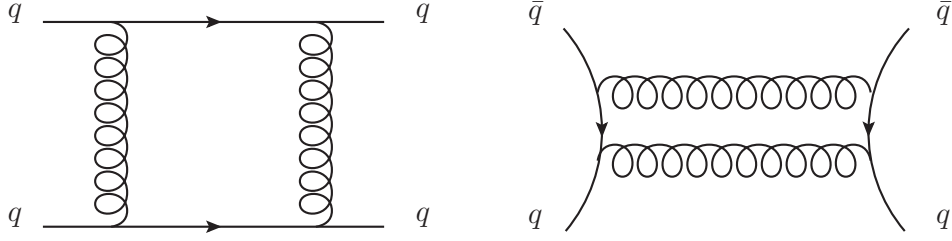


Figure 5.1: Feynman diagrams for connected (left) and disconnected (right) contributions to flavorless meson propagators.

while the nucleon has three light quarks. The antiquark in the pion could, along with one of the quarks in the nucleon, annihilate into gluons, which reform into the quark-antiquark pair at the sink. This disconnected piece of the correlation function requires the all-to-all propagator.

5.1.1 Stochastic All-to-All Propagators

The all-to-all propagator is typically estimated using stochastic methods. We start with a set of N vectors $\phi_{a\alpha}^i(x)$, $i = 1 \dots N$, whose elements are selected randomly in such a way that

$$\langle \phi_{a\alpha}^i(y) \phi_{\bar{a}\bar{\alpha}}^{i*}(x) \rangle = \sum_{i=1}^N \phi_{a\alpha}^i(y) \phi_{\bar{a}\bar{\alpha}}^{i*}(x), \quad (5.1)$$

$$\stackrel{N \rightarrow \infty}{=} \delta(y, x) \delta_{a\alpha; \bar{a}\bar{\alpha}}. \quad (5.2)$$

For large but finite N , the expectation value $\langle \phi_{a\alpha}^i(y) \phi_{\bar{a}\bar{\alpha}}^{i*}(x) \rangle$ approximates a delta-function with errors of the order $1/\sqrt{N}$. We use this approximation to obtain the

all-to-all propagator in a single configuration:

$$S_{a\alpha;\bar{a}\bar{\alpha}}^A(y, x, U) \approx S_{a\alpha;\bar{b}\bar{\beta}}^A(y, z) \sum_{i=1}^N \phi_{\bar{b}\bar{\beta}}^i(z) \phi_{\bar{a}\bar{\alpha}}^{i*}(x), \quad (5.3)$$

$$= \sum_{i=1}^N \eta_{a\alpha}^i(y) \phi_{\bar{a}\bar{\alpha}}^{i*}(x), \quad (5.4)$$

$$\eta_{a\alpha}^i(y) = S_{a\alpha;\bar{b}\bar{\beta}}^A(y, z, U) \phi_{\bar{b}\bar{\beta}}^i(z). \quad (5.5)$$

We obtain the η^i by solving the equation

$$K_{\bar{b}\bar{\beta};a\alpha}^A(z, y, U) \eta_{a\alpha}^i(y) = \phi_{\bar{b}\bar{\beta}}^i(z), \quad (5.6)$$

inverting the quark matrix on the random source vectors. One choice of the random vectors is Z_n noise, in which each component of the vectors is chosen randomly from the set of the n^{th} complex roots of 1. Although a number of variance reduction techniques exist [73, 74, 72], the stochastic estimation always introduces an additional statistical uncertainty into the calculation.

5.2 Distillation: Exact All-to-All Propagators

A new method for the calculation of exact all-to-all propagators, called distillation, has recently been developed and tested [75]. We consider the all-to-all propagator from a smeared source to a smeared sink. The purpose of the smearing is to reduce the coupling of the quark operator to high energy modes. Gaussian smearing does this by suppressing the higher eigenmodes of the Laplacian operator. This can also be accomplished by computing the lowest N eigenmodes of the Laplacian and projecting the field operators into the space spanned by those eigenmodes,

creating “distilled” operators of rank N . The size of N required for a spectrum calculation depends on the size of the lattice, but is typically ~ 50 , small enough that we can calculate exact all-to-all propagators between distilled operators.

In terms of the eigenvalues $\lambda_p(t)$ and eigenvectors $v_{a,p}(\vec{x}, t)$ (a is the color index and p labels eigenmodes) of the Laplacian operator, we rewrite the smearing matrix as

$$J_{ab}(\vec{x}, \vec{y}, t) = \sum_p f(\lambda_p(t)) v_{a,p}(\vec{x}, t) v_{b,p}^\dagger(\vec{y}, t), \quad (5.7)$$

where $f(\lambda_p(t))$ is a weighting function which determines the relative contributions of the eigenmodes to the operator. For $f(\lambda_p(t)) = e^{\sigma^2 \lambda_p(t)^2/2}$, we have Gaussian smearing. The smeared quark propagator for an undisplaced source is then²

$$\tilde{S}_{a\alpha; \bar{a}\bar{\alpha}}^A(y, x) = J_{ab}(\vec{y}, \vec{z}, t_f) S_{b\alpha; \bar{b}\bar{\alpha}}^A(\vec{z}, t_f; \vec{w}, t_i) J_{\bar{b}\bar{\alpha}}^*(\vec{w}, \vec{x}, t_i), \quad (5.8)$$

$$\begin{aligned} &= \sum_p \sum_{\bar{p}} f(\lambda_p(t_f)) v_{a,p}(\vec{y}, t_f) v_{b,p}^\dagger(\vec{z}, t_f) S_{b\alpha; \bar{b}\bar{\alpha}}^A(\vec{z}, t_f; \vec{w}, t_i) \\ &\times f(\lambda_{\bar{p}}(t_i)) v_{\bar{b}, \bar{p}}(\vec{w}, t_i) v_{\bar{a}, \bar{p}}^\dagger(\vec{x}, t_i), \end{aligned} \quad (5.9)$$

$$= \sum_p \sum_{\bar{p}} f(\lambda_p(t_f)) v_{a,p}(\vec{y}, t_f) P_{\alpha\bar{\alpha}}^{p\bar{p}}(t_f, t_i) f(\lambda_{\bar{p}}(t_i)) v_{\bar{a}, \bar{p}}^\dagger(\vec{x}, t_i), \quad (5.10)$$

where $P_{\alpha\bar{\alpha}}^{p\bar{p}}(t_f, t_i)$, called a perambulator, is

$$P_{\alpha\bar{\alpha}}^{p\bar{p}}(t_f, t_i) = v_{b,p}^\dagger(\vec{z}, t_f) S_{b\alpha; \bar{b}\bar{\alpha}}^A(\vec{z}, t_f; \vec{w}, t_i) v_{\bar{b}, \bar{p}}(\vec{w}, t_i). \quad (5.11)$$

For displaced sources and sinks, the quark propagator is

$$\tilde{S}_{a\alpha; \bar{a}\bar{\alpha}}^A(y, x) = \sum_p \sum_{\bar{p}} f(\lambda_p(t_f)) \left[\tilde{D}_i^{(\ell)} v_{a,p} \right] (\vec{y}, t_f) P_{\alpha\bar{\alpha}}^{p\bar{p}}(t_f, t_i) f(\lambda_{\bar{p}}(t_i)) \left[v_{\bar{a}, \bar{p}}^\dagger \tilde{D}_i^{(\ell)\dagger} \right] (\vec{x}, t_i), \quad (5.12)$$

²For the rest of this section, there will be no implied summation over repeated temporal variables.

where the displacement operator is applied to the Laplacian eigenvectors outside of the perambulator. For the weighting function we use a Heaviside approximation to Gaussian smearing: $f(\lambda_p(t)) = \Theta(\lambda_p(t) - \lambda_{max})$, effectively truncating the sum over eigenmodes at some maximal eigenvalue and using equal weighting for all included modes.

We now expand this concept to three-quark baryon operators. When we began using the distillation method, we also developed a new set of projection coefficients into the lattice irreps. The new set was optimized so that operators contained a fewer number of terms (speeding up the correlator evaluation) and the isospin projection was included in the coefficients. For the delta operators, the new coefficients were for the $I_3 = \frac{1}{2} \Delta^+$ operator, whose flavor wave function consists of permutations of uud operators. The flavors of the quarks for each term in the operators were then identical to those in the nucleon operators. By convention, the quarks were always reordered so that the third quark was the down flavored quark. This eased the development of the code since the Wick contractions for all terms in both sets of operators were then identical.

With these new coefficients, the nucleon and delta correlation functions are

$$C_{IJ}^{F,\Lambda}(t) = c_{I;\alpha\beta\gamma}^{F,\Lambda} \bar{c}_{J;\bar{\alpha}\bar{\beta}\bar{\gamma}}^{F,\Lambda} \left(\tilde{G}_{\alpha\beta\gamma;\bar{\alpha}\bar{\beta}\bar{\gamma}}^{uud}(t_f, t_i) - \tilde{G}_{\alpha\beta\gamma;\bar{\beta}\bar{\alpha}\bar{\gamma}}^{uud}(t_f, t_i) \right), \quad (5.13)$$

$$\begin{aligned} &= c_{I;\alpha\beta\gamma}^{F,\Lambda} \bar{c}_{J;\bar{\alpha}\bar{\beta}\bar{\gamma}}^{F,\Lambda} \epsilon_{abc} \epsilon_{\bar{a}\bar{b}\bar{c}} \left(\tilde{S}_{a\alpha;\bar{a}\bar{\alpha}}^u(t_f, t_i) \tilde{S}_{b\beta;\bar{b}\bar{\beta}}^u(t_f, t_i) \tilde{S}_{c\gamma;\bar{c}\bar{\gamma}}^d(t_f, t_i) \right. \\ &\quad \left. - \tilde{S}_{a\alpha;\bar{b}\bar{\beta}}^u(t_f, t_i) \tilde{S}_{b\beta;\bar{a}\bar{\alpha}}^u(t_f, t_i) \tilde{S}_{c\gamma;\bar{c}\bar{\gamma}}^d(t_f, t_i) \right), \end{aligned} \quad (5.14)$$

$$\begin{aligned} &= \sum_{p,q,r} \sum_{\bar{p},\bar{q},\bar{r}} \Phi_{I;pqr;\alpha\beta\gamma}^{F,\Lambda}(t_f) \left(P_{\alpha\bar{\alpha}}^{p\bar{p}}(t_f, t_i) P_{\beta\bar{\beta}}^{q\bar{q}}(t_f, t_i) P_{\gamma\bar{\gamma}}^{r\bar{r}}(t_f, t_i) \right. \\ &\quad \left. - P_{\alpha\bar{\beta}}^{p\bar{p}}(t_f, t_i) P_{\beta\bar{\alpha}}^{q\bar{q}}(t_f, t_i) P_{\gamma\bar{\gamma}}^{r\bar{r}}(t_f, t_i) \right) \bar{\Phi}_{J;\bar{p}\bar{q}\bar{r};\bar{\alpha}\bar{\beta}\bar{\gamma}}^{F,\Lambda}(t_i), \end{aligned} \quad (5.15)$$

where

$$\Phi_{I;pqr;\alpha\beta\gamma}^{F,\Lambda}(t) = \epsilon_{abc} c_{I;\alpha\beta\gamma}^{F,\Lambda} \left[\tilde{D}_i^{(\ell)} v_{a,p} \right] (t_f) \left[\tilde{D}_j^{(\ell)} v_{b,q} \right] (t_f) \left[\tilde{D}_k^{(\ell)} v_{c,r} \right] (t_f), \quad (5.16)$$

$$\bar{\Phi}_{J;\bar{p}\bar{q}\bar{r};\bar{\alpha}\bar{\beta}\bar{\gamma}}^{F,\Lambda}(t_i) = \epsilon_{\bar{a}\bar{b}\bar{c}} \bar{c}_{J;\bar{\alpha}\bar{\beta}\bar{\gamma}}^{F,\Lambda} \left[v_{\bar{a}\bar{p}}^\dagger \tilde{D}_i^{(\ell)\dagger} \right] (t_i) \left[v_{\bar{b}\bar{q}}^\dagger \tilde{D}_j^{(\ell)\dagger} \right] (t_i) \left[v_{\bar{c}\bar{r}}^\dagger \tilde{D}_k^{(\ell)\dagger} \right] (t_i), \quad (5.17)$$

are distilled baryon creation and annihilation operators.

To do a spectroscopy calculation, we first calculate the eigenvectors of the Laplacian operator on each time step in each configuration. This was done using the Arpack eigenvalue solver [76]. The perambulators and operators are then formed from Eqs. (5.11), (5.16), and (5.17). The correlator is calculated by tying together the perambulators and operators according to Eq. (5.15). The perambulators are independent of the sources. The same perambulators can be used for meson, baryon, and multi-particle correlation functions. Likewise the meson and baryon distilled operators can be reused to calculate multi-particle correlation functions; the only change is that the multi-particle correlator ties the elements together differently.

5.3 Distillation Tests

Anisotropic lattices with $2 + 1$ flavors of dynamical quarks were used to test the distillation method [75]. The anisotropy was tuned to $a_S/a_t = 3.5$ and two different volumes were used: $16^3 \times 128$ and $20^3 \times 128$. These same lattices were used for the delta spectrum study and are described in more detail in the next chapter.

In particular, it was important to determine how many eigenvectors we needed for a spectroscopy calculation and how this scaled with the lattice volume. It was believed that using the same cutoff λ_{max} to truncate the eigenmodes would produce results independent of volume (assuming negligible finite volume effects). It was found that the number of eigenmodes less than λ_{max} scaled like $L_s^{3/2}$, as shown in Fig. 5.2. Thus, the number of eigenvectors needed for a spectroscopy calculation was also expected to scale like $L_s^{3/2}$.

In Fig. 5.3 we plot the effective energies of four G_{1g} nucleon operators on the $16^3 \times 128$ lattices, calculated from

$$E_{eff} = \frac{1}{5} \ln \left(\frac{C(t)}{C(t+5)} \right), \quad (5.18)$$

as to average over timeslices separated by 5 steps. We plot the results for several different numbers of eigenvectors. An improvement in the statistical error is seen by increasing from 16 to 32 eigenvectors. In moving from 32 to 64 eigenvectors, little improvement is seen. In fact the effective energies seem to plateau slightly later and the operators seem to be oversmeared with 64 eigenvectors, as compared to 32. As seen in Fig. 5.4, little improvement is seen when more than 32 eigenvectors are used in the calculation of the first two energy levels through a variational analysis.

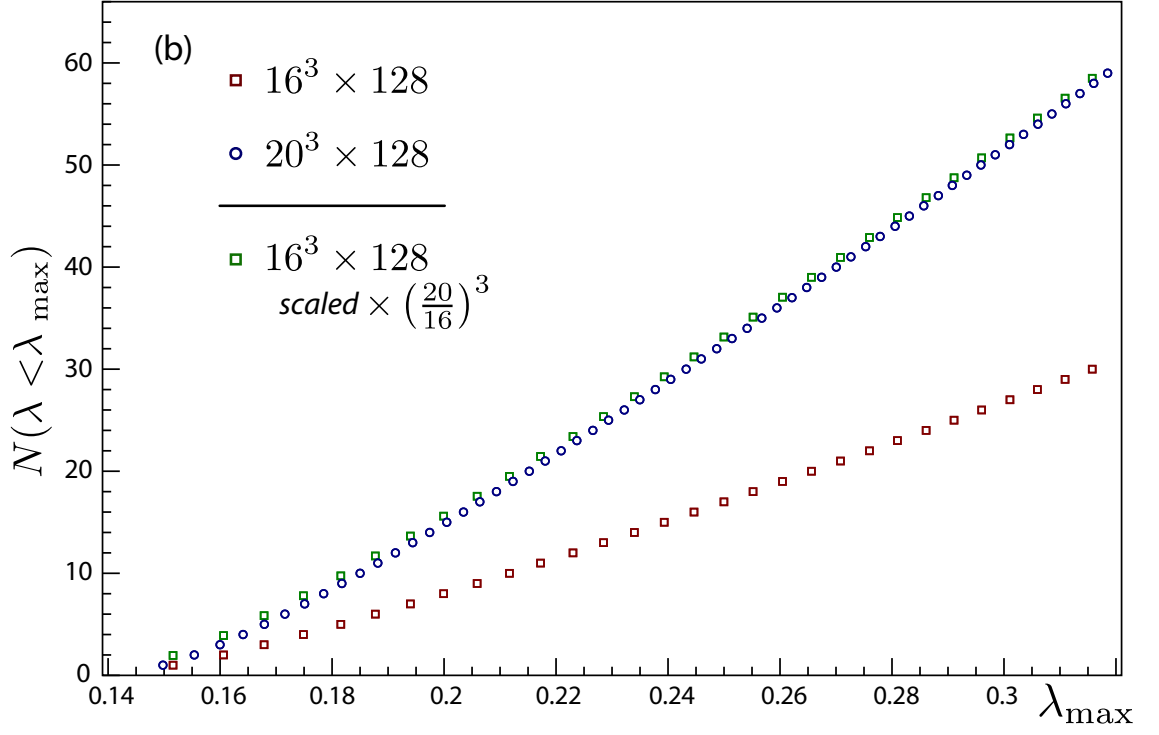


Figure 5.2: From [75], the number of eigenvalues of the Laplacian operator less than λ_{\max} for $16^3 \times 128$ and $20^3 \times 128$ lattices. Also shown are the $16^3 \times 128$ results scaled by a factor of $\left(\frac{20}{16}\right)^{3/2}$.

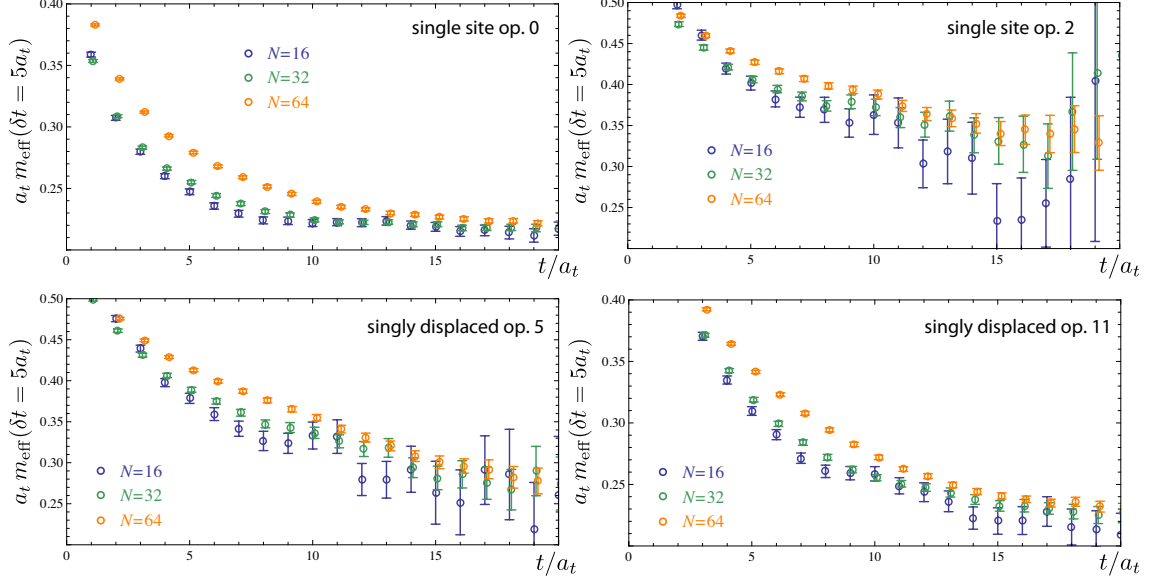


Figure 5.3: From [75], effective mass plots for two single-site and two singly displaced G_{1g} nucleon operators on $16^3 \times 128$ lattices calculated with different number of eigenvectors.

Finally, the volume effects on the effective mass were examined. When increasing the volume from 16^3 to 20^3 , it was expected that the number of eigenvectors would have to be doubled since $\left(\frac{20}{16}\right)^{3/2} \approx 2$. As shown in Fig. 5.5, 64 eigenvectors were required on the 20^3 lattices to obtain similar results to those on the 16^3 lattices with 32 eigenvectors.

The time to calculate baryon correlators, with three quarks at the source and three quarks at the sink, scales like N^6 , as seen in Eq. (5.15). As N scales like $L_s^{3/2}$, the computational time scales poorly with volume. Methods with better scaling are currently being investigated. However, calculating baryon correlators using the distillation method was feasible on the $16^3 \times 128$ lattices using 32 eigenvectors and we used this method to extract the delta spectrum on those lattices. This calculation

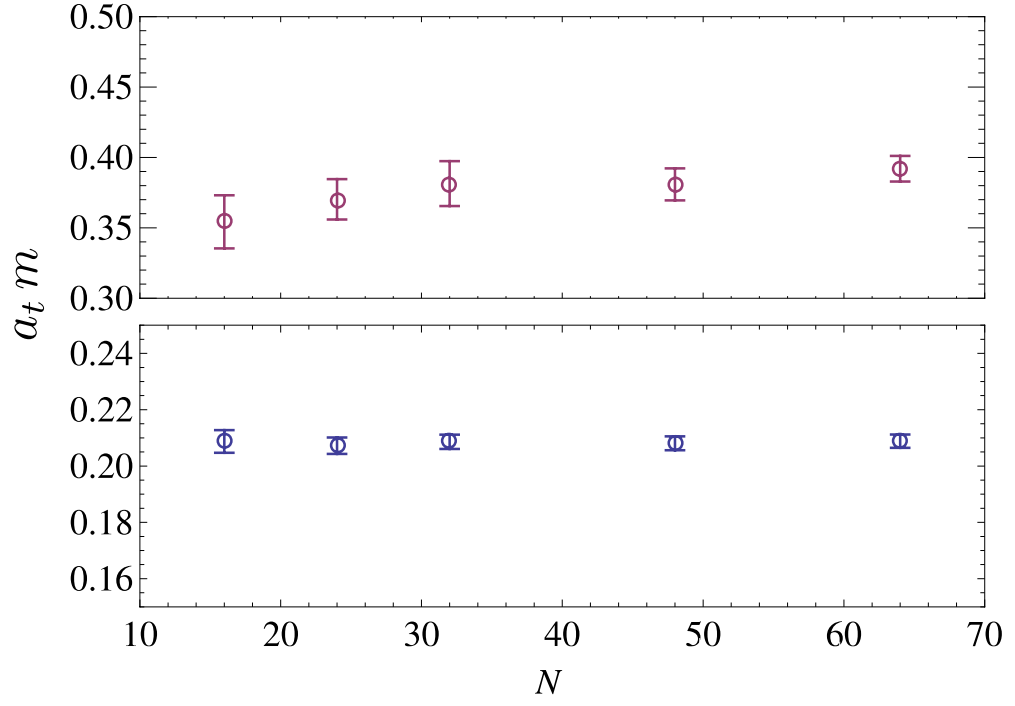


Figure 5.4: From [75], fitted energies of the ground (bottom) and first excited (top) states from a G_{1g} nucleon variational calculation. Energies are plotted as a function of the number of eigenvectors N used in the calculation.

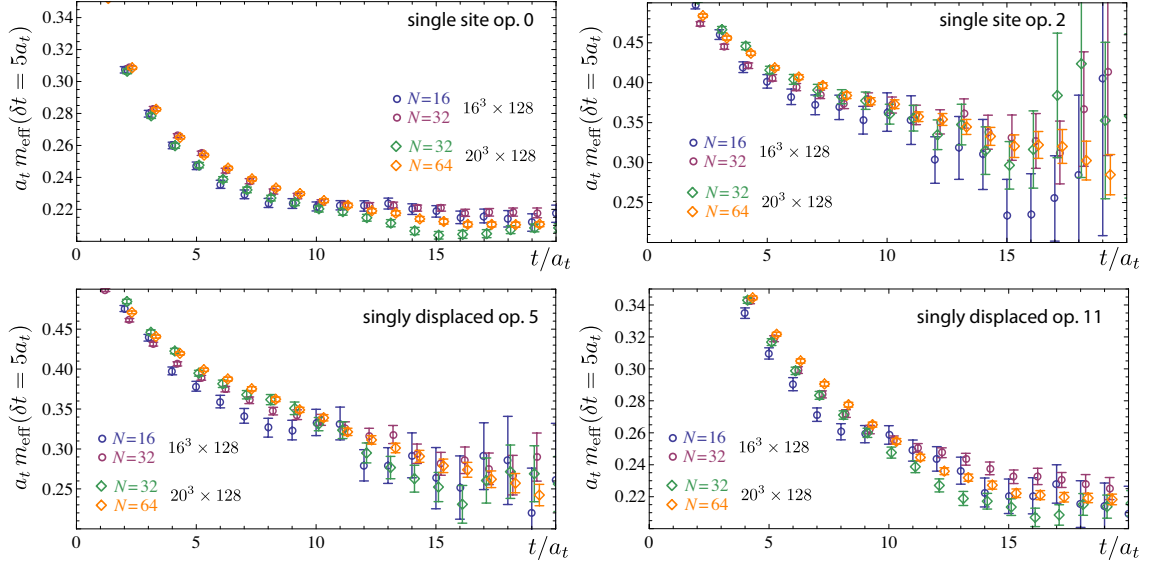


Figure 5.5: From [75], effective mass plots for two single-site and two singly displaced G_{1g} nucleon operators on $16^3 \times 128$ and $20^3 \times 128$ lattices calculated with different numbers of eigenvectors.

is the focus of the next chapter.

Chapter 6

The Excited Delta Spectrum

In this chapter, we describe a calculation of the excited delta spectrum. We used the distillation method described in the previous chapter to compute correlation functions of delta operators which transform as irreducible representations of the lattice symmetry group, as described in Chapter 3. We used lattices with $N_f = 2+1$, which included two flavors of dynamical light quark as well as dynamical strange quarks. This calculation represents one of the first excited spectrum calculations on anisotropic $N_f = 2 + 1$ lattices.

We used an improved gauge action and the clover fermion action, as described in Section 6.1. In Section 6.2 we describe the lattices used in the calculation and in Section 6.3 we describe the pruning of the delta operators. Finally, we give the results of the computation in Section 6.4.

6.1 Improved Actions

For the delta spectrum calculation, we used improved versions of the anisotropic Wilson gauge and fermion actions described in Chapter 4. The Wilson gauge action has corrections of order a^2 while the fermion action has corrections of order a . The improvement program seeks to push the corrections to a higher power of the lattice spacing.

With Symanzik improvement [77, 78], we add higher dimensional operators to the action with coefficients selected to eliminate the dominant discretization error. The Wilson gauge action can be improved to $\mathcal{O}(a^4)$ by adding dimension-six gauge invariant terms, written in terms of rectangular Wilson loops with perimeters of 6 gauge links. The coefficients in front of these new terms can be computed from perturbation theory [79]. The accuracy is improved at higher orders of perturbation theory, but the computations are prohibitively difficult above tree level. Tadpole improvement [80] is a technique to enhance the convergence of the perturbative series and improve the tree-level improved action. Tadpole improvement eliminates the contributions of tadpole diagrams to the gluon propagator by renormalizing the gauge action $U_\mu \rightarrow U_\mu/u_\mu$. u_μ is the tadpole factor which can be determined non-perturbatively. For the anisotropic action, we have different spatial and temporal tadpole factors. The anisotropic tree-level tadpole-improved action is given by [81]

$$S_G[U] = \frac{\beta}{N_c \xi_0} \left\{ \sum_{x,s>s'} \left[\frac{5}{3u_s^4} \mathcal{P}_{ss'}(x) - \frac{1}{12u_s^6} \mathcal{R}_{ss'}(x) \right] + \sum_{x,s} \left[\frac{4}{3u_s^2 u_t^2} \mathcal{P}_{st}(x) - \frac{1}{12u_s^4 u_t^2} \mathcal{R}_{st}(x) \right] \right\}, \quad (6.1)$$

where $\mathcal{P}_{ss'}(x)$ is the plaquette at point x in the $\mu\nu$ plane and $\mathcal{R}_{\mu\nu}(x)$ is the 2×1 rectangular Wilson loop. u_s and u_t are the spatial and temporal tadpole factors.

The clover action is an improvement over the Wilson fermion action which aims to eliminate $\mathcal{O}(a)$ corrections to the fermion action. The Wilson term in the fermion action is a dimension-five operator. There exists one other possible dimension-five operator: $\bar{\psi}(x) c_{SW} \sigma_{\mu\nu} F_{\mu\nu}(x) \psi(x)$, where

$$\sigma_{\mu\nu} = \frac{i}{2} [\gamma_\mu, \gamma_\nu]. \quad (6.2)$$

This is the Sheikholeslami-Wohlert or clover term [82]. On anisotropic lattices, we split the clover term into two: one part involving Wilson loops in the spatial planes, and the other involving temporal Wilson loops. The tadpole-improved tree-level spatial and temporal clover coefficients are given by [83]

$$c_s = \frac{\nu}{u_s^3}, \quad (6.3)$$

$$c_t = \frac{1}{2} \left(\nu + \frac{1}{\xi} \right) \frac{1}{u_t u_s^2}. \quad (6.4)$$

In the fermion action, we used stout-smeared gauge links which have different tadpole factors than the unsmeared gauge fields. We denote these factors \tilde{u}_s and \tilde{u}_t .

The quark matrix is then given by

$$\begin{aligned} K_{a\bar{\alpha};a\alpha}^A(x, y) = & \frac{1}{\tilde{u}_t} \left\{ \tilde{u}_t M^A + \hat{W}_t + \frac{1}{\gamma_f} \sum_s \hat{W}_s - \frac{1}{2} \left[\frac{1}{2} \left(\frac{\gamma_g}{\gamma_f} + \frac{1}{\xi} \right) \frac{1}{\tilde{u}_t \tilde{u}_s^2} \sum_s \sigma_{ts} F_{ts} \right. \right. \\ & \left. \left. + \frac{1}{\gamma_f} \frac{1}{\tilde{u}_s^3} \sum_{s < s'} \sigma_{ss'} F_{ss'} \right] \right\}, \end{aligned} \quad (6.5)$$

where $\gamma_g = \xi_0$ and $\gamma_f = \xi_0/\nu$ are the gauge and fermion anisotropies, and W_μ is the Wilson fermion operator.

When setting $\beta = 1.5$, it was found that the tadpole factors were given by $u_t = \tilde{u}_t = 1$, $u_s = 0.7336$, and $\tilde{u}_s = 0.9267$. The anisotropies were tuned to $\gamma_g = 4.3$ and $\gamma_f = 3.4$, which gave a renormalized anisotropy consistent with 3.5 [84].

6.2 Lattice Parameters

The strange quark mass was tuned as described in [85]. Two dimensionless coordinates l_Ω and s_Ω were defined:

$$l_\Omega = \frac{9m_\pi^2}{4m_\Omega^2}, \quad (6.6)$$

$$s_\Omega = \frac{9(2m_K^2 - m_\pi^2)}{4m_\Omega^2}. \quad (6.7)$$

To leading order in chiral perturbation theory, pseudoscalar masses are given by $m_P^2 = 2B(m_{q_1} - m_{q_2})$, where the m_{q_i} are the masses of the quarks within the meson, and B is a constant. Thus, s_Ω is independent of the light quark physics. Setting $m_s = -0.0743$ gave results for s_Ω consistent with the physical point, independent of the strange quark mass, as shown in Fig. 6.1.

We extracted the excited delta spectrum on $16^3 \times 128$ lattices with the mass of the light quarks set to $m_l = -0.0840$. This yielded a pion mass of $m_\pi = 0.0691(6)$. The scale was once again set using the Sommer scale, yielding an overall scale factor of $a_t^{-1} = 5640(20)$ MeV. In physical units, the pion mass is about 390 MeV. We used the distillation method with the baryon operators projected to the space spanned by the lowest 32 eigenvectors of the Laplacian operator. We generated perambulators to all possible time sinks, but for only five different time sources. We used 173 configurations and averaged over the five time sources.

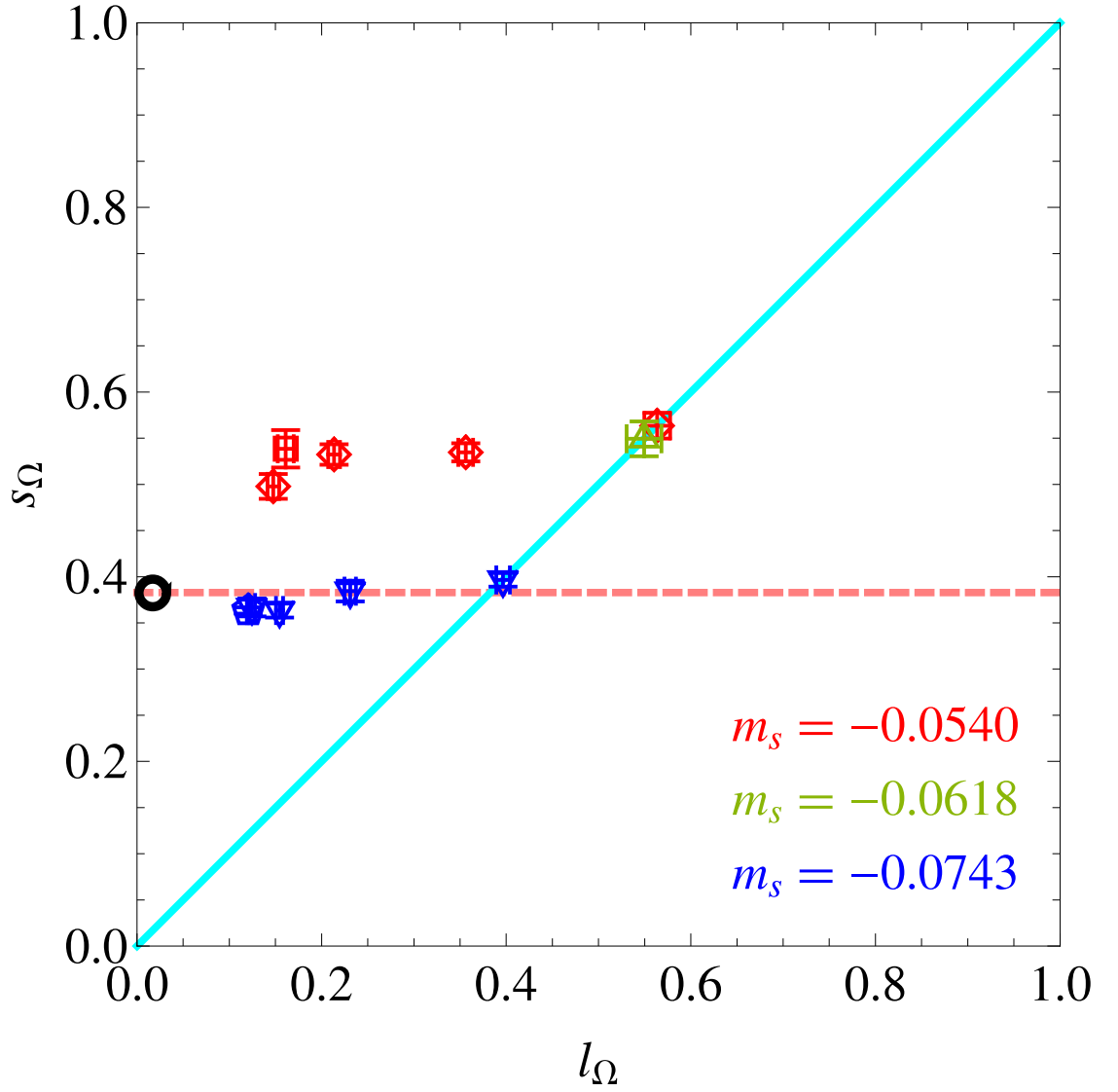


Figure 6.1: From [85], location of various $N_f = 2 + 1$ ensembles in the $l_\Omega - s_\Omega$ plane, defined in Eqs. (6.6) and (6.7). The black circle is the physical point (with the horizontal dashed line being the physical s_Ω), the red diamonds and squares have $m_s = -0.0540$, the green upper triangle has $m_s = -0.0618$, and the blue upside-down triangles and pentagons have $m_s = -0.0743$. The diagonal solid line are coordinates with three degenerate flavors.

6.3 Operator Pruning

To prune the delta operators, we followed a similar procedure as in the nucleon spectrum calculation. We found that there were groups of operators which had nearly identical correlators up to an overall normalization factor. As the effective energy is independent of normalization, the effective energy plots of these correlators looked nearly identical. We show an example in Fig. 6.2, where we have plotted the effective energy for six such operators. We concluded that these operators coupled to nearly identical states in the Hilbert space and thus, it was only necessary to include one such operator in the next stage of the pruning procedure. We compared the effective energies of operators in pairs. For each pair, we calculated the absolute value of the difference in effective energy divided by the jackknife error. If the average of this quantity over the first 16 timeslices was less than 2, then one of the operators was thrown out.

After completing this step, we continued the pruning by selecting, in each channel, up to 10 of the quietest operators for each displacement pattern. We generated the full 10×10 renormalized correlator matrix, given by Eq. (4.50) for each displacement pattern and searched for the best 4×4 submatrix based on the condition number. In this study, we did not require the sets of operators in opposite parity irreps to be identical. We decided that choosing an optimal set of positive and negative parity operators would lead to an improvement in the results which would outweigh the better statistics we could obtain by folding positive and negative parity correlators. We generated the full correlator matrix for all of the remaining

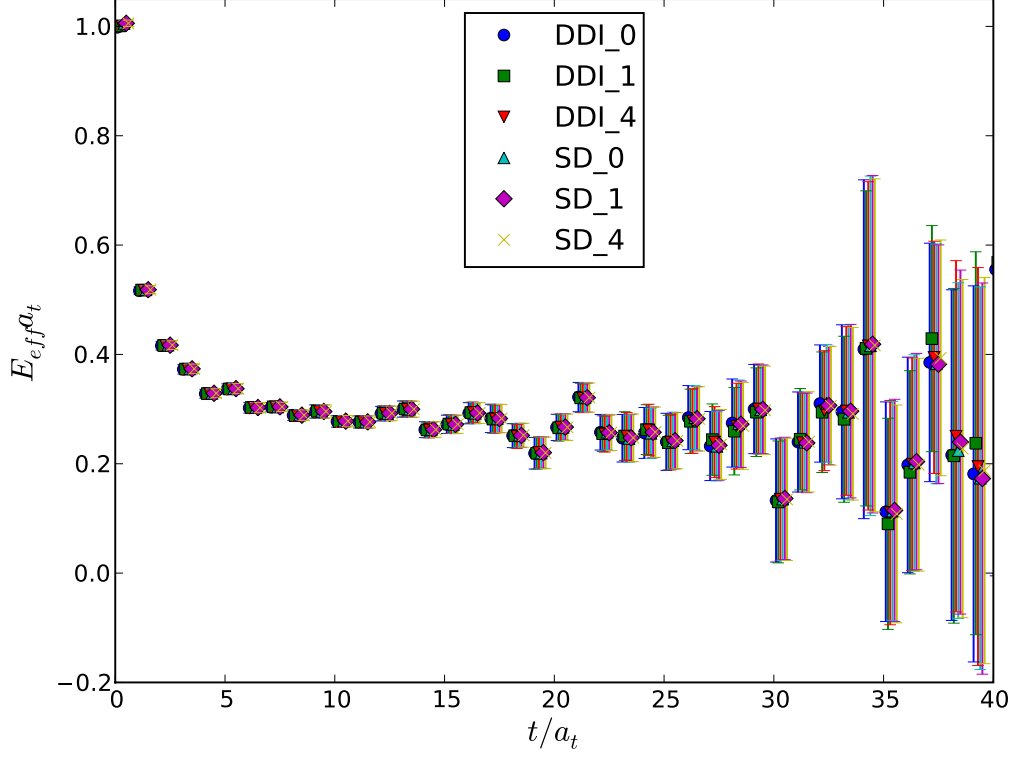


Figure 6.2: The effective energy for three single-site and three doubly-displaced-I delta operators. The nearly identical effective energy for all the operators suggests that they all couple to the same state in the Hilbert space.

operators in each channel and then once again pruned on condition number to select the final set of operators. In each channel we were able to obtain 9-11 well conditioned operators. The final sets of pruned operators are given in Appendix B.

6.4 Results

To extract the delta spectrum from the correlator matrix, we followed a similar procedure as in the nucleon spectrum study. We once again found that by rephasing

the operators, the matrix could be made completely real. These phases were found to be, within error bars, equal to 0, $\pi/2$, π , or $3\pi/2$ and were chosen to be one of those values. We then averaged the resulting real, symmetric matrix with its transpose.

We used the fixed eigenvector method to diagonalize the correlator matrix, choosing the optimal values of t_0 and t^* using the procedure described in Section 4.8.2. The diagonal elements were then fit with a double exponential form:

$$\tilde{C}_{II}^{fit} = Ae^{-E_I(t-t_0)} + (1-A)e^{-E'(t-t_0)}. \quad (6.8)$$

We found that the temporal extent of the lattice was sufficiently large that we could fit correlation functions on early time slices without any interference from backward-in-time propagating states.

We extracted the lowest four delta energy levels in each channel, except for the G_{1u} channel in which we obtained three levels. The results are shown in Table 6.1. In Figs. 6.3-6.8 we plot $C_{II}^{\Lambda}(t)e^{E_I^{\Lambda}(t-t_0)}$ for the extracted states, which provides a visual confirmation of the sensibility of the fits. Fig. 6.9 is a box plot of the extracted spectrum.

6.4.1 Discussion

For some of the low-lying states we can identify the corresponding continuum state. For the H_g channel, the lowest energy multi-hadron state is a $\pi - N$ p-wave state in which the pion and nucleon both must have non-zero momentum. The energy of the $\pi - N$ state in which both particles have the smallest non-zero

Table 6.1: The delta spectrum at $m_\pi = 390$ MeV with jackknife errors. We do not include the error in the determination of the scale that acts as an overall multiplicative factor in the range 0.965 to 1.035.

$G_{1g}, t_0 = 7, t^* = 9$			$G_{1u}, t_0 = 7, t^* = 11$		
time	Ea_t	E (MeV)	time	Ea_t	E (MeV)
3 – 21	0.3952(46)	2229(26)	5 – 21	0.3291(48)	1856(27)
3 – 17	0.4115(46)	2321(26)	3 – 16	0.4446(148)	2508(83)
2 – 16	0.452(60)	2549(34)	2 – 13	0.4959(66)	2797(37)
2 – 13	0.5223(92)	2946(52)			
$H_g, t_0 = 8, t^* = 11$			$H_u, t_0 = 8, t^* = 10$		
time	Ea_t	E (MeV)	time	Ea_t	E (MeV)
6 – 31	0.2583(34)	1457(19)	5 – 17	0.3377(43)	1905(24)
7 – 15	0.3173(69)	1790(39)	5 – 19	0.3434(54)	1937(30)
5 – 23	0.3847(152)	2170(86)	4 – 15	0.4506(240)	2541(135)
5 – 24	0.3885(104)	2191(59)	2 – 15	0.5029(91)	2836(51)
$G_{2g}, t_0 = 7, t^* = 9$			$G_{2u}, t_0 = 7, t^* = 9$		
time	Ea_t	E (MeV)	time	Ea_t	E (MeV)
3 – 21	0.4161(60)	2347(34)	2 – 13	0.5063(142)	2856(80)
3 – 14	0.4248(62)	2396(35)	2 – 14	0.5044(72)	2845(41)
3 – 12	0.4399(72)	2481(41)	2 – 13	0.5272(101)	2973(57)
2 – 11	0.5584(179)	3149(101)	2 – 12	0.5636(167)	3179(94)

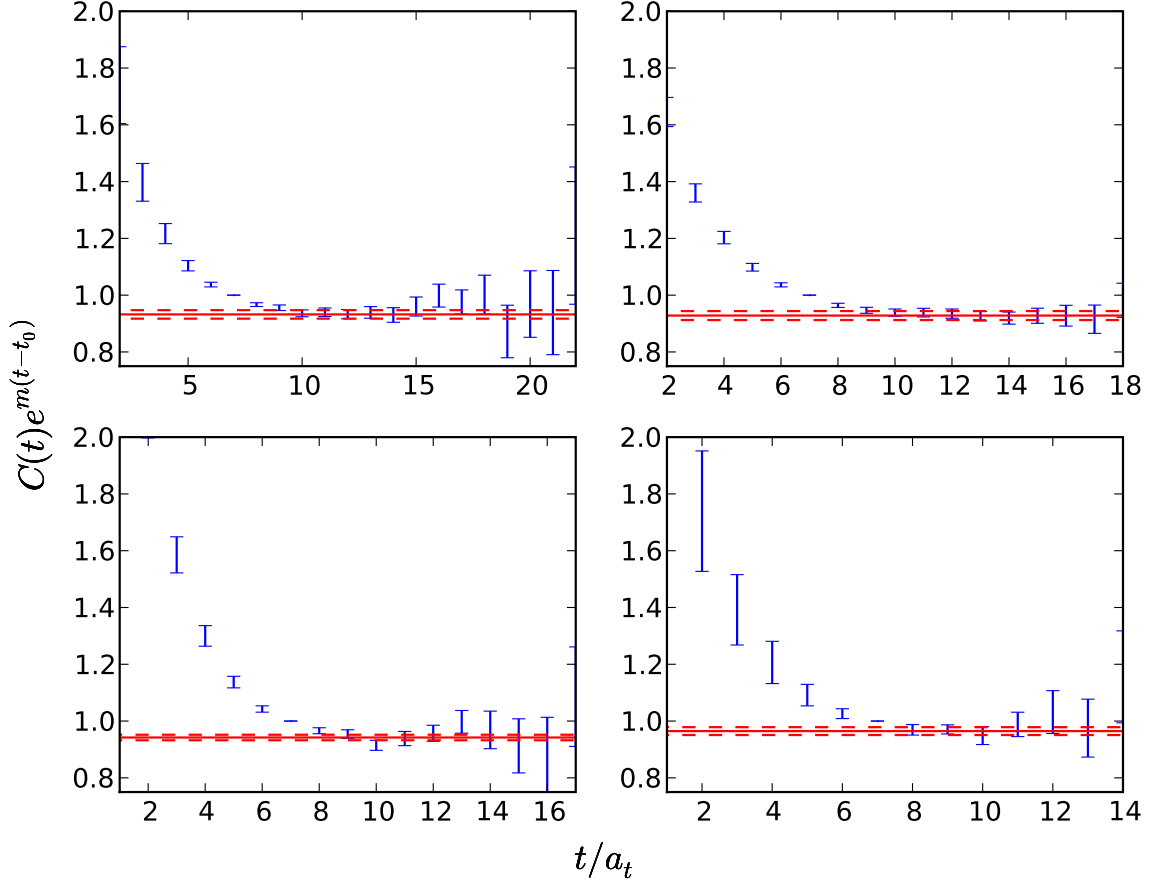


Figure 6.3: Plots of $C_{II}^\Lambda(t)e^{E_I^\Lambda(t-t_0)}$ for the ground (top left), first excited (top right), second excited (bottom left) and third excited (bottom right) delta states in the G_{1g} channel at $m_\pi = 390$ MeV. The plot plateaus to the value of A in Eq. (6.8), as determined by the fit, indicated by solid horizontal line. Horizontal dotted lines are jackknife errors on A .

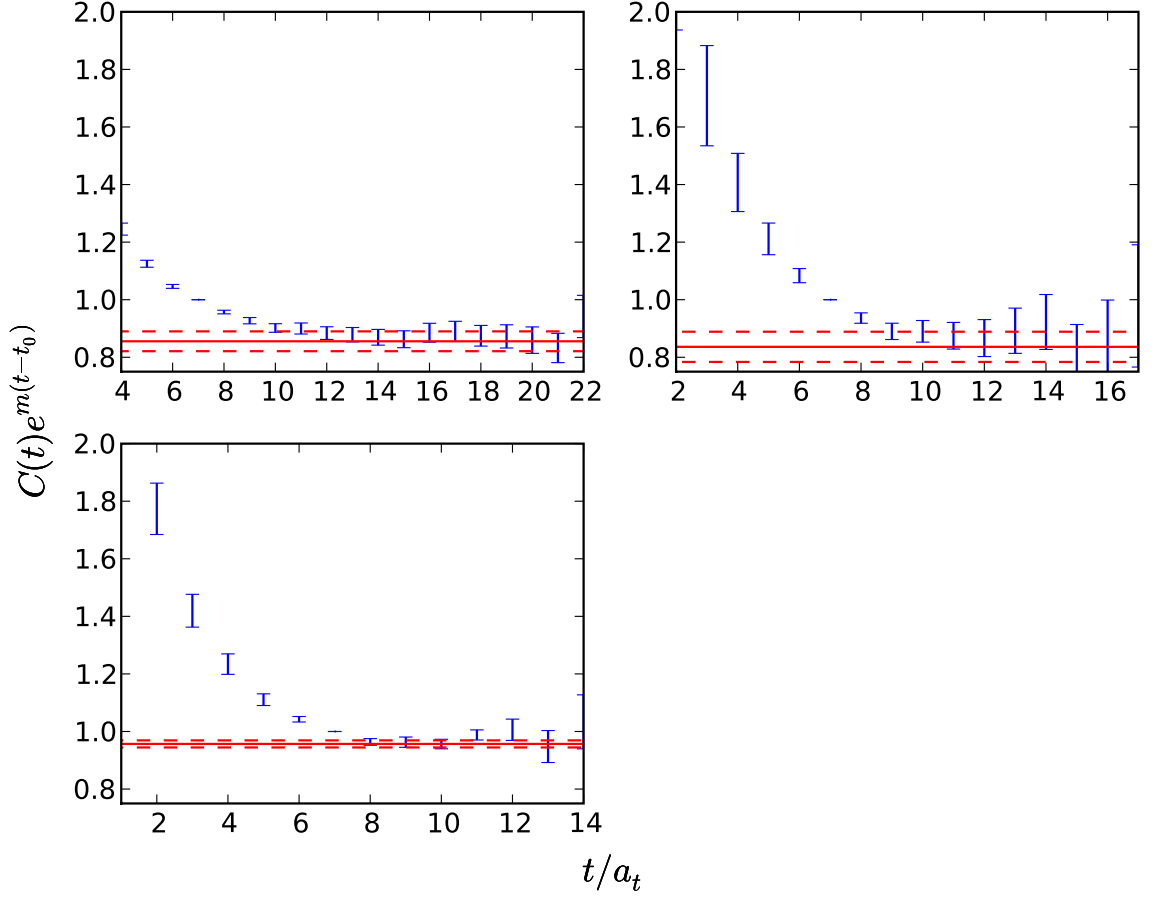


Figure 6.4: Plots of $C_{II}^\Lambda(t)e^{E_I^\Lambda(t-t_0)}$ for the ground (top left), first excited (top right), second excited (bottom left) delta states in the G_{1u} channel at $m_\pi = 390$ MeV. The plot plateaus to the value of A in Eq. (6.8), as determined by the fit, indicated by solid horizontal line. Horizontal dotted lines are jackknife errors on A .

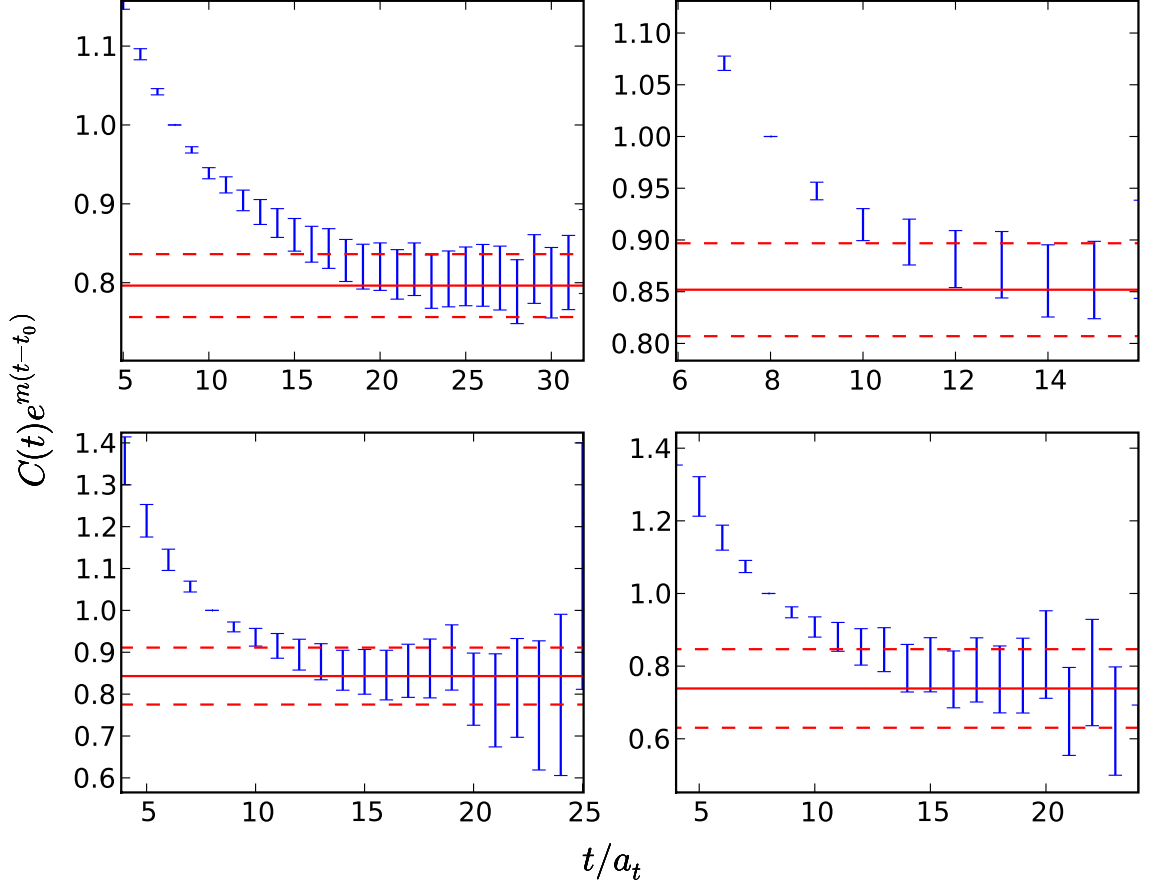


Figure 6.5: Plots of $C_{II}^\Lambda(t)e^{E_I^\Lambda(t-t_0)}$ for the ground (top left), first excited (top right), second excited (bottom left) and third excited (bottom right) delta states in the H_g channel at $m_\pi = 390$ MeV. The plot plateaus to the value of A in Eq. (6.8), as determined by the fit, indicated by solid horizontal line. Horizontal dotted lines are jackknife errors on A .

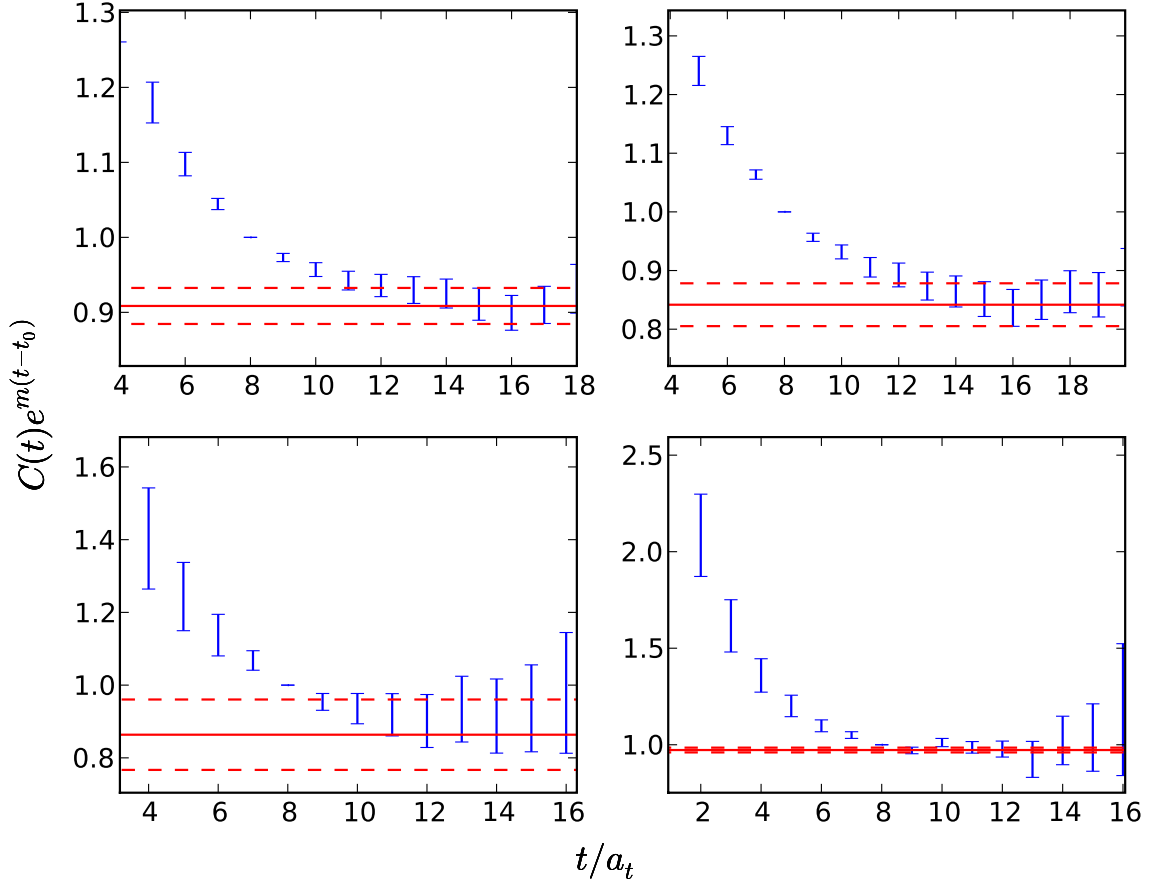


Figure 6.6: Plots of $C_{II}^\Lambda(t)e^{E_I^\Lambda(t-t_0)}$ for the ground (top left), first excited (top right), second excited (bottom left) and third excited (bottom right) delta states in the H_u channel at $m_\pi = 390$ MeV. The plot plateaus to the value of A in Eq. (6.8), as determined by the fit, indicated by solid horizontal line. Horizontal dotted lines are jackknife errors on A .

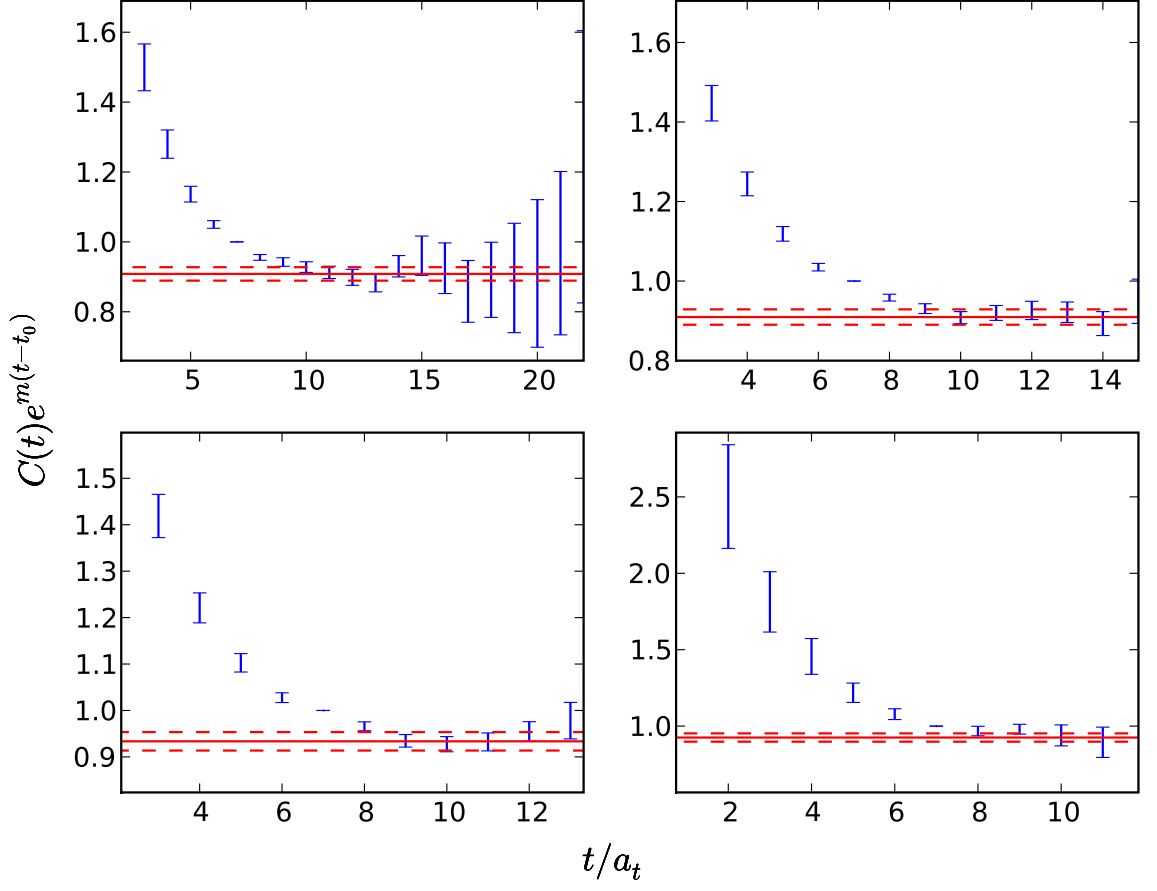


Figure 6.7: Plots of $C_{II}^\Lambda(t)e^{E_I^\Lambda(t-t_0)}$ for the ground (top left), first excited (top right), second excited (bottom left) and third excited (bottom right) delta states in the G_{2g} channel at $m_\pi = 390$ MeV. The plot plateaus to the value of A in Eq. (6.8), as determined by the fit, indicated by solid horizontal line. Horizontal dotted lines are jackknife errors on A .

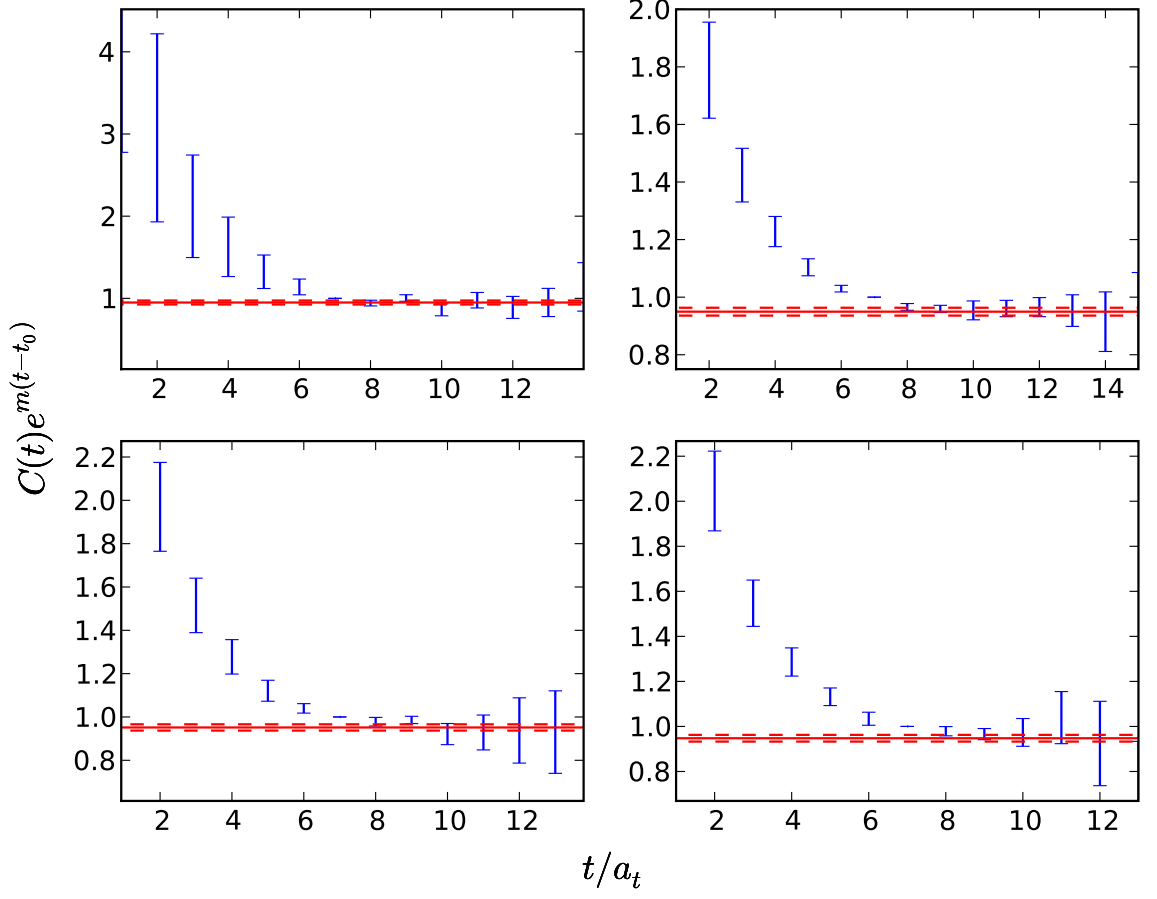


Figure 6.8: Plots of $C_{II}^\Lambda(t)e^{E_I^\Lambda(t-t_0)}$ for the ground (top left), first excited (top right), second excited (bottom left) and third excited (bottom right) delta states in the G_{2u} channel at $m_\pi = 390$ MeV. The plot plateaus to the value of A in Eq. (6.8), as determined by the fit, indicated by solid horizontal line. Horizontal dotted lines are jackknife errors on A .

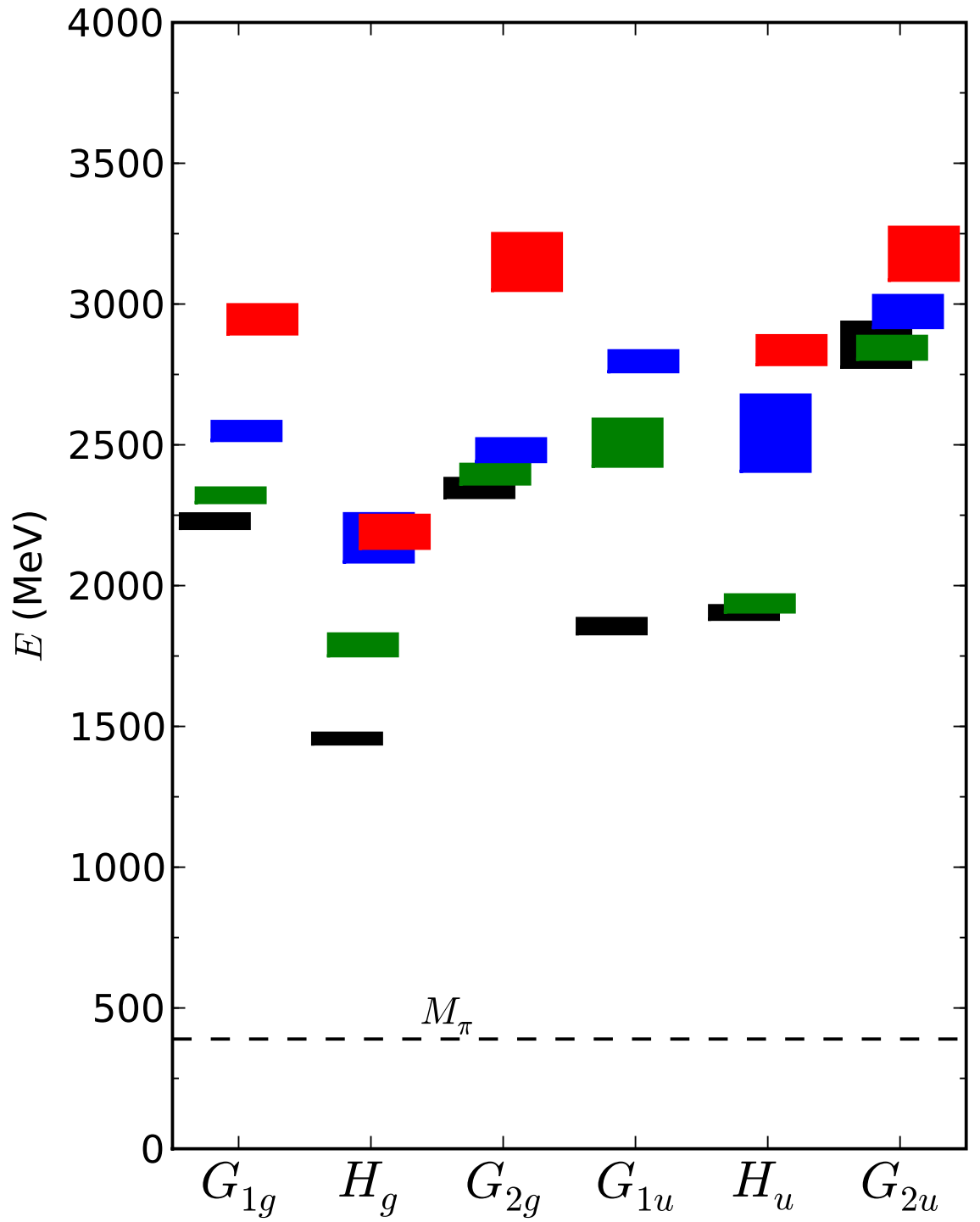


Figure 6.9: The delta spectrum at $m_\pi = 390$ MeV. We plot the lowest four energy levels in each channel (only three in the G_{1u}). The location of each box indicates the energy, while the height is the jackknife error.

momentum is $0.377(4)$. The lowest two states in the H_g channel fall well below this energy, and thus we identify these two states as the lowest two $\text{spin-}\frac{3}{2}^+$ states in the delta spectrum, the $\Delta(1232)$ and $\Delta(1600)$. In both the lattice spectrum and the physical spectrum, these are the two lowest energy delta states. In the physical spectrum the next two energy states are the negative parity $\text{spin-}\frac{1}{2}^-$ $\Delta(1620)$ and $\text{spin-}\frac{3}{2}^-$ $\Delta(1700)$ states. In the lattice spectrum we see a similar pattern, with the next lowest energy states occurring in the G_{1u} and H_u channels. We can identify the G_{1u} ground state with the $\Delta(1620)$.

In the H_u channel, the ground state has an energy which is nearly degenerate with the first excited state. This does not match the physical spectrum in which the $\text{spin-}\frac{5}{2}^-$ $\Delta(1930)$ would be the lowest excited state we would expect to see in the H_u channel. We would expect to see a larger energy gap between the lowest two H_u states, something which was observed in the quenched spectrum. The lowest energy multi-particle state in the H_u channel is a $\Delta - \pi$ s-wave state with an energy of $0.3274(35)$. Thus, one of the two lowest energies in the H_u channel may be a $\Delta - \pi$ state, while the other may be the $\Delta(1700)$. More data are needed to better understand these states. We do not attempt to identify any other lattice states with continuum states.

Chapter 7

Conclusions and Outlook

In this work we have calculated excited state spectra in quantum chromodynamics. Although we have not performed these computations at the physical pion mass, we have made several important steps towards the goal of computing quantities from lattice QCD which can be directly compared to experimental results.

Most importantly, we have shown that the variational method can be successfully employed to extract the energies of multiple excited states. We were able to extract around four states in every lattice irreducible representation for both the nucleon and delta systems at pion masses as low as about 400 MeV. Despite the unphysically large pion mass, many features of the low lying energy spectrum could be observed qualitatively. We were able to identify several low-lying lattice states with their counterparts in the continuum. We believe as we approach the physical pion mass, the energies of these states will converge to the experimentally observed values. Among these states was one of the first observations of spin- $\frac{5}{2}$ state on the lattice. On the other hand, the Roper resonance remains an open question as most lattice studies have failed to obtain the correct ordering of the spin- $\frac{1}{2}^-$ ground state and the first excited spin- $\frac{1}{2}^+$ state.

I have specifically worked on the extraction of these mass spectra for both the nucleon and the delta. For the nucleon system, I calculated the energy spectrum

from correlation functions generated by Adam Lichtl. The pruning and optimization of the operators was completed as part of his dissertation work on quenched lattices. I worked on the details of the variational analysis including the rephasing and folding of the correlators, the selection of the optimal t_0 and t^* parameters using the correlator reconstruction method, the diagonalization of the correlator matrices, and the extraction of the energies through fits of the diagonal matrix elements of the rotated correlator matrices. For the delta analysis, starting with perambulators and baryon elemental operators, I generated the correlation functions using the distillation method and extracted the spectrum using a similar procedure as in the nucleon analysis.

Currently, work is in progress to improve the quality of spectrum calculations. The Hadron Spectrum plans to use the distillation method to compute the nucleon and delta spectrum on several pion masses. The dependence of the energy levels on pion mass may enable a better understanding of how the calculated energies extrapolate to the physical point and help to identify potential multi-hadron states. Methods are also being tested which will facilitate spectrum calculations on larger lattice volumes, which may also aid in the identification of multi-hadron states. Ultimately, we would like to include multi-particle operators in the variational basis.

As we decrease the pion mass, there are several complications that we expect to arise. We expect the energies of multi-particle states to rapidly decrease and the density of these states within the spectrum to increase. Even at a pion mass around 400 MeV, many of the energies in the spectra were above the multi-particle thresholds. The identification of these states will become even more critical as the

pion mass is decreased. Also, at unphysically large pion masses, decay paths for many excited states are kinematically impossible and resonances in the physical spectrum become stable particles. Near the physical point, many excited lattice states will become unstable and couple to multi-particle scattering states. These resonances can be observed by examining the volume dependence of multi-particle scattering states. By varying the volume, the energy dependence of scattering states can be inferred and masses and widths of resonances can be determined by searching for avoided level crossings [86, 87, 88].

Computing technology is rapidly approaching the point where lattice QCD calculations at the physical point are possible. Recent calculations have been completed with a pion mass of 156 MeV, only about 20 MeV above the physical point [89]. Ultimately, the HadSpec collaboration will perform calculations at the physical pion mass with multi-hadron operators. The results presented in this thesis are an important step towards that goal.

Appendix A

Nucleon Operators

In this appendix we present the final sets of 16 optimized nucleon operators used in the variational analysis. The positive and negative parity irreps both used the same sets of corresponding operators, related by Eqs. (4.28) and (4.29). The projection coefficients for these operators are stored on the Jefferson Laboratory cluster in the directory `/cache/LHPC/MISC/baryons/projection_coefficients/`. The G_1 operators are given in Table A.1, the H operators in Table A.2, and the G_2 operators in Table A.3. By convention, indexing of the embedding begins at 0.

Table A.1: Final set of operators used in nucleon spectrum calculation in the G_1 channels.

Operator Number	Displacement Type	Embedding
1	Single-Site	2
2	Singly-Displaced	11
3	Singly-Displaced	17
4	Singly-Displaced	20
5	Doubly-Displaced-I	0
6	Doubly-Displaced-I	4
7	Doubly-Displaced-I	5
8	Doubly-Displaced-I	9
9	Doubly-Displaced-I	12
10	Doubly-Displaced-L	4
11	Doubly-Displaced-L	10
12	Triply-Displaced-T	3
13	Triply-Displaced-T	5
14	Triply-Displaced-T	9
15	Triply-Displaced-T	11
16	Triply-Displaced-T	25

Table A.2: Final set of operators used in nucleon spectrum calculation in the H channels.

Operator Number	Displacement Type	Embedding
1	Singly-Displaced	9
2	Singly-Displaced	10
3	Singly-Displaced	31
4	Doubly-Displaced-I	8
5	Doubly-Displaced-I	17
6	Doubly-Displaced-I	31
7	Doubly-Displaced-L	47
8	Doubly-Displaced-L	54
9	Doubly-Displaced-L	84
10	Doubly-Displaced-L	113
11	Doubly-Displaced-L	124
12	Triply-Displaced-T	35
13	Triply-Displaced-T	71
14	Triply-Displaced-T	86
15	Triply-Displaced-T	95
16	Triply-Displaced-T	104

Table A.3: Final set of operators used in nucleon spectrum calculation in the G_2 channels.

Operator Number	Displacement Type	Embedding
1	Singly-Displaced	0
2	Singly-Displaced	1
3	Singly-Displaced	2
4	Singly-Displaced	6
5	Doubly-Displaced-I	5
6	Doubly-Displaced-I	6
7	Doubly-Displaced-I	7
8	Doubly-Displaced-L	32
9	Doubly-Displaced-L	37
10	Doubly-Displaced-L	41
11	Doubly-Displaced-L	52
12	Triply-Displaced-T	1
13	Triply-Displaced-T	33
14	Triply-Displaced-T	45
15	Triply-Displaced-T	51
16	Triply-Displaced-T	61

Appendix B

Delta Operators

In this appendix we present the final sets of optimized delta operators used in the variational analysis. The projection coefficients for these operators are stored on the Jefferson Laboratory cluster in the directory `/home/jbulava/baryons/projection_coefficients/`. The G_{1g} operators are given in Table B.1, the G_{1u} operators are given in Table B.2, the H_g operators in Table B.3, the H_u operators in Table B.4, the G_{2g} operators in Table B.5, and the G_{2u} operators in Table B.6. By convention, indexing of the embedding begins at 0.

Table B.1: Final set of operators used in the delta spectrum calculation in the G_{1g} channel.

Operator Number	Displacement Type	Embedding
1	Singly-Displaced	4
2	Singly-Displaced	8
3	Singly-Displaced	9
4	Doubly-Displaced-I	0
5	Doubly-Displaced-I	1
6	Doubly-Displaced-I	7
7	Doubly-Displaced-L	8
8	Doubly-Displaced-L	28
9	Doubly-Displaced-L	31
10	Triply-Displaced-T	1
11	Triply-Displaced-T	12

Table B.2: Final set of operators used in the delta spectrum calculation in the G_{1u} channel.

Operator Number	Displacement Type	Embedding
1	Singly-Displaced	4
2	Singly-Displaced	8
3	Singly-Displaced	13
4	Doubly-Displaced-I	6
5	Doubly-Displaced-I	7
6	Doubly-Displaced-L	10
7	Doubly-Displaced-L	28
8	Doubly-Displaced-L	31
9	Triply-Displaced-T	26

Table B.3: Final set of operators used in the delta spectrum calculation in the H_g channel.

Operator Number	Displacement Type	Embedding
1	Single-Site	0
2	Singly-Displaced	11
3	Singly-Displaced	17
4	Doubly-Displaced-I	3
5	Doubly-Displaced-L	19
6	Doubly-Displaced-L	44
7	Triply-Displaced-T	24
8	Triply-Displaced-T	25
9	Triply-Displaced-T	34

Table B.4: Final set of operators used in the delta spectrum calculation in the H_u channel.

Operator Number	Displacement Type	Embedding
1	Single-Site	0
2	Single-Site	1
3	Doubly-Displaced-I	9
4	Doubly-Displaced-I	13
5	Doubly-Displaced-L	30
6	Doubly-Displaced-L	62
7	Triply-Displaced-T	29
8	Triply-Displaced-T	30
9	Triply-Displaced-T	48
10	Triply-Displaced-T	52

Table B.5: Final set of operators used in the delta spectrum calculation in the G_{2g} channel.

Operator Number	Displacement Type	Embedding
1	Singly-Displaced	0
2	Singly-Displaced	2
3	Singly-Displaced	3
4	Singly-Displaced	4
5	Doubly-Displaced-L	7
6	Doubly-Displaced-L	8
7	Doubly-Displaced-L	21
8	Doubly-Displaced-L	28
9	Triply-Displaced-T	10
10	Triply-Displaced-T	13
11	Triply-Displaced-T	18

Table B.6: Final set of operators used in the delta spectrum calculation in the G_{2u} channel.

Operator Number	Displacement Type	Embedding
1	Singly-Displaced	2
2	Singly-Displaced	3
3	Doubly-Displaced-L	8
4	Doubly-Displaced-L	11
5	Doubly-Displaced-L	19
6	Doubly-Displaced-L	29
7	Triply-Displaced-T	3
8	Triply-Displaced-T	13
9	Triply-Displaced-T	30

Bibliography

- [1] F. Halzen and A. Martin. *Quarks and Leptons: An Introductory Course in Modern Particle Physics*. (John Wiley and Sons, Inc., 1984).
- [2] D. Perkins. *Introduction to High Energy Physics* (Cambridge University Press, 2000).
- [3] D. Griffiths. *Introduction to Elementary Particles* (John Wiley and Sons, Inc., 1987).
- [4] C. Amsler et al. (Particle Data Group). Phys. Lett. **B667**, 1 (2008).
- [5] S. L. Glashow. Nucl. Phys. **22**, 579 (1961).
- [6] S. Weinberg. Phys. Rev. Lett. **19**, 1264 (1967).
- [7] A. Salam (1968). Originally printed in Svartholm: Elementary Particle Theory, Proceedings Of The Nobel Symposium Held 1968 At Lerum, Sweden, Stockholm 1968, 367-377.
- [8] A. W. Thomas and W. Weise. *The Structure of the Nucleon* (Wiley-VCH, 2001).
- [9] D. H. Perkins. Nature **159**, 126 (1947).
- [10] A. Pais. Phys. Rev. **86**, 663 (1952).
- [11] M. Gell-Mann. Phys. Rev. **92**, 833 (1953).
- [12] T. Nakano and K. Nishijima. Prog. Theor. Phys. **10**, 581 (1953).
- [13] W. Heisenberg. Z. Phys. **77**, 1 (1932).
- [14] F. E. Close. *An Introduction to Quarks and Partons* (Academic Press, 1979).
- [15] M. Gell-Mann. Phys. Rev. **125**, 1067 (1962).
- [16] Y. Ne'eman. Nucl. Phys. **26**, 222 (1961).
- [17] M. Gell-Mann. Phys. Lett. **8**, 214 (1964).
- [18] G. Zweig CERN-TH-401.
- [19] G. Zweig CERN-TH-412.
- [20] O. W. Greenberg. Phys. Rev. Lett. **13**, 598 (1964).
- [21] M. Y. Han and Y. Nambu. Phys. Rev. **139**, B1006 (1965).

- [22] W. K. H. Panofsky Presented at 14th Int. Conf. on High Energy Physics, Vienna, Aug 1968.
- [23] R. P. Feynman. Phys. Rev. Lett. **23**, 1415 (1969).
- [24] H. Fritzsch and M. Gell-Mann. eConf **C720906V2**, 135 (1972).
hep-ph/0208010.
- [25] H. Fritzsch, M. Gell-Mann and H. Leutwyler. Phys. Lett. **B47**, 365 (1973).
- [26] D. J. Gross and F. Wilczek. Phys. Rev. Lett. **30**, 1343 (1973).
- [27] H. D. Politzer. Phys. Rev. Lett. **30**, 1346 (1973).
- [28] M. E. Peskin and D. V. Schroeder. *An Introduction to Quantum Field Theory* (Westview Press, 1995).
- [29] S. Basak et al. Phys. Rev. **D76**, 074504 (2007). 0709.0008.
- [30] A. C. Lichtl (2006). hep-lat/0609019.
- [31] C. Morningstar (2008). 0810.4448.
- [32] H. J. Rothe. *Lattice Gauge Theories: An Introduction* (World Scientific Publishing, 2005).
- [33] I. Montvay and G. Munster. *Quantum Fields on a Lattice* (Cambridge University Press, 1994).
- [34] T. DeGrand and C. DeTar. *Lattice Methods For Quantum Chromodynamics* (World Scientific Publishing, 2006).
- [35] M. Creutz Cambridge, Uk: Univ. Pr. (1983) 169 P. (Cambridge Monographs On Mathematical Physics).
- [36] R. P. Feynman. Rev. Mod. Phys. **20**, 367 (1948).
- [37] R. P. Feynman and A. R. Hibbs. *Quantum Mechanics and Path Integrals* (McGraw-Hill, 1965).
- [38] K. G. Wilson. Phys. Rev. **D10**, 2445 (1974).
- [39] H. B. Nielsen and M. Ninomiya. Nucl. Phys. **B185**, 20 (1981).
- [40] K. G. Wilson. In A. Zichichi, ed., *Phenomena in Subnuclear Physics* (Plenum Press, 1975).
- [41] M. Luscher and U. Wolff. Nucl. Phys. **B339**, 222 (1990).
- [42] B. Blossier, M. Della Morte, G. von Hippel, T. Mendes and R. Sommer (2009). 0902.1265.

- [43] B. Efron. *The Jackknife, the Bootstrap, and Other Resampling Plans* (Society for Industrial and Applied Mathematics, 1982).
- [44] S. Basak et al. (Lattice Hadron Physics (LHPC)). Phys. Rev. **D72**, 074501 (2005). [hep-lat/0508018](#).
- [45] S. Basak et al. Phys. Rev. **D72**, 094506 (2005). [hep-lat/0506029](#).
- [46] S. Gusken et al. Phys. Lett. **B227**, 266 (1989).
- [47] M. G. Alford, T. Klassen and P. Lepage. Nucl. Phys. Proc. Suppl. **47**, 370 (1996). [hep-lat/9509087](#).
- [48] C. Morningstar and M. J. Peardon. Phys. Rev. **D69**, 054501 (2004). [hep-lat/0311018](#).
- [49] S. Basak et al. PoS **LAT2005**, 076 (2006). [hep-lat/0509179](#).
- [50] M. Hamermesh. *Group Theory and Its Application to Physical Problems* (Dover Publications, Inc., 1962).
- [51] C. Morningstar. Unpublished notes circulated among Hadron Spectrum Collaboration (2006).
- [52] S. K. Kim. *Group Theoretical Methods and Applications to Molecules and Crystals* (Cambridge University Press, 1999).
- [53] S. Altmann and P. Herzog. *Point-Group Theory Tables* (Oxford University Press, 1994).
- [54] J. M. Bulava et al. Phys. Rev. **D79**, 034505 (2009). [0901.0027](#).
- [55] W. H. Press, S. A. Teukolsky, W. T. Vetterling and B. P. Flannery. *Numerical Recipes in C* (Cambridge University Press, 1992).
- [56] R. G. Edwards and B. Joo (SciDAC). Nucl. Phys. Proc. Suppl. **140**, 832 (2005). [hep-lat/0409003](#).
- [57] G. P. Lepage Invited lectures given at TASI'89 Summer School, Boulder, CO, Jun 4-30, 1989.
- [58] T. R. Klassen. Nucl. Phys. **B533**, 557 (1998). [hep-lat/9803010](#).
- [59] T. R. Klassen. Nucl. Phys. Proc. Suppl. **73**, 918 (1999). [hep-lat/9809174](#).
- [60] T. Umeda et al. (CP-PACS). Phys. Rev. **D68**, 034503 (2003). [hep-lat/0302024](#).
- [61] R. Sommer. Nucl. Phys. **B411**, 839 (1994). [hep-lat/9310022](#).
- [62] C. Aubin et al. Phys. Rev. **D70**, 094505 (2004). [hep-lat/0402030](#).

- [63] C. Bernard et al. (MILC). PoS **LAT2006**, 163 (2006). [hep-lat/0609053](#).
- [64] J. M. Bulava et al. (Hadron Spectrum) (2008). [0810.0253](#).
- [65] J. J. Dudek, R. G. Edwards, N. Mathur and D. G. Richards. Phys. Rev. **D77**, 034501 (2008). [0707.4162](#).
- [66] C. Michael. Phys. Rev. **D49**, 2616 (1994). [hep-lat/9310026](#).
- [67] F. James and M. Winkler (2004). <http://www.cern.ch/minuit/>.
- [68] D. C. Moore and G. T. Fleming. Phys. Rev. **D74**, 054504 (2006). [hep-lat/0607004](#).
- [69] K. Bitar, A. D. Kennedy, R. Horsley, S. Meyer and P. Rossi. Nucl. Phys. **B313**, 348 (1989).
- [70] H. R. Fiebig and R. M. Woloshyn. Phys. Rev. **D42**, 3520 (1990).
- [71] S.-J. Dong and K.-F. Liu. Phys. Lett. **B328**, 130 (1994). [hep-lat/9308015](#).
- [72] J. Foley et al. Comput. Phys. Commun. **172**, 145 (2005). [hep-lat/0505023](#).
- [73] S. Bernardson, P. McCarty and C. Thron. Comput. Phys. Commun. **78**, 256 (1993).
- [74] W. Wilcox (1999). [hep-lat/9911013](#).
- [75] M. Peardon et al. (2009). [0905.2160](#).
- [76] F. M. Gomes and D. Sorensen (1998). <http://www.caam.rice.edu/software/ARPACK/>.
- [77] K. Symanzik. Nucl. Phys. **B226**, 187 (1983).
- [78] K. Symanzik. Nucl. Phys. **B226**, 205 (1983).
- [79] M. Luscher and P. Weisz. Phys. Lett. **B158**, 250 (1985).
- [80] G. P. Lepage and P. B. Mackenzie. Phys. Rev. **D48**, 2250 (1993). [hep-lat/9209022](#).
- [81] C. J. Morningstar and M. J. Peardon. Phys. Rev. **D60**, 034509 (1999). [hep-lat/9901004](#).
- [82] B. Sheikholeslami and R. Wohlert. Nucl. Phys. **B259**, 572 (1985).
- [83] P. Chen. Phys. Rev. **D64**, 034509 (2001). [hep-lat/0006019](#).
- [84] R. G. Edwards, B. Joo and H.-W. Lin. Phys. Rev. **D78**, 054501 (2008). [0803.3960](#).

- [85] H.-W. Lin et al. (Hadron Spectrum). Phys. Rev. **D79**, 034502 (2009).
0810.3588.
- [86] B. S. DeWitt. Phys. Rev. **103**, 1565 (1956).
- [87] U. J. Wiese. Nucl. Phys. Proc. Suppl. **9**, 609 (1989).
- [88] M. Luscher. Nucl. Phys. **B364**, 237 (1991).
- [89] S. Aoki, K.-I. Ishikawa, N. Ishizuka, T. Izubuchi, D. K. K. Kanaya,
Y. Kuramashi, Y. Namekawa, M. Okawa, Y. Taniguchi, A. Ukawa, N. Ukita
and T. Yoshie. Phys. Rev. D. page 034503 (2009).